Spectroscopic monitoring of broad protein conformational ensembles

Dissertation zur Erlangung des

akademischen Grades eines Doktors der

Naturwissenschaften (Dr.rer.nat.)

vorgelegt von

Patrick Roser

an der

Universität Konstanz

Mathematisch-Naturwissenschaftliche Sektion

Fachbereich Chemie

Konstanz, 2020

Tag der mündlichen Prüfung: 29.11.2019

1. Referent: Prof. Dr. Malte Drescher

2. Referentin: Prof. Dr. Karin Hauser

Es kommt nicht darauf an, mit dem Kopf durch die Wand
zu rennen, sondern mit den Augen die Tür zu finden.

– Werner von Siemens

Danksagung

Der vielleicht wichtigste Teil dieser Arbeit ist dieser hier, der alle Mitwirkenden und helfenden Personen im Rahmen meiner Promotion gewidmet ist. Auch wenn ich hier sicherlich nicht alle Personen aufzählen kann, danke ich doch jedem Beteiligten an dieser Stelle.

Zuerst sei hier Malte Drescher zu erwähnen, der mich in den letzten Jahren stets unterstützt hat und mir den nötigen wissenschaftlichen Freiraum gegeben hat, ohne den roten Faden abreißen zu lassen. Vielen Dank dafür und die schöne Zeit in deiner Arbeitsgruppe.

Karin Hauser danke ich für die Übernahme des Zweitgutachtens und damit vor allem dem Zeitaufwand, der damit verbunden ist. Valentin Wittmann danke ich für die Übernahme des Prüfungsvorsitzes.

Meinem Thesis Kommittee, Marcel Leist und Michael Kovermann, möchte ich danken für die Zeit und Enthusiasmus, die sie mir bei der Unterstützung meiner Projekte entgegen gebracht haben.

Allen Kollegen der Arbeitsgruppe Drescher, insbesondere auch den mittlerweile schon als Alumni geltenden Christian, Marta, Andi, Martin und Frank, danke ich für die tolle Stimmung in der AG – sowohl wissenschaftlich als auch im Privaten. Besonders danken möchte ich dabei Julia, die mir gerade am Anfang meiner Promotion mit viel Geduld die Thematik näher gebracht hat. Dabei danke ich auch Juliane, die einen Teil meiner Arbeit weiterführen wird und dabei sicherlich weiterhin mit viel Elan und Kreativität erfolgreich sein wird.

Besonders danken möchte ich den Personen, die ich betreuen durfte und die mich bei meiner Arbeit tatkräftig unterstützt haben: Katharina, Frederike, Eli und Leon. Vielen Dank für euren Einsatz und oft auch sehr hilfreichen Input, vor allem in biologischen Fragen.

Bei den Facilities NMR und Proteomics möchte ich mich für die freundliche Unterstützung bedanken, vor allem aber natürlich für die erfolgreichen Messungen meiner Proben. Dank gilt auch Daniel Hammler, der auf kleinem Dienstweg Messungen möglich gemacht hat und dafür seine persönliche Zeit geopfert hat.

Ohne meine Kooperationspartner innerhalb und außerhalb von Konstanz wäre diese Arbeit so sicherlich nicht möglich gewesen. Daher gilt besonderer Danke Christine Peter samt Christoph, Kubi und Sascha für die spannende Zusammenarbeit. Ebenso wichtig war die Zusammenarbeit mit Daniel Rauh und Jörn Weisner aus Dortmund, die in den Kinasen-Projekten mit viel Enthusiasmus und tollen Ideen mitgearbeitet haben.

Der Abschluss ist natürlich den wichtigsten Personen vorbehalten, die mich in meiner gesamten Zeit unterstützt haben – meinen Freunden und meiner Familie. Ganz besonders danke ich Markus und Dave, die immer ein offenes Ohr für mich hatten in privaten wie wissenschaftlichen Fragen. Meinen Eltern, Großeltern, meinem Bruder und Jenny danke ich für die uneingeschränkte Unterstützung und Vertrauen, ohne die ich sicherlich heute nicht diese Thesis schreiben würde. Vielen Dank euch für den Rückhalt trotz der langen Studienzeit. Der Abschluss gehört natürlich Cora, die mir ein wunderbarer Rückhalt ist und mich stets motiviert und unterstützt, vielen Dank dafür!

Table of contents

1. General introduction

The proper folding of proteins ensures the correct function of a myriad of vital cellular processes in biological systems, ultimately also in humans. Malfunctions in these lead to manifold disease patterns such as cancer or neurodegenerative diseases. In many cases, their origin boils down to protein misfolding. Understanding folding, refolding and misfolding processes in biomolecules is thus critical in the scope of disease treatment and a structure-based design of effectors and drugs. Historically, manifold techniques were developed to assess structure analysis of mostly well-folding biomolecules. However, the definition of structure does not only cover discrete and well-defined secondary and tertiary structure elements. The lack of an unambiguous, discrete structure and its biological implications is of central importance in biomolecules that exhibit partial or full disorder. Proteins lacking discrete structuring are termed intrinsically disordered proteins and are crucially linked to multiple clinical pictures. Not only their malfunctioning is of utmost interest, also their interactions in a cellular context is important. Analysis of structural ambiguity in these molecules is thus of great interest and imposes major challenges to state-of-the-art techniques such as X-ray crystallography. The limited availability of techniques to study these proteins heavily impedes the development of deeper structural knowledge, highlighting the need for new spectroscopic tools.

In the following, intrinsic disorder in two different biologically relevant systems was explored using both experimental and computational techniques. At first, the structural ensemble of alpha-synuclein based peptide fragments and the implications of disease-related point mutations were analyzed. Alpha-synuclein is involved in the pathogenic course of Parkinson's disease and does not exhibit distinct structuring in solution. Another case of molecular disorder is imposed by the protein kinase p38α, whose function involves *e.g.* signal processing. This protein is well-structured throughout most of its sequence with the exception of the so-called activation loop region. This sequence area is fundamental to the kinase activity, despite the lack of secondary structure elements.

In both of these cases, intrinsic disorder is studied by a combination of available spectroscopic tools to strive for deeper insights into mechanisms of folding, unfolding and ultimately misfolding. These findings will be key steps to understand underlying mechanisms and their causes that could potentially help in finding new pathways to prevent protein malfunctioning.

2. Disordered structures in biomolecules

The investigation of the connectivity between the structure of proteins and the consequential effect on their biological function has been a crucial research interest in the past decades.[1] This includes processes of folding, refolding and unfolding that are crucially impacting the molecular behavior of biomolecules.[2-4] The large spectroscopic toolbox available to get insight into molecular structuring has led to an enormous collection of datasets available *via* libraries like the protein data bank PDB.[5] Many protein structures have been resolved using powerful techniques like crystal structure analysis. However, these techniques rely on molecules adopting rigid and unambiguous structures as a prerequisite for the formation of crystals. In general, molecular flexibility and the presence of a multitude of structural substates lead to a loss in positioning precision for these methods. Molecules adopting multiple conformations are challenging to analyze and need other experimental approaches (as reviewed in chapter 3).

Typically, the absence of a unique or few structural states is termed structural disorder.[6] The classification of molecules into ordered and disordered is under debate, as disorder does not necessarily involve a complete lack of local structuring.[7] The most prominent case of disorder are intrinsically disordered proteins (IDPs) that typically lack structural features throughout most of their amino acid sequence and are involved in a variety of biological functions and malfunctions including neurodegenerative diseases.[8] IDPs such as alpha-synuclein or tau or are encoded by approximately 30% of the human genome, depicting the importance in a biological context.[9] Extensive studies on IDPs have been conducted and reviewed.[10-11]

In contrast to this, disorder can further be found locally in a restricted part of otherwise well-structured proteins as seen in the activation loop of protein kinases[12] or in protein fibrils[13]. This local disorder, despite lacking a clear structure, can still be critically involved in the biological activities by *e.g.* triggering a catalytic activity of substrate recognition. In terms of structural analysis, a locally disordered domain depicts a situation that reflects many of the challenges also present for fully disordered proteins, highlighting the broad applicability of the term disorder in a biological context. The assessment of the flexibility in domains is indispensable for understanding their biological relevance. The terms order and disorder should not be seen as binary, as even in flexible and ambiguous domains a certain degree of alignment or order can be found. Therefore, it is important to understand what disorder really implies for a protein of interest and techniques able to differentiate between order and disorder are necessary. A crucial difference between fully and partially disordered molecules is that for the latter, boundary constraints are introduced to the description of conformational equilibria. While IDPs can adopt large variety of different conformations, disordered

domains are restricted at both ends to the rigid backbone structures of the proteins they belong to. This renders access to more precise descriptions of these domains as anchoring points with well-known locations can be used to monitor structural changes.

In this study, two prominent proteins were studied that depict either a fully intrinsically disordered protein or a locally disordered domain in a stable three-dimensional structure. Alpha-synuclein (ASYN) depicts a prominent example for the former while p38α with its unstructured activation loop depicts a rather confined disordered region in a rigid structure. Both of these were studied extensively in this work and will be introduced briefly in the corresponding chapters 4 and 5.

3. Spectroscopic techniques to study structure and dynamics of proteins

The interplay between structure and activity of biomolecules, in this study proteins, and the associated demand for structural insights led to the development of a multitude of experimental techniques that assess this. Crystallographic techniques have proven to yield structure models with atomistic precision, provided that a protein crystal can be prepared. Ordered proteins with a well-characterized secondary and tertiary structure are often feasible to crystallization while molecules incorporating flexible or even unstructured regions are difficult to analyze using these methods. Structure elucidation of disordered proteins and regions is more complicated and alternative methods to describe plasticity and dynamics of these regions were needed. The most prominent techniques are nuclear magnetic resonance (NMR), circular dichroism (CD), (single-molecule) fluorescence energy transfer ((sm)FRET), infrared (IR) spectroscopy and electron paramagnetic resonance (EPR). In the following, a short overview of possibilities to elucidate structure and dynamics using EPR and CD will be given, for details on NMR, IR and FRET extensive reviews are available.[10, 14-18]

With the upcoming of new experimental techniques and improving measurement capabilities, EPR spectroscopy has developed into a powerful tool, allowing insights into intrinsically disordered proteins.[19] Especially in the case of broad structural equilibria and structural ambiguities, sparse distance restraints are often not enough to correctly describe the underlying ensemble. Therefore, joint measurements combining distance restraints from experimental datasets with molecular dynamics simulations have been developed and risen to a powerful tool, enabling insights into complex structural ensembles.[20-21]

3.1. Site-directed spin labeling renders access to selective structural studies

The concept of site-directed spin labeling (SDSL) is based on the introduction of a paramagnetic tag to a molecule or object of interest, allowing subsequent analysis using magnetic resonance spectroscopy. While in this work the objects studied are proteins and protein-based peptides, SDSL is used in a variety of molecules including nucleic acids,[22] lipids[23] and polymer samples.[24-25] Many proteins are diamagnetic and thus undetectable using magnetic resonance methods, exception are proteins bearing inherent paramagnetic centers such as flavoproteins or photosystems[26-27]. Therefore, a spin labeling step is typically needed in advance to EPR studies. This necessity is a significant advantage as site-specific introduction of labels allows for unambiguous and virtually background-free detection even in complex systems. Labeled proteins render

the assessment of many different physical aspects possible, these have been extensively studied and reviewed.[28-29] Notably, not only the dynamics[30-31] and distances between two spin labels as shown in the following can be analyzed, but also solvent accessibilities[32-33] and the polarity of microenvironment[34-37] are observable *via* EPR techniques.

The large amount of intrinsic sample properties rendered accessible by spin labeling lead to thorough development of site-directed spin labeling techniques.[38-39] Thus, SDSL is commonly used directly aiming for structure elucidation of (bio-)macromolecules using EPR techniques.[40] Labels used for this are for instance paramagnetic centers, chelated metal ions[41-43] or nitroxides.[44] Different label requirements depending on the projected measurements lead to a variety of spin labels that have been reviewed extensively.[45-47] Important characteristics are the chemical stability of labels and linkers, the procedures of label introduction and flexibility of both label and linker. While the former is mostly important for *in vivo* measurements, the latter are relevant especially for studies on structure and dynamics. Notably, also the spectroscopic properties of labels can heavily influence their usability in EPR studies. In the scope of this work, nitroxide based labels were chosen as the most suitable spin moiety and will be discussed in more details in the following (Figure 1 shows some common nitroxide labels).

Introduction of nitroxide spin labels to the target is typically done through site-specific binding to selected amino acids such as lysine or cysteine, the available nitroxide moieties mostly differ in ring size, anchoring groups and steric shielding of the unpaired electron.[48-54] An important aspect of spin labels is their rigidity. A high flexibility of the nitroxide moiety and/or the linker area is unlikely to introduce steric hindrance to the protein it is attached to, yet introduces additional flexibility impeding the interpretation of distance determinations. Rigid spin labels can, *e.g.*, bind to His-tags [55-56] or two cysteine residues in spatial vicinity,[57] leading to reduced structural freedom.[55-56] As this will lead to structural perturbation of the protein in many cases, small and flexible spin labels that bind to single amino acids are often used,[45-47] with the most abundant ones being methanethiosulfonate spin label (MTSSL) and 3-maleimido proxyl (Proxyl) shown in Figure 1.[58-60] These labels have been used extensively to study protein structure and dynamics.[61-62]

More flexibility in the label choice is achieved when the spin label is introduced into the amino acid sequence directly *via* peptide synthesis. This allows the usage of exceptionally rigid spin labels such as 2,2,6,6-tetramethyl-N-oxyl-4-amino-4-carboxylic acid (TOAC)[63-64] or 4-(3,3,5,5-tetramethyl-2,6-dioxo-4-oxylpiperazin-1-yl)-L-phenyl-glycine (TOPP)[65] in a site-specific and quantitative manner. These are depicted in Figure 1. For the synthesis of such constructs, one has to rely on solid-phase peptide synthesis which is limited to rather small peptides and not yet feasible for larger complexes.[51]

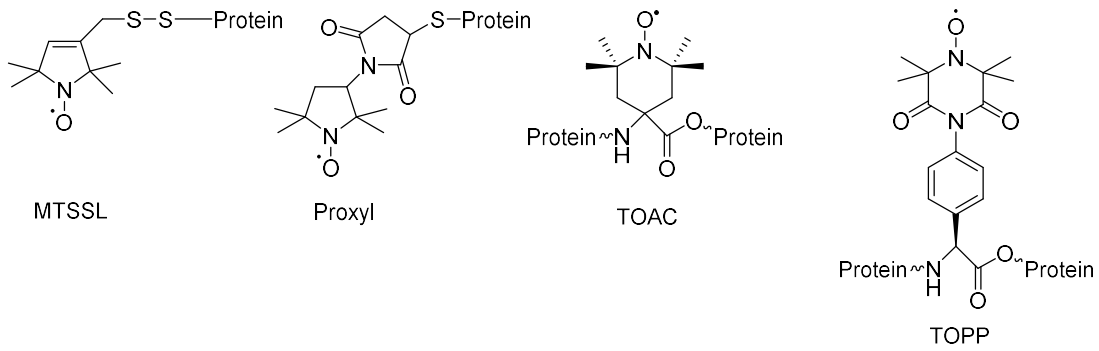

Figure 1: Spin labeling using either MTSSL or Proxyl attached to a cysteine residue in contrast the unnatural amino acids TOAC and TOPP incorporated directly into the peptide backbone.

In addition to the choice of a suitable label, the position at which it is introduced has to be carefully evaluated. This process is heavily dependent on the experiments to be conducted, some typical factors to take into account are listed in the following.

- *Labeling reaction yields*: Often a quantitative labeling can be expected for highly reactive spin labels. To ensure this, the amino acid chosen has to be located at the exposed protein surface. This can be evaluated using available crystal structures and scanning the residues by eye in a surface representation. In addition to this, a site-scan prediction of possible rotamers using *e.g.* MMM[66] or PyMOL[67] can exclude sterically problematic residues.
- *Perturbation of the protein*: Non-perturbing positions for the spin label should be chosen. Positions close to active sites or binding positions have to be avoided.
- *Optimal label distance*: The distance between the two spin label should be chosen deliberately. For distance measurements, the accessible distance range is between 1.5 to about 8 nm.
- *Spin label mobility at the labeled residue*: Label positions where the predicted rotamer population is sparse and confined to a smaller volume can be beneficial as the distance distribution will be less broadened by spin label movements. However, these positions can also exhibit less efficient labeling.
- *Label location*: When expected structural changes and their direction are known, beneficial positions can be chosen regarding the perspective of the measured spin-spin axis with respect to the expected molecular motion.
- *Native cysteines*: If native cysteine residues are present in the protein sequence, they can be used if they conform to the requirements above.
- *Non-labeled cysteines*: Remaining native cysteine residues have to be either completely removed or, preferably, retained as long as they are not expected to be accessible to labeling. Non-accessible cysteines can be due to these residues being hidden in hydrophobic pockets or deactivated in disulfide bridges. This reduces possibilities for protein native structure perturbation.

3.2. Rotational dynamics

In addition to the *static* observation of structural traits, the *dynamics* of intrinsically disordered proteins and protein regions are an important aspect of their structural ensemble. Conformational changes, as well as the degree of conformational freedom, are crucial indicators and thus spectroscopic techniques to assess these have been developed.

EPR spectroscopy is a particularly powerful technique to capture dynamics in solution. This involves the attachment of only a single spin label into the protein in an area of interest. The rotational dynamics of spin labels are reflected in the EPR spectra, with increased rotational correlation times leading to a spectral broadening that can be quantified (see Figure 2). These overall dynamics can be distinguished by the dynamics of the spin label itself (including its linker moiety), the protein secondary structure elements in the vicinity of the labeled residue and the rotation of the entire protein.[29, 68-69] Therefore, dissection of the apparent mobility can help understanding changes in the structural dynamics of *e.g.* proteins. For proteins that alter their backbone flexibility in the direct vicinity of the spin label, the overall spin label dynamic is often altered and thus detectable in cwEPR experiments. This has been shown and reviewed extensively.[70-71] In the following, the analysis of spin label mobility using cwEPR will be termed *mobility studies*.

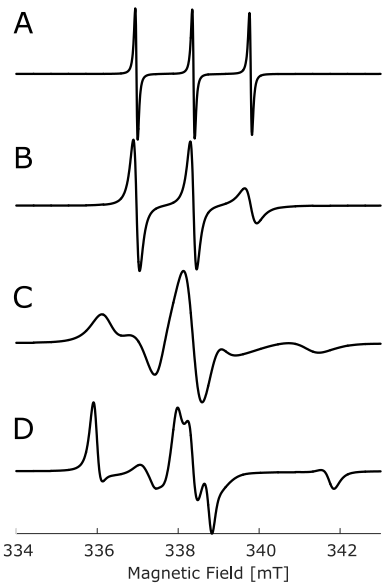

Figure 2: Mobility of a nitroxide spin label. The plots correspond to the spectra simulated at 9.5 GHz (X-Band) with rotational correlation times of 10 ps (A), 1 ns (B), 10 ns (C), 100 ns (D) in the fast (garlic function, A and B) or slow (chili function, C, D) regime using EasySpin.[72]

The description of experimental EPR spectra involves the full description of the spin Hamiltonian, leading to inherent spin parameters such as the g tensor in the Zeeman

term and the hyperfine tensor describing the splitting of energy levels due to the nitrogen atom in the unpaired electron vicinity for nitroxide spin labels. [29, 73] The analysis of experimental spectra and dissection of the underlying physics is typically done *via* solving of stochastic Liouville's equations readily implemented in software packages like EasySpin[72].

EPR has several characteristic traits that are important for studies on protein dynamics. A full, quantitative description of experimental data not only allows for the determination of *e.g.* rotational correlation times, but furthermore the discrimination between multiple spin species. If the sampled protein exhibits several conformational substates that differ from each other in the dynamics around the spin label, these can be quantified using spectral analysis methods. In addition, the temperature at which mobility studies are conducted is precisely adjustable in a large range including biological temperatures. Therefore, it is possible to use experimental conditions that reflect an environment closes to the native *in vivo* state. Especially for temperature-dependent equilibria, this dependency can be probed over a large range of temperatures.[74]

3.3. Long-range distance restraints by EPR

3.3.1. Pulsed EPR distance determination

The introduction of a second spin moiety to the protein enables structural characterizations based on spin-spin distances. The following paragraphs provide a brief overview of experimental and theoretical aspects of pulsed EPR measurements while referring to more detailed literature.[75]

The dipolar interaction between two unpaired electrons is proportional to the inverse cube of the distance, enabling the path to spectroscopic techniques assessing these distances.[76] More importantly, insights are gained not only on the distance between two spins but on the full distribution of distances present in the samples. In typical ensemble methods like FRET, an average distance information for all observed molecules is obtained. This sets EPR distance measurement apart from these, allowing the analysis of distance distributions that include more than one distance. Multiple, discrete structural substates in *e.g.* proteins are thus rendered accessible. Notably, the use of small and non-perturbing labels is beneficial for both high experimental precision as well as low structural disruption introduced to the target.[77] The accessible range of distances includes short distances of around 1.2 nm[78] as well as long distances up to approximately 8 nm without the need to select suitable labels for the expected distance range. In very

favorable cases that include deuteration of samples and sparse spin labeling, the maximum measurable distances can reach 16 nm.[79-80]

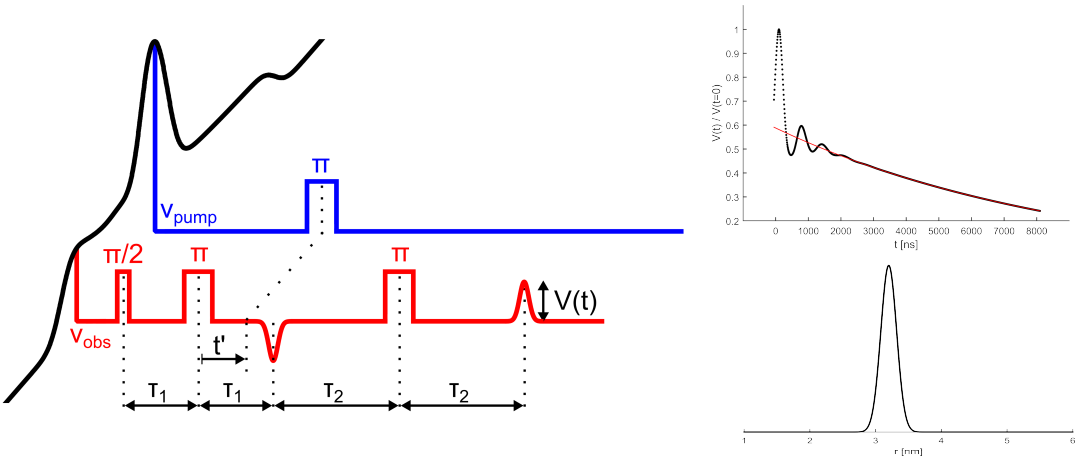

Figure 3: Left: Two frequency, four pulse DEER experiment with excitation in separated spectral regions (nitroxide X-Band spectrum illustrated in black). The resulting raw data trace is shown in the top right. After background correction (red line) and Tikhonov regularization (not shown) the distance distribution is obtained (bottom right). Adapted from Hintze, 2011.[81]

Typically, samples are flash-frozen in liquid nitrogen to yield a glassy state that inherits the structural equilibria already present in the solution.[82] While distances measurements at room temperature have been proposed using either nitroxides[83-85] or triarylmethyl labels[86], the majority of measurements are carried out at cryogenic temperatures to optimize spin-relaxation kinetics and avoid reorientation of the spin-spin vector due to molecular motions. Depending on the spin labels used and the experimental properties, a variety of different measurement procedures are available. [87-88] Pulsed techniques include: double-quantum coherence (DCQ)[89-90], single frequency technique for refocusing dipolar couplings (SIFTER)[91] or RIDME[92]. The majority of distance measurements are conducted using double-electron electron resonance (DEER) which is also called pulsed electron-electron double resonance (PELDOR)[93-98] and depicted in Figure 3. All of these methods share the goal of separating the dipole-dipole interaction from all other contributions to the spin Hamiltonian[99-100] which is necessary for distances exceeding approximately 2 nm.[87] Smaller distances can be measured using cwEPR as the dipole-dipole coupling leads to significant spectral broadening.[101]

The extraction of distance distributions from raw experimental data is typically done using model-free approaches, opening the path for structural analysis that includes not only the determination of secondary structure changes, but also observation of large domain and tertiary structure movements. Notably, the distance measured between the two spin labels does not only include the separation by the protein backbone structure they are attached to, but also uncertainty introduced by flexibilities inherent to the label

and its linkage to the primary sequence. While these motions can be modeled with a rotamer approach suggesting possible linker dynamics and the impact on the distance distribution,[102] this implies that a structure model is already available and the experimental data can be used to evaluate the proposed structure.

De novo structure determination, *i.e.* without the assumption of a structural model, is far more challenging. The distance constraints are typically sparse and ambiguous because of the additional label flexibility. While the number of distance constraints observed can be increased, this involves large experimental effort and more labeling positions that might lead to perturbations in the protein structure. Therefore, *de novo* structural analyses are usually conducted as a joint approach using multiple techniques involving *e.g.* nuclear magnetic resonance methods and molecular dynamics (MD) simulations.[103-107]

3.3.2. Multilateration

EPR distance determinations are a powerful tool, allowing more advanced analysis procedures such as multilateration. The ability to measure precise distances between multiple label pairs renders access to determine the coordinates of a spin label based on distance distributions from known locations. This technique is termed multilateration, triangulation or localization in recent literature.[66, 108-110] As the term triangulation is slightly misleading in that the number of distance constraints used is variable, the terms multilateration or localization will be used in the following. It should be noted that this approach distinguished itself from known techniques used in GPS in that not only the distance to the reference points but also the width of the distribution is included in the calculations.

This technique as an EPR tool was first introduced in 2002[111] and was utilized for the location of lipids[110] and metal ions in proteins[108, 112-113] as well as for the construction of structural models in protein complexes.[109, 111, 114-115]

Experimentally, a localization is carried out by measuring a set of pairwise distances between the point of unknown location and different reference points that should be spread evenly in a three-dimensional space to achieve the best possible precision. At least three distance sets are needed to result in an ambiguous localization with two different possible positions, addition of four distance pairs results in an unambiguous localization. The inherent dynamics of the attached spin labels increases the uncertainty of the positioning of both the unknown position as well as for the reference points and is thus incorporated into the calculations.[66]

3.4. Secondary structure content reported by CD spectroscopy

An inherent property of chiral molecules and structures is the distinct difference between the absorption properties of left- and right handed circularly polarized light. This effect is termed circular dichroism (CD) and depicts a valuable tool for not only the identification of stereo centers in chemistry related aspects[116] but also for the determination of secondary structure contents in protein samples since decades.[117] In this short paragraph, only the most important aspects of CD spectroscopy necessary in the scope of this work will be covered, for a more detailed explanation of the underlying principles extensive reviews are available.[117-120] Shortly, proteins feature chirality not only by chiral amino acids (19 out of the 20 natural occurring amino acids are chiral), but also through the formation of secondary structure elements such as α-helices. The wavelength-dependent circular dichroism can be accessed experimentally using alternating circularly polarized light which is typically generated using a photo-elastic modulator[121] and subsequently guided through the diluted protein sample (typically in aqueous solution) in a quartz cuvette. The transmitted light is the analyzed by a photon-multiplier tube, resolving the difference in absorption between left- and right handed polarization.

Secondary structure elements such as α-helices and β-sheets as well as the absence of these elements (often misleadingly termed random coil instead of unordered) impose distinct chiral characteristics and thus CD signals (see Figure 4), allowing classification of proteins based on the presence of secondary structures. While a qualitative analysis is facile for samples containing exclusively one single secondary structure element, a quantitative analysis is impeded when the sample contains a mixture of several structural elements. Nevertheless, analysis tools to estimate the secondary structure contents of given samples are available.[118-120] One prerequisite for the analysis of secondary structure elements is the need for precise control of temperature, path lengths and sample concentrations. While these can be adjusted easily for larger sample amounts, the usage of low concentrated samples and reduced path lengths that are often necessary in studies on proteins severely hinders a quantitative analysis.

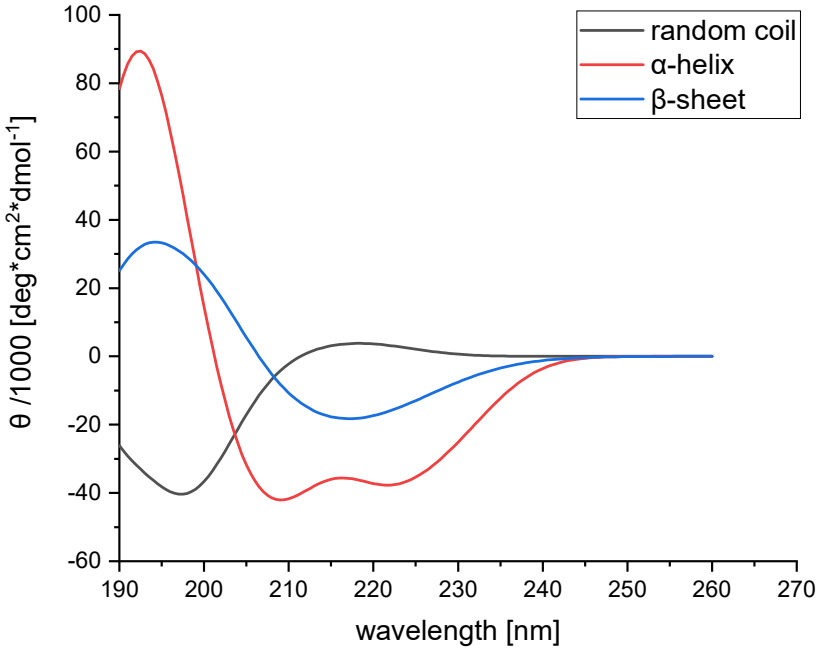

Figure 4: Simulated CD spectra for proteins in dependency of their secondary structure elements. Based on the theoretical description of CD signals from de Jongh et.al, 1994.[122]

The combination of all of the techniques shown above represents a powerful toolbox enabling experiments to gain insights into protein structure, folding and refolding processes.

In the following chapters, this will be applied to two important proteins already mentioned above: ASYN and p38α, with the former representing an intrinsically disordered protein with virtually no stable secondary structure elements in solution and the latter a well-folding protein with only a discrete, secondary structure-lacking region within its sequence. Both proteins thus represent molecular disorder in different dimensions while both being highly important in a biological context. ASYN and p38α will be introduced in more detail in the beginning of each representative result chapter, starting with ASYN.

4. Local features of the intrinsically disordered protein alpha-synuclein

4.1. Alpha-synuclein and its structural diversity

The intrinsically disordered protein alpha-synuclein (ASYN) consists of 140 amino acids and is abundantly present in human neurons. While its physiological function is poorly understood,[123] malfunctions are tightly linked to a variety of disorders such as neurodegenerative diseases.[124] This imbalance is mainly caused by the ambivalent character of the ASYN structure that ranges between complete lack of structuring to well-defined fibril formation that leads to loss of neurons in neurodegenerative diseases.[125-129] The primary sequence can be divided into three regions: The N-terminus ranging from residue 1 to 60, the hydrophobic non-amyloid component (NAC) and the acidic C-terminus. Of note is also the VATV motif located in the N-terminus, the deletion of this motif heavily influences aggregation kinetics.[130] While most studies are focusing on the pathophysiological impact of ASYN, the physiological function of ASYN is certainly equally important, *e.g.* it might be an important factor in DNA repair processes.[131] This highlights the crucial necessity of spectroscopic techniques and studies that allow deeper insights into ASYN function as well as malfunction. The following paragraphs contain a brief overview highlighting the most important structural aspects for the scope of this work while referring to more detailed literature when suitable.

With regards to physiological malfunctions, aggregation of ASYN is crucially involved in disease symptoms. Extensive studies on this pathway have been conducted and reviewed.[126-129, 132-133] In this study though, the focus resides on the structure of monomeric ASYN in solution and during interaction with membranes.

In absence of binding partners, ASYN typically adopts a structurally undefined disordered conformation with high flexibility. However, a disordered state does not necessarily involve a complete lack of structural traits. Recent studies are debating the monomeric state of ASYN in solution versus an equilibrium of relatively stable multimers.[134-136] Long-range contacts found for isolated ASYN point at local structuring already present in solution.[137] First in-cell measurements conducted using both NMR and EPR techniques hint at an unordered state of ASYN that remains in a cellular context.[138-139] These findings are especially interesting given the presence of large amounts of lipids and membranes in a cellular environment.[140] The disordered state of ASYN in cells is still under debate[141] and recent FRET studies suggest the presence of several distinct structural ensembles in cells.[142]

In vitro experiments have shown various structural changes upon ASYN interaction with binding partners, giving important insights into possible cellular roles. As already

mentioned, an important interdependence has been found with lipid membranes.[143] Extensive studies on different lipid bodies have been conducted that show a structural shift towards an alpha-helical structure of ASYN.[105, 142-146] In addition to membranes, other binding partners such as metal ions have been proposed, again understating the ambiguity and variety of molecular dependencies for ASYN.[144]

Clinical studies have identified several characteristic point mutation in the ASYN sequence that influence disease traits and are found in the hereditary form of Parkinson's disease.[133, 145-146] Two of these located near the N-terminus are A30P and A53T, impacting the aggregation properties during fibril formation and therefore impose a great interest with regards to disease pathology.[133, 147] Prior to this, these point mutations were further shown to affect the binding to membranes[148-149] and the helical structuring in their direct vicinity upon interaction with lipids, suggesting a mechanistic impact of the point mutations already for non-aggregated ASYN.[150-151]

In addition to disease mutations, changes in the protein structure can occur *via* post-translational modifications (PTMs). These can occur during or after translation of proteins in cells, altering the biological function of proteins or marking them for other cellular processes. For ASYN, important PTMs are nitration and phosphorylation which can occur on serine and tyrosine residues encoded in the primary sequence.[152-154] In addition, studies have been conducted focusing on acetylation,[129] O-GlcNac modification[128] or ubiquitination.[155]

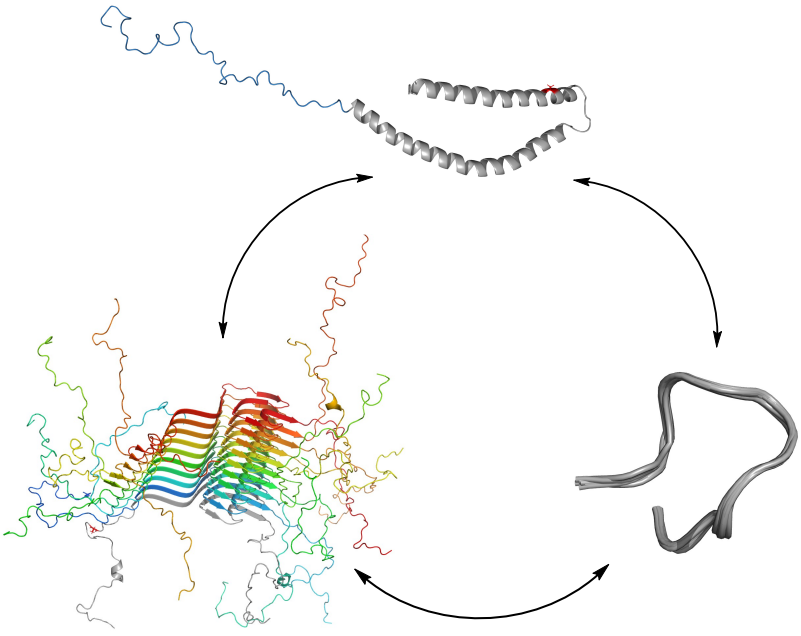

Figure 5: Structural variety of ASYN. Unordered fragment ensemble adopted in solution (right, based on PDB 2JN5), helical structuring adopted upon membrane binding (top, based on PDB 1XQ8) and fibrils formed in ASYN aggregates (left, based on PDB 2N0A). the disease mutation A30P is depicted in red for helical ASYN (top).

The studies mentioned above focused on structural changes for ASYN in the presence of external influences such as binding partners or molecular crowding in cellular systems, assuming to origin from an unstructured ensemble. The native structure of ASYN under *in vitro* conditions and in absence of binding partners does not show significant secondary structure formation. In order to understand conformational transitions induced by external triggers, potential structuring already present in the native state has to be considered. This first step from complete disorder to local ordering is crucial for the formation of stable secondary structure elements. The formation of transient structures, *i.e.* short-lived secondary structure motifs, can be crucial factor in protein activities such as membrane of substrate binding. The aforementioned dynamic flexibility has been discussed and reviewed extensively.[155-157] Indeed, recent NMR studies suggest a propensity for transient secondary structuring for isolated ASYN.[129] Several distinct substates were isolated for ASYN, depending on the solvent constitution.[156] Additionally, MD simulations directly suggest transient secondary structure formation.[157-158] These findings suggest that there might be transient or local ordering already present in isolated ASYN. Transient and thus short-lived structuring of ASYN could lead to profound impacts in substrate interactions, capturing those would thus be an important step towards a deeper understanding of the biological implications of protein disorder. These questions which will thus be assessed in chapter 4.2.

4.2. A combinatorial spectroscopic and simulation approach

Transient ordering in an otherwise structure-deficient equilibrium is an important trait to assess, as this might have an impact on several biological interactions such as protein-protein contacts or post-translational modifications.[136, 159-162]

During this study, a combinatorial approach using circular dichroism spectroscopy, pulsed electron paramagnetic resonance techniques and molecular dynamics simulations was developed to assess structural features of α-synuclein in different environments. The combination of spectroscopic and theoretical techniques to assess structural equilibria has been successfully shown to be able to ameliorate the precision and clearness of structural analyses.[20, 163] Therefore, a very defined experimental system had to be found that reduces the number of experimental variables to a minimum whilst providing a platform that allows a direct comparison of experimental datasets with simulated structure pools. This necessity precludes the use of complex environments (such as cellular systems) as atomistic simulations are often limited to monomolecular solvents. With a suitable system at hand, structural traits and changes should be monitored while unique environmental parameters like the solvent were changed. While distance distributions obtained with DEER do not allow a direct allocation to protein structures, ensemble pools obtained with MD simulations can be used to narrow down the quantity of possible structures, resulting in deeper insights into local or transient ordering. It should be noted that a transient ordering of structure usually happens on timescales in the nanosecond range. This is much faster than the typical freeze times of hundreds of milliseconds during shock-freezing of samples during the preparation of DEER samples.[164] Thus, transient structures that fold and unfold rapidly at ambient temperature will most likely not be captured in this process. However, the presence of transient structures at ambient temperatures likely involves equilibria that are also populated around the glass temperature of the solvents used, *i.e.* around 100-160 K.[165] These equilibria are then captured as a snapshot of populated states, enabling deeper insights into the underlying dynamics.

In order to achieve unambiguous insights into structural traits, several key points have to be optimized carefully. From an experimental point of view, high precision in the determination of distance distributions is needed. This involves spin labeling procedures with labels that are unambiguous in their conformation. In many cases, approximations such as coarse-graining are used to describe structural equilibria of proteins. In this study, the necessity of explicit structure description excluded these and an approach using an atomistic level of description was developed. These aspects led to the development of a system using peptide fragments instead of full-length ASYN. Peptide fragments as a model system for the description of full-length protein have been

proven as a valuable tool in structural studies for ASYN in earlier studies, thus showing the potential of a fragment approach to study structural ensembles.[166-168]

4.2.1. A peptide system as a model platform for ASYN

The peptide fragments chosen are located in the membrane-binding N-terminus of ASYN and include the disease mutant position A30P that has been found in patients with hereditary Parkinson's disease and whose implications are of great interest.[169-170] As noted above, peptide fragments offer several significant advantages on both experimental and simulation aspects; the full synthesis *via* solid-phase peptide synthesis (SPPS) techniques allows the direct control of primary sequences and thus incorporation of several different spin labels that differ in their attachment functionality and, most importantly, in their structural flexibility that is crucially linked to the achievable precision in end-to-end distance descriptions of structures. In addition, the size reduction to shorter peptides is crucially important for atomistic simulations.

Ten different peptide fragments were chosen as a starting point for further studies, these are depicted in Figure 6. These constructs contain wild-type sequences without further modifications and are located around the membrane binding N-terminus of ASYN. As the C-terminal region has not been found to exhibit large structuring upon interaction with binding partners, the focus towards N-terminal areas was preferred. Additionally, known delete and disease mutations are located in the chosen regions (see below). This resulted in a library of ten different peptide fragments that were synthesized *via* SPPS (carried out by Biosyntan, Berlin): Peptides P1 and P2 that are starting from the ASYN N-terminus and differ in the presence or absence of the delete region 2-11 that is crucial for membrane binding.[171] P3 and P4 are starting from residue 19, incorporating the wild-type derived alanine or the known disease mutation A30P. P5 is located in the same are while being shortened, facilitating MD simulations for variable evaluation. P6, P7, P8 and P9 are located at the end of the N-terminus and incorporate either the wild-type sequence, the disease mutation A53T, the deletion or doubling of the residues 52 to 55 (VATV, see 4.1).[130] These were fully characterized to selectively choose a reduced amount in further studies involving a combinatorial EPR and MD approach. The longest peptide, P10, spans around this area to represent a larger portion of ASYN, bridging the gap between fragments and full-length ASYN.

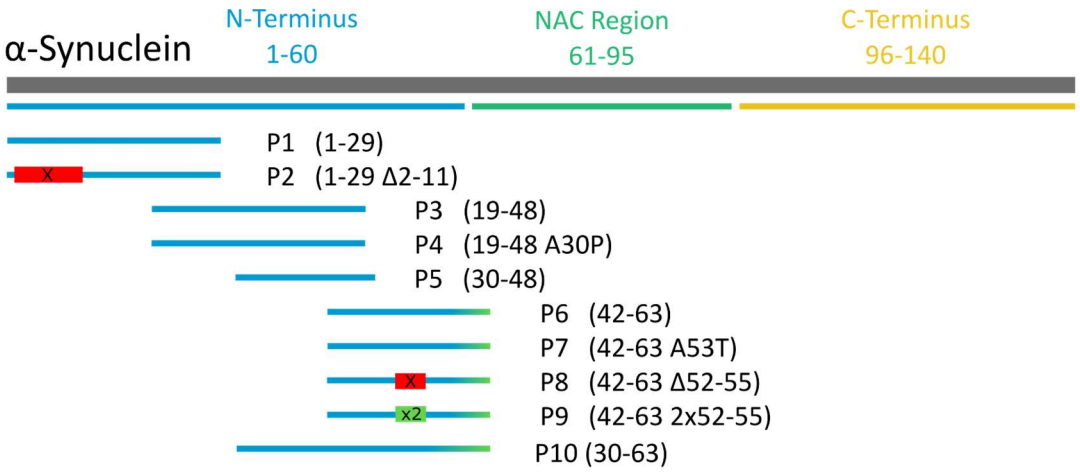

Figure 6: Library of ten different peptide sequences used to evaluate their behavior and usability for further studies. The sequence of ASYN is depicted in grey, common delete mutations are depicted in red, sequence doubling is shown in green.

The establishment of a model system based on peptide fragments instead of full-length ASYN is crucially coupled with the verification that these peptides represent the biological functions of ASYN as good as possible. While peptide fragments have been used as model systems in earlier studies,[166-168] the structural integrity and comparability to the full-length protein had to be evaluated.

This was done mainly using CD spectroscopy, as it is a fast and reliable tool to follow main structural traits of proteins. As already noted above, ASYN resides in a broad, unordered structural state in an aqueous environment and in absence of relevant binding partners. Therefore, a CD signal reflecting an unordered state is expected for all ten peptides. Structural ordering appearing in the CD signal for some of these peptides in aqueous solution would exclude their applicability as model compounds.

Measurements of all peptides were carried out in water, resulting in spectra representative of unordered states (see Figure 7 top). No significant aberrations were found for the ten model compounds, implying that the absence of clear secondary structure elements observed for ASYN is retained in the peptides (for details, see 8.1.1).

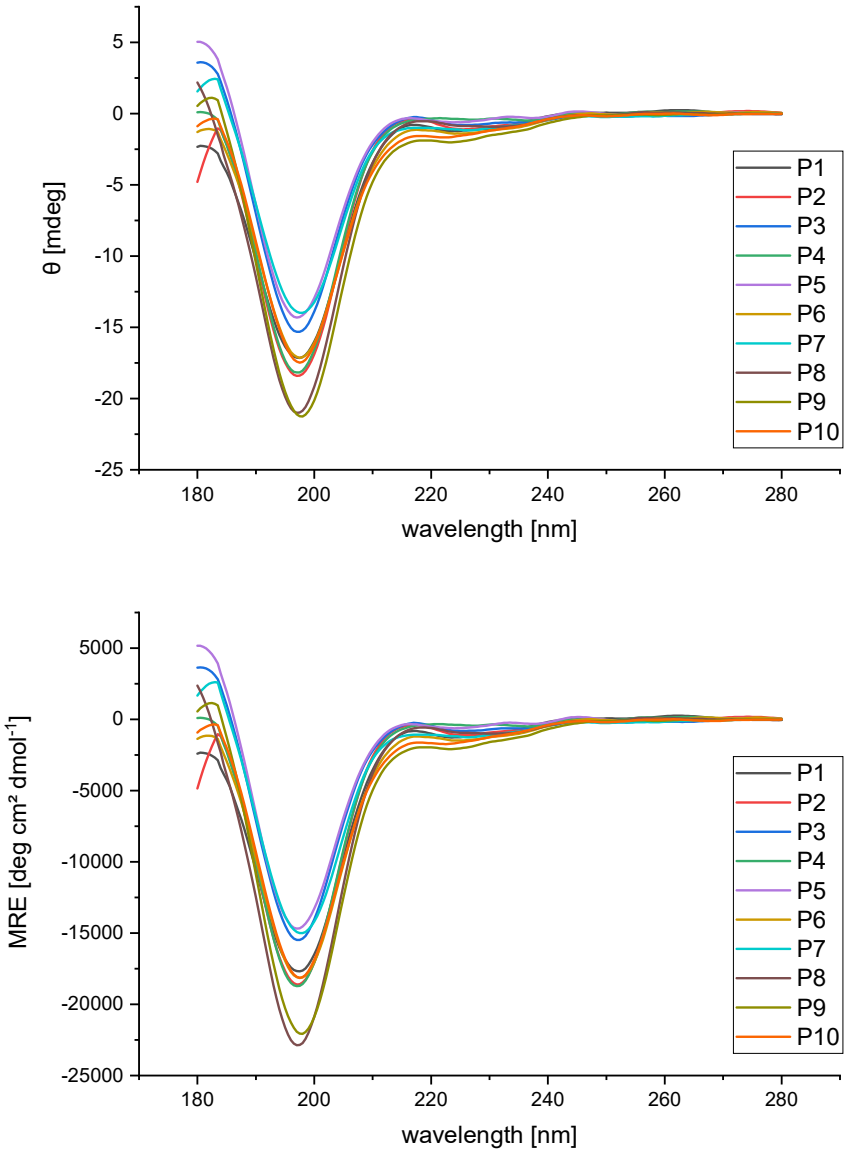

Figure 7: Top: CD data obtained for the ten peptide fragments in aqueous solution (Milli-Q, see experimental details) with a concentration of 50 µM. For experimental details, see chapter 8.1.1. Bottom: converted dataset to units of mean residue ellipticity (MRE). Due to experimental constraints as explained in chapter 8.1.1, conversion to MRE was omitted in further spectra.

As the peptides showed the expected behavior in aqueous solution, the ability to adopt helical conformations and binding to lipids was assessed. A particularly interesting tool to stabilize α-helical structures in the scope of this study was the addition of alcohols that have been shown to support helix-formation and stabilization.[172] Here, methanol was used as a solvent to assess the tendency of the peptide fragments to form helical structures. CD spectra were collected after a solvent exchange to pure MeOH (see Figure 8). All spectra were strongly differing from their counterpart in aqueous solution, which is in line with a structural change from an unordered to a more helical state. All spectra are representing a structural state consisting mostly of α-helical states (see Figure 4 for reference). Several peptides show spectra that can be interpreted as a virtually full helical ensemble (*e.g.* P5, P4, Figure 7) while others seem to consist of a slightly more

mixed secondary structure content (P3, P9). This could be due to the presence of beta-sheet contents in slightly aggregated peptides, however the difference in spectral shapes is too minor for a meaningful interpretation.

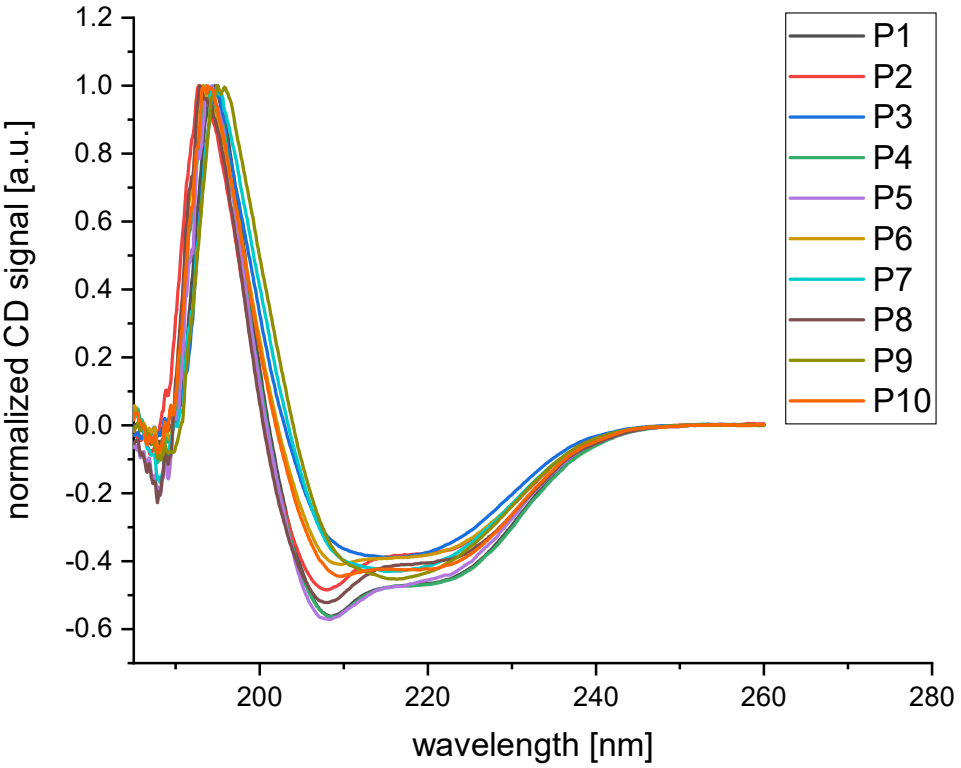

Figure 8: CD spectra obtained in pure methanol, showing a clear tendency towards alpha-helical conformations for all ten peptides. For experimental details, see chapter 8.1.1

The collected spectra show structural changes for all peptides upon solvent exchange, understating the helical tendencies also found in full-length ASYN. In a biological context, ASYN adopts a helical conformation upon binding to membranes. This has been evaluated for membrane mimics such as large unilamellar vesicles (LUVs).[173] Therefore, all peptides have been incubated with LUVs consisting of POPG (see chapter 8.1.1) to assess their binding characteristics (see Appendix, Figure A. 1). All peptides, with the exception of P8, show significant structural changes *via* a CD signal shift towards an alpha-helical conformation. This understates that these model peptides reflect the full-length protein in biologically relevant environments. The peptide P8 incorporates a well-known delete mutation of a crucial binding motif VATV already studied for ASYN. Indeed, the CD spectrum for P8 of mostly unordered and β-sheet resembling characteristics, suggesting that no binding to LUVs occurs.

Based on these results, the proposed peptide system was presumed to represent full-length ASYN in an acceptable multitude to present this as a suitable model system. A choice of three peptides were chosen for further experiments (see Figure 9):

- P5, termed **ASYN-P short**. This is a short peptide consisting of the residues 30 to 47 in the spin-labeled case and is used for the evaluation of experimental and simulation methods.
- P3, termed **ASYN-P WT**. This is a longer peptide based on residues 21 to 37 of wild-type (WT) ASYN.
- P4, termed **ASYN-P DM.** This fragment contains the same sequence as P3 and additionally includes the disease mutation A30P (DM) used to evaluate the effect of this mutation on the structural equilibrium.

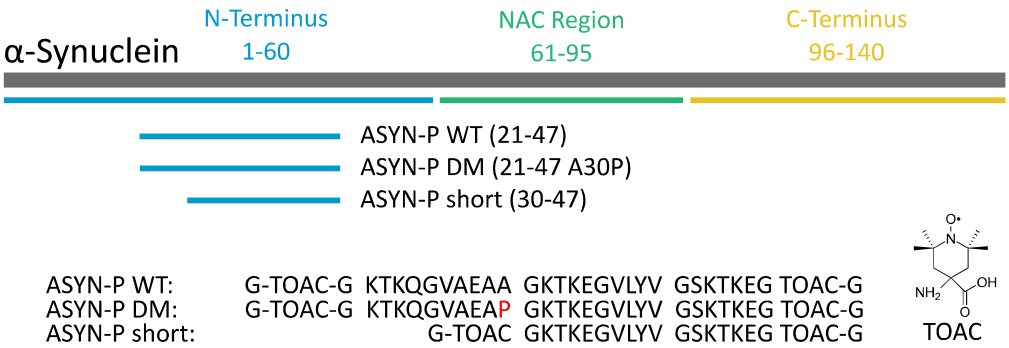

Figure 9: Spin labeled peptide fragments used for further studies using EPR and MD simulations. The primary sequence, including the unnatural amino acid TOAC (see chapter 3.1) is shown.

For these three peptides, beginning with ASYN-P short to evaluate all the procedures, a suitable approach for spin-labelling and subsequent distance measurement studies was developed. In parallel, MD simulations were carried out in the group of Christine Peter (Universität Konstanz).

4.2.2. SDLS and EPR distance measurements in a controlled environment

In order to obtain experimental datasets that are comparable with MD simulations, a suitable system to control important variables in EPR measurements had to be found. This included the choice of spin labels and optimization of all measurement parameters as well as assessment of solvent, cryoprotectant and freeze time effects.

Using synthetically produced peptides, several label attachments were feasible. Standard nitroxide spin labels such as MTSSL can be attached to cysteine residues introduced to the primary sequence. In addition to this, rigid spin labels incorporated as unnatural amino acids can be used (see chapter 3.1). The high rigidity of *e.g.* TOAC has the advantage of a vastly reduced ambiguity introduced by label flexibility.[84] This

facilitates the assignment of changes in the distance distribution to backbone flexibilities. Both approaches were conducted, allowing for a comparison of these labeling techniques.

Attachment of MTSSL was done with peptide fragment P5 that was modified with cysteine residues at both termini. These were subsequently labeled with MTSSL and isolated using chromatographic separation (see chapter 8.1.1 for labeling details), resulting in a virtually quantitative double labeling degree. TOAC spin labeling was carried out synthetically (by Biosynthan, Berlin) and involved encapsulation of the unnatural amino acid TOAC with neighboring glycine residues to circumvent issues with terminally accessible TOAC moieties (see chapter 8.1.1 for details). Again, quantitative double labeling was achieved.

With both variants of P5 or ASYN-P short at hand, EPR distance determinations were carried out in both aqueous environment (see Figure 10) as well as in methanol (see Figure 11).

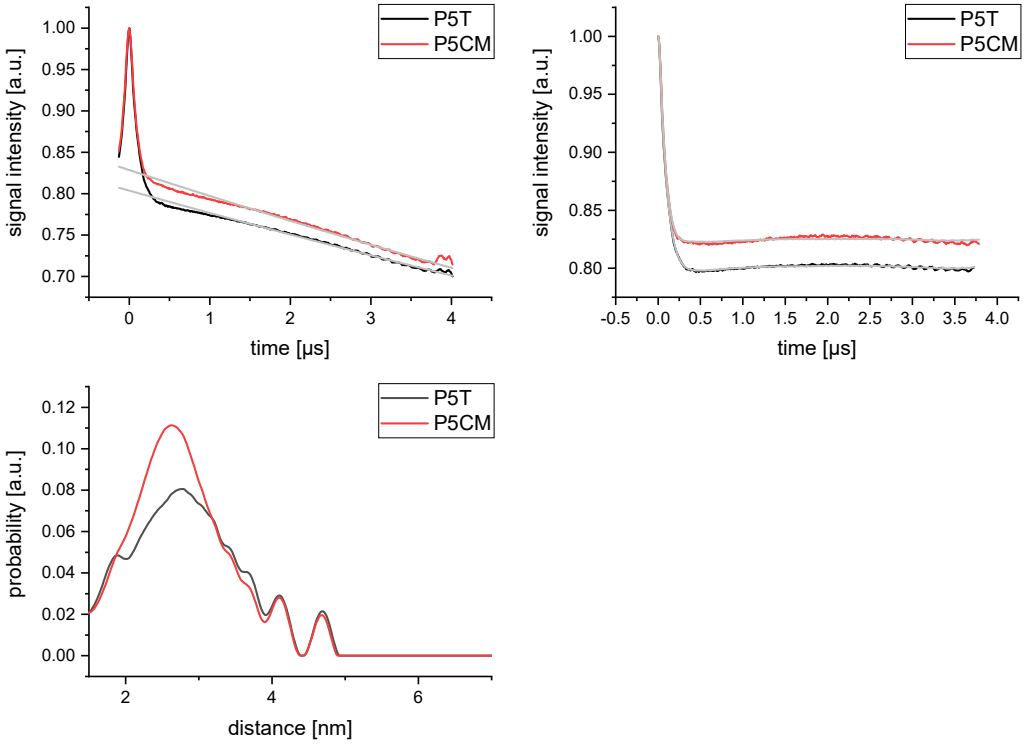

Figure 10: Distance determinations carried out with the P5 constructs bearing TOAC (P5T, black) and MTSSL (P5CM, red) in deuterated water. Top left: Raw data traces with the corresponding background fits (grey). Artifacts at the end of DEER traces were cut from the data during form factor calculation. Top right: resulting form factors and the fits (grey) resulting from Tikhonov regularization. Bottom: Resulting distance distributions. For analysis details, see chapter 8.1.1.

Distance determinations in aqueous environments lead to broad distributions for both MTSSL and TOAC labeled samples. Notably, despite the larger inherent flexibility there is no significant broadening of the distance constraints observable for MTSSL. Moreover, the shapes of the distance distributions are very similar, suggesting that in water the predominant mechanism leading to distribution broadening is the conformational flexibility of the peptide itself and not the spin label dynamics. While small differences in the modulation depths are observable, these are caused by experimental deviances such as non-equal pump pulse lengths (see chapter 8.1.1).

For methanol, the obtained distance restraints are significantly narrower than for aqueous environment (see Figure 11), correlating with the shift towards more rigid helical structuring of the peptides as already observed with CD spectroscopy. In methanol, significant differences rise in the distance distributions. MTSSL-labeled samples yield broader, slightly multimodal distance distributions that are shifted towards longer distances. With TOAC, on the other hand, narrow and unimodal distributions are obtained. Here, the restricted mobility of TOAC allows for an unambiguous interpretation of the unimodal, restricted flexibility in a helical conformation.

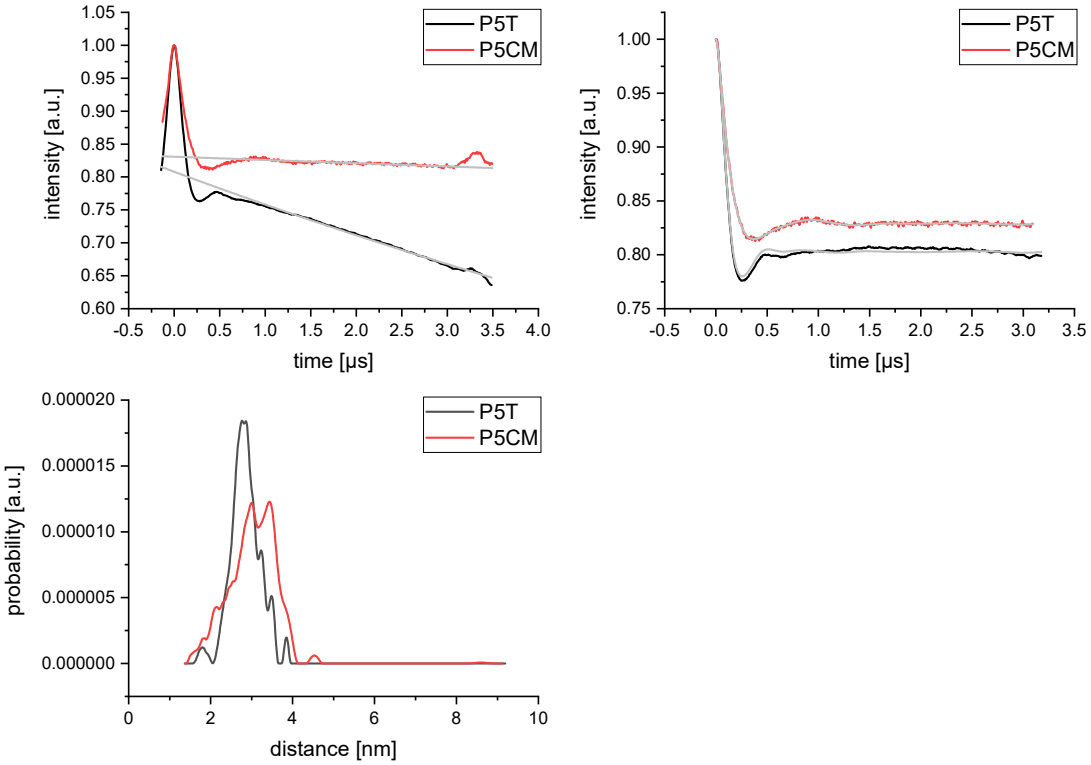

Figure 11: Distance determinations carried out with the P5 constructs bearing TOAC (P5T, black) and MTSSL (P5CM, red) in deuterated methanol. Top left: Raw data traces with the corresponding background fits (grey). Top right: resulting form factors and the fits (grey) resulting from Tikhonov regularization. Bottom: Distance distributions obtained *via* Tikhonov validation. For analysis details, see chapter 8.1.1.

Considering the less ambiguous results obtained with TOAC for rigid structures, this approach was chosen for subsequent measurements. Addition of terminal TOAC residues minimizes the probability for protein perturbation. CD spectra were collected, directly comparing the TOAC labeled ASYN-P short with the unlabeled variant in aqueous environment (see Figure 12). No perturbation from the unordered state induced by TOAC could be observed.

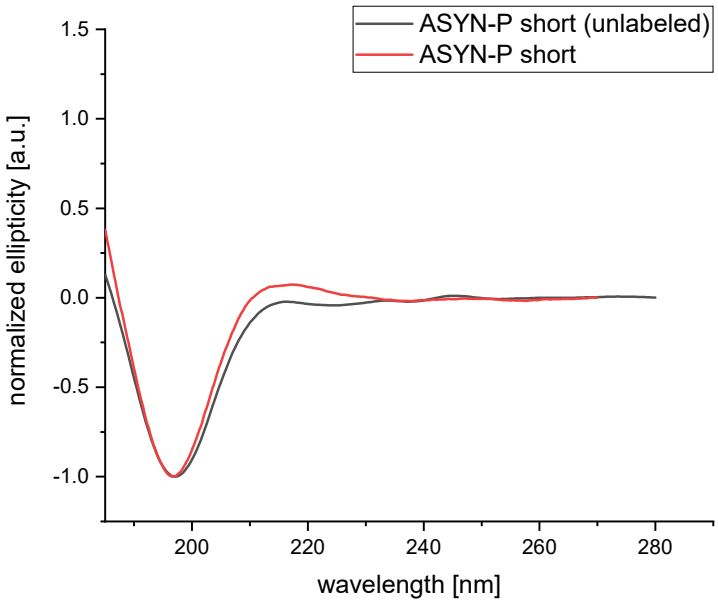

Figure 12: CD spectra obtained for TOAC labeled ASYN-P short (red) and the EPR silent peptide lacking TOAC label (ASYN-P short (unlabeled), black) in aqueous solvents. No major deviations are observable in both spectra, suggesting an unordered state that is undisturbed by the addition of TOAC labels.

To obtain distinct insights into structural traits using EPR distance measurements, the data quality has to be sufficient to discriminate minor deviances in the distance distribution. Changes such as a shift in the mean distance distribution can be simulated as raw data traces with artificial noise levels (see Figure 13). As a rough indicator of the required data quality, two distance distributions composed of a Gaussian shape that slightly differ in their mean distance were simulated (Figure 13, left). This change of 0.3 nm was converted into raw data traces and mixed with noise levels that are achievable using a carefully optimized measurement setup as seen in the following datasets during this chapter. In the zoom inset in Figure 13, right, significant deviances in the data traces are shown that are retained after Tikhonov validation in the resulting distance distributions (Figure 13, bottom). This denotes that distinguishing between small distribution deviances is possible with high quality datasets, implying the necessity to carefully optimize experimental variables.

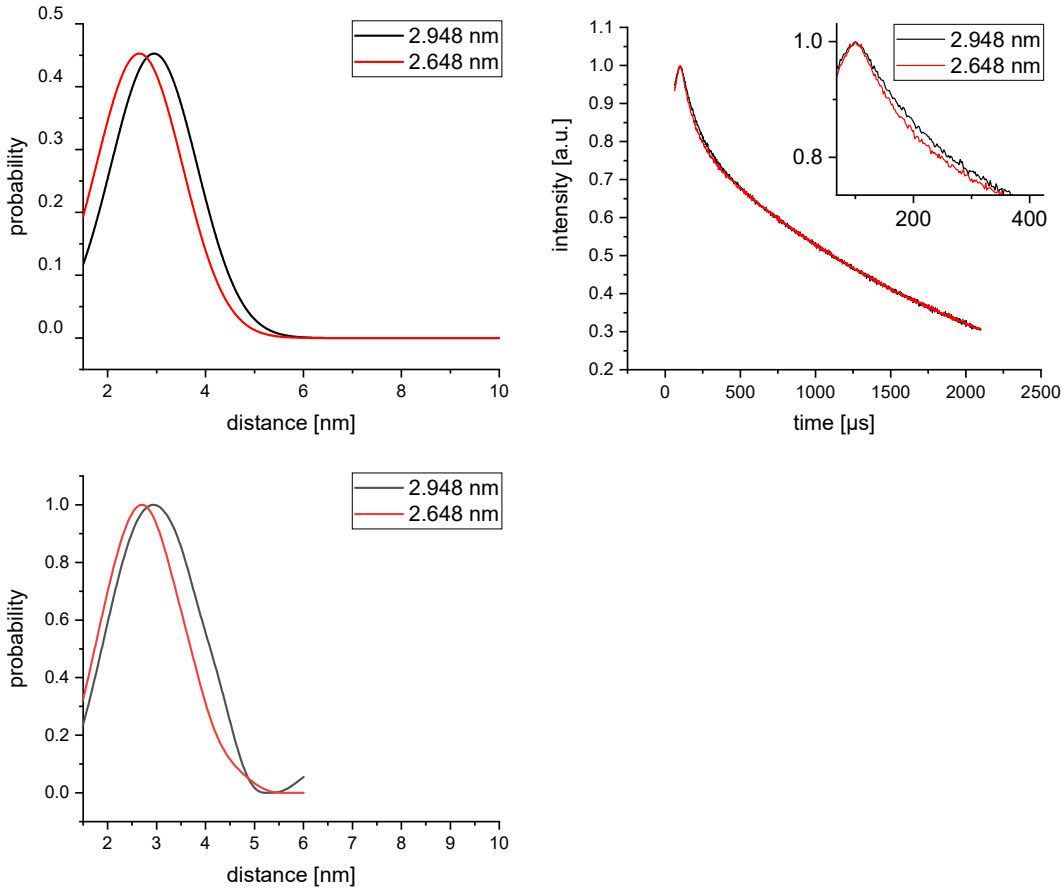

Figure 13: Top left: Two simulated Gaussian distance distributions that differ by 0.3 nm in their mean distances. Top right: Raw data traces based on the corresponding distance distributions, mixed with a background function and artificial noise. The inset shows the magnification of the first data points were differences are the most distinguishable. Bottom: Resulting distance distributions after background correction and Tikhonov regularization. The simulated distances are recovered with high accuracy.

For the given experimental setup, high quality data was obtained by the optimization of several parameters. For the peptide samples, the spin concentration was optimized to result in high signal levels allowing for easy separation of intermolecular and intramolecular contributions (for more details, see Jeschke, 2012)[174]. Deuteration of all solvents was pursued, this helps prolonging T_m relaxation times and subsequently improving signal-to-noise ratio or the maximum achievable d_2 time. With the resonator setup used, a critical step was to optimize resonator bandwidth as reported by the Q factor. This was optimized thoroughly using a model compound (see Figure A. 2).

To evaluate the solvent environment, MD simulations (as introduced later in this chapter) for aqueous solutions are carried out using solely water molecules as a solvent. This was also true for the EPR measurements performed using either Milli-Q or deuterated water, imposing an artificial environment that is significantly differing from cellular systems. To estimate the impact on the solvent regarding salt concentrations and pH values, samples in partially deuterated TRIS (tris(hydroxymethyl)aminomethane)

buffer (see chapter 8.1.1 for details) were prepared and measured. In Figure 14, datasets produced in both Milli-Q and TRIS buffer are depicted. After removal of the background function, the resulting form factors show no significant deviations. With this, the distance distribution for both samples is expected to be virtually equal for the given signal-to-noise ratios.[1]

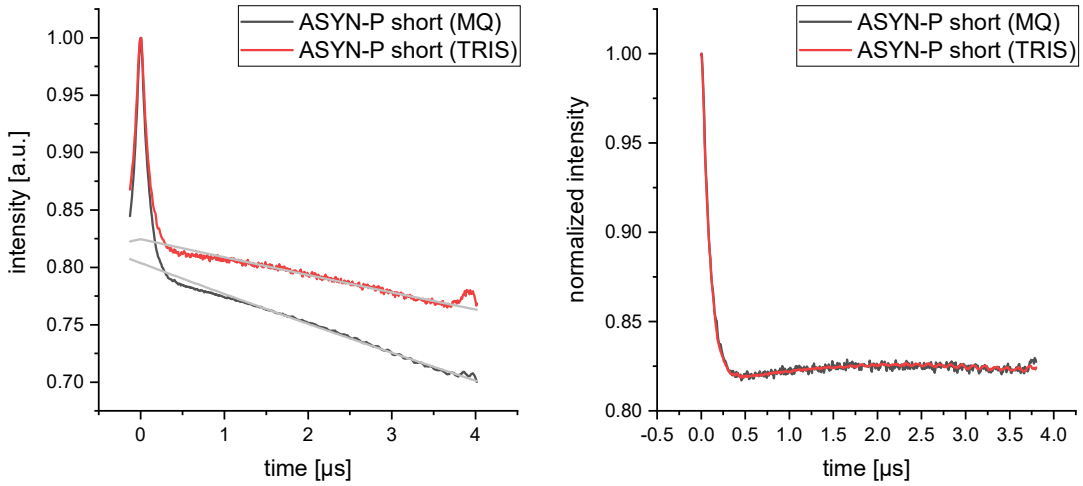

Figure 14: Left: Raw data traces obtained for ASYN-P short in Milli-Q (black) and TRIS buffer (red) with the corresponding background fits (grey). Right: Form factors obtained for both datasets, showing no significant deviations. Data was modulation depth scaled.

EPR distance measurements carried out with aqueous samples at cryogenic temperatures require the addition of cryoprotectants to prevent crystal formation and retain a glassy state. This is typically conducted by adding 20 to 50 % glycerol (v/v) to the samples prior to freezing. In MD simulations this is not covered, imposing the need to assess the influence on the cryoprotectant on the structural ensemble. Three samples were prepared and subjected to DEER measurements, containing 20, 40 or 60 % (v/v) of deuterated glycerol (Figure 15). As seen on the left side of Figure 15, deviances in the form factor were observable. These are also reflected in the calculated distance distributions, shifting towards larger distances with increasing amount of glycerol (Figure 15, right).

[1] With Tikhonov regularization, calculation of distance constraints does not result in a single, unambiguous solution and can deviate for a single dataset depending on parameters such as the α parameter. Therefore it is not shown in cases were form factors do not significantly deviate and subsequently no change in distance distributions is expected.

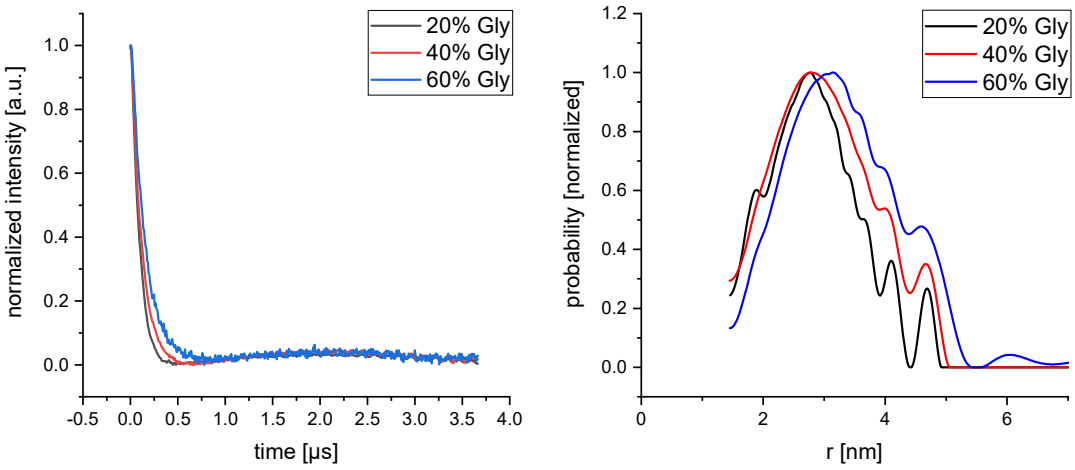

Figure 15: Left: Form factors obtained for ASYN-P short with varying amounts of glycerol. The data was normalized to facilitate the interpretation by eye. Right: resulting distance distributions (normalized) for the respective datasets, showing a shift towards larger distances with increased amount of glycerol. The full dataset is shown in Figure A. 3.

Upon increasing the glycerol content by a factor of three from 20 to 60 %, the resulting differences to the structural equilibrium appear minor. As glycerol is not included in MD simulations, subsequent measurements were carried out using a maximum of 20 % of glycerol to ensure an optimal compatibility of the experimental environment with the MD simulation parameters.

The presence of transient structural states in ASYN would imply a folding state equilibrium present in solution. If this equilibrium is still populated in the measured DEER samples, the impact of structuring is observable in the distance constraints. However, DEER measurements are conducted at cryogenic temperatures and involve fast freezing of the samples in liquid nitrogen. This procedure is rate limited by the rapidly evaporating nitrogen diminishing the temperature transfer rate between the sample, the glass vial it is stored in and the cryogenic liquid. The total time consumed for the samples to cool down to the glass temperature is thus at least in the hundreds of milliseconds.[164] To circumvent this, techniques to rapidly freeze EPR samples have been proposed and used.[164] A facile method to improve freezing times is the exchange of cryogenic solvent to isopentane that is not evaporating before 28 °C and thus increases heat transfer. To evaluate the resulting impact, distance measurements with both liquid nitrogen, as well as cold isopentane were conducted for ASYN-P short (see 8.1.1). As seen in Figure 16, the faster freezing rate with isopentane leads to a slight but significant broadening of the distance distributions. This is in line with previous results, suggesting that faster freezing traps more spin label rotamer states while retaining equal protein backbone conformations.[82]

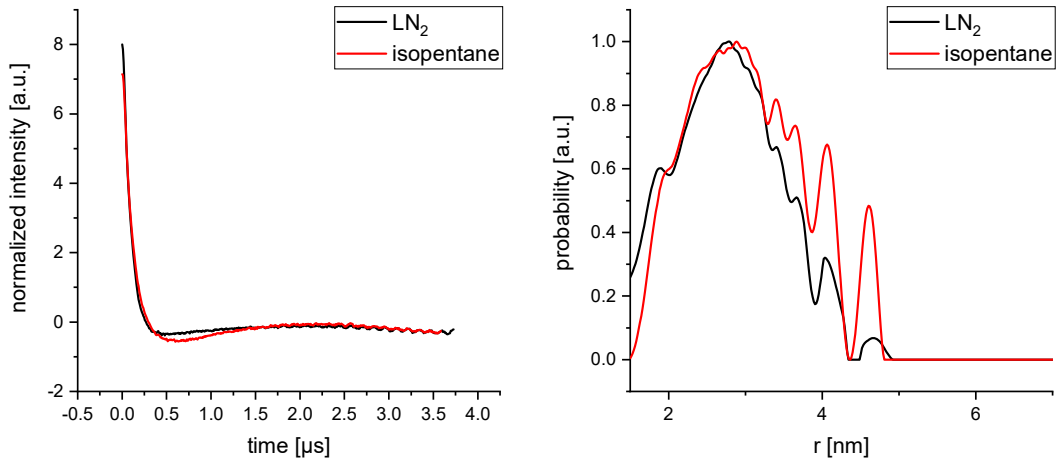

Figure 16: The effect of fast-freezing samples. Left: Form factors obtained for ASYN-P short in aqueous solution obtained after freezing with either liquid nitrogen (black) or cold isopentane (red) with the corresponding fits obtained from Tikhonov regularization. Right: resulting distance distributions, showing broadening of the distance distributions for the faster freezing procedure using isopentane. The raw data is shown in Figure A. 4.

Under the assumption of a non-affected protein or peptide backbone structuring, rapidly freezing the samples does not result in significant advantages in terms of label flexibility. Concerning transient backbone structures, it is crucial to compare the relevant time scales. While fast rapid-freeze quenching leads to freezing times of around 100 µs,[82] MD simulations carried out later in this chapter show refolding mechanisms on a time scale of pico- to nanoseconds. This implies that capturing preexisting structures from a peptide samples during the freezing process is certainly not possible with optimized procedures. It can be expected that the conformational equilibrium found in the DEER data represents the populations occupied around the glass temperature of the solvent. Given that no distinct structuring is found for ASYN and the derived peptides, the rapid refolding reactions implicate low energy barriers that are readily overcome with even low thermal energy. Equilibrium populations at the glass temperature are thus likely to represent roughly the same states found at ambient temperature.

After the thorough investigation and optimization of experimental parameters in order to precisely control those variables, the two longer peptides ASYN-P WT and ASYN-P DM that differ in the biologically relevant A30P mutation were structurally investigated in a combined approach using CD and EPR spectroscopy as well as MD simulations.

4.2.3. Structural investigation of the A30P disease mutation with a combination of experimental and simulation techniques

As mentioned above, disease mutations and their biological relevance are undoubtedly critical in understanding mechanisms of neurodegenerative diseases. Using the peptide model system developed in the scope of this work, deeper insights into the impact on the structural ensemble caused by the A30P mutation was strived for. The precision available using this fragment-based approach allows for a more detailed view into structural deviances.

Once more, CD spectroscopy was used to assess differences between the wild-type derived ASYN-P WT and the disease mutation based peptide ASYN-P DM. In addition to this, CD spectroscopy using the non-labeled derivatives was carried out , depicted in Figure 17. For all four samples shown, the CD signals strongly suggest an unordered state, which is in line with the measurements carried out in the beginning of this chapter using the peptides P3 and P4. This suggests that despite the attachment of TOAC spin labels, no significant aberration from the unordered state in aqueous solution is expected. A direct comparison of ASYN-P WT and ASYN-P DM shows no major disparities, hinting that the disease mutation does not induce a profound effect in aqueous solution.

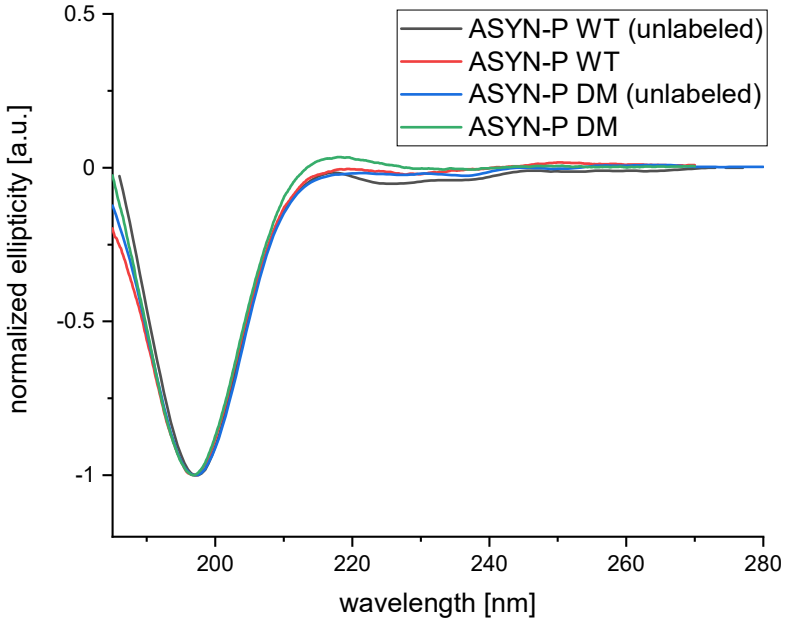

Figure 17: Normalized CD spectra acquired for ASYN-P WT and ASYN-P DM in either unlabeled form or with the attached TOAC label. No major deviances are observed for the four spectra, suggesting unordered states in each sample.

For a more precise view into structural details and differences between the wild-type and the disease mutant derived fragments, EPR distance measurements in aqueous

solution were conducted (Figure 18). The resulting distance distributions (Figure 18, bottom) do not impose major deviations between ASYN-P WT and ASYN-P DM. Both retain a broad distance dispersion suggesting high structural flexibility. The disease related mutation A30P thus seems to have no distinct influence on the conformational ensemble in aqueous solution, suggesting that potential differences in biological environments are not driven by large changes in the structural ensemble in the disease mutation containing peptide.

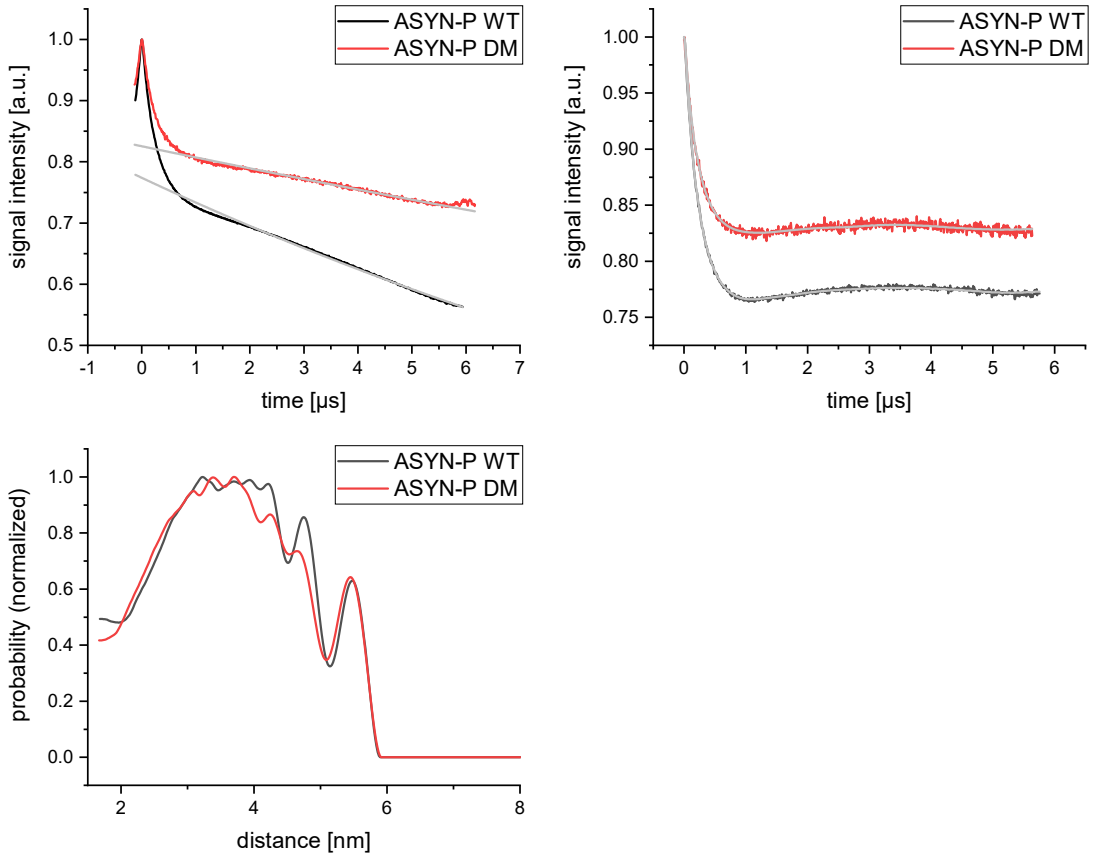

Figure 18: Distance determinations for ASYN-P WT and ASYN-P DM in aqueous solution. Top left: Raw data traces with the corresponding background fits (grey). Top right: resulting form factors and the fits (grey) from Tikhonov validation. Deviances in the modulation depth are caused by variations in pulse lengths. Bottom: Distance distributions (normalized) obtained with Tikhonov validation. For analysis details, see chapter 8.1.1.

In contrast to the broad equilibrium observed in aqueous solution, solvent exchange to methanol induces a major shift towards α-helical structuring that can be observed *via* CD spectroscopy for either the unlabeled peptides P3 and P4 (see Figure 8) or the labeled ASYN-P WT and ASYN-P DM (Figure 19). While both peptides feature spectral shapes suggesting a large fraction of α-helical structuring, significant deviations between the wild-type and the disease mutant derived are observable in the CD spectra. Though a quantitative comparison was omitted (see chapter 8.1.1 for details), a comparison of the spectral composition is still possible. For a full α-helical conformation, several key traits

in the spectra can be found. The global minimum at approximately 208 nm, an inflection point around 220 nm and the characteristic ratio of 2 to 1 between the global maximum and the global minimum. While the two spectra both fulfil the first two aspects, a 2 to 1 ratio is only found for ASYN-P WT with ASYN-P DM showing a less intense global maximum. This can be directly interpreted as a reduction in α-helical content for ASYN-P DM and is a clear sign for structural disparities between the two compounds. As the disease mutation replaces alanine with proline, the lower helical content can be traced back to the known helix-breaking properties of proline residues.[175]

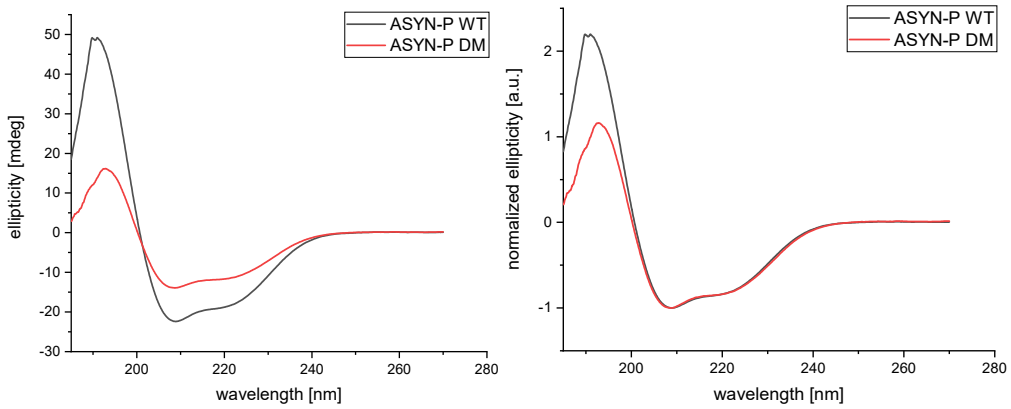

Figure 19: CD spectra of ASYN-P WT (black) and ASYN-P DM (red). Left: Spectra obtained for both samples. Right: Spectra normalized to the global minimum, facilitating the interpretation of apparent intensity loss in the global maximum for ASYN-P DM. This hints to a reduction of α-helical structure fractions for the disease mutation-based peptide.

EPR distance measurements were conducted with the spin labeled peptides in methanol (Figure 20). With the formation of α-helixes, the distance distributions obtained *via* DEER are significantly narrower than in aqueous solutions. This can be explained by the increased backbone rigidity upon secondary structure formations. For ASYN-P WT the distribution adopts an approximate unimodal shape that reflects low flexibility of the α-helix in conjunction unambiguous label orientations. While ASYN-P DM mostly overlap with the wild-type distance data for the long-distance contributions, in this peptide shorter distances are populated significantly more. This leads to a bimodal distribution with more emphasis on short distances that can be explained with the decreased helix content and thus more flexibility in the peptide backbone. The appearance of shorter distances upon helix breaking suggests that the adopted structure is not stretched but packed rather tightly.

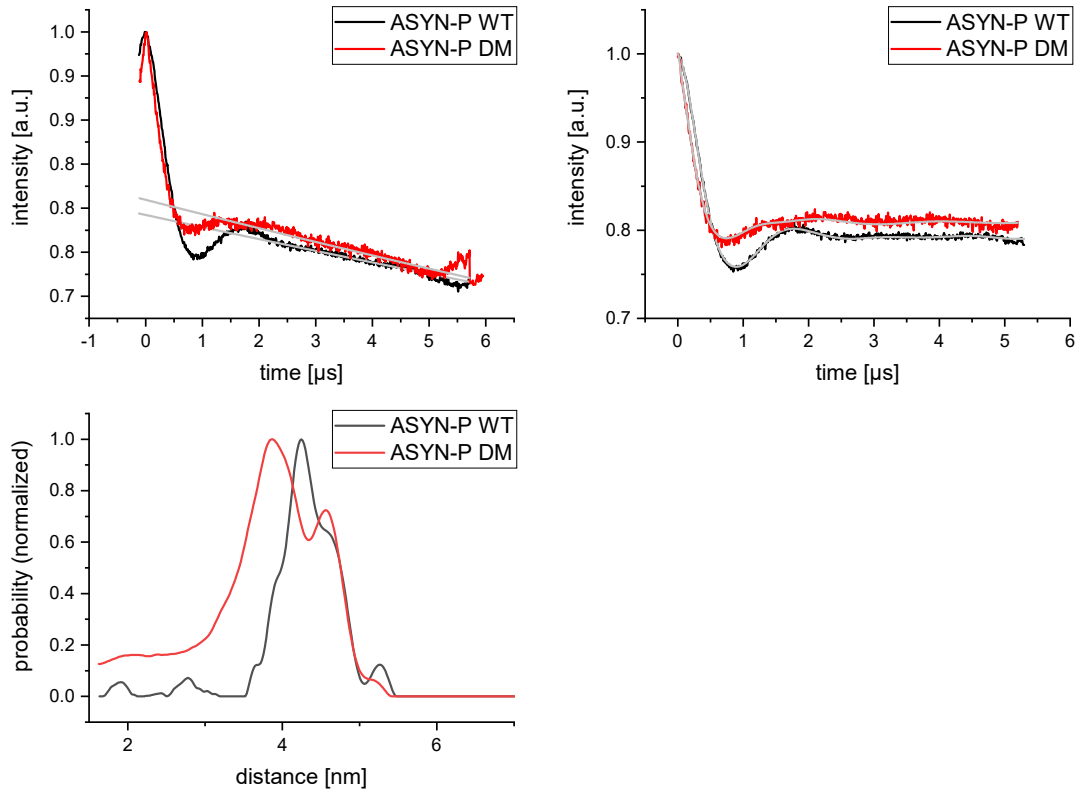

Figure 20: Distance determinations for ASYN-P WT and ASYN-P DM in deuterated methanol. Top left: Raw data traces with the corresponding background fits (grey). Top right: resulting form factors and the fits (grey) from Tikhonov validation. Bottom: Distance distributions (normalized) obtained with Tikhonov validation. For analysis details, see chapter 8.1.1

Experimental datasets have shown that while the A30P mutation does not significantly influence the structural ensemble in aqueous solution, the situation drastically changes upon formation of α-helical structures. In a biological context, this ordering can occur upon membrane binding, highlighting the necessity to understand the underlying structural rearrangements. CD spectroscopy and especially EPR are valuable tools to identify structural changes with increased insights rendered possible if a structural model is proposed using additional information. To assess this aspect, a combinatorial approach that uses experimental information to guide atomistic molecular dynamics simulations was developed in combination with Christoph Globisch, Jakob Steuer and Oleksandra Kukharenko (group of Christine Peter, Universität Konstanz).

While atomistic MD simulations have undergone large improvements in the last decades to accurately describe the structure and folding of proteins, the large structural fluctuations occurring in IDPs remain challenging. An important variable in these simulations is the choice of the force field. These are typically optimized using proteins with well-known three-dimensional structures as references, allowing the adjustment of force field parameters while ensuring the proper description of these model proteins. This can lead to a bias towards tightly folded and collapsed structures. However, IDPs

depict a drastically different structural landscape. Without long-term secondary structure elements, a tendency towards collapsed structures will lead to structure descriptions that lack any elongated substates. Utilizing the well-studied force field GROMOS that has been evaluated in a variety of simulation studies (see 8.1.1), the structure ensemble of ASYN-P short was determined in aqueous solution. For c_α-distances from the generated structures, end-to-end distance distributions were simulated (Figure 21). The majority of simulated structures led to distance distributions around 1 nm which is significantly shorter than the experimental results. This clearly shows the tendency for collapsed structures induced by this force field.

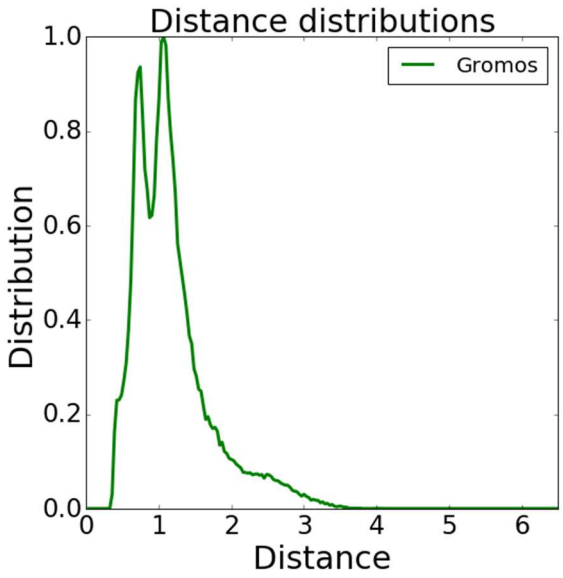

Figure 21: Normalized simulated distance distribution for ASYN-P short in water using the Gromos force field. For simulation details, see chapter 8.1.1.

MD simulations were thus optimized thoroughly in order to accurately describe the broad structural ensemble in the ASYN peptides. Notably, the simulation of IDPs is an emerging research area gaining track only recently.[176-179] With the help of these studies and thorough investigation of simulation parameters, the results were significantly improved. This was done for ASYN-P short, decreasing the computational effort during simulations due to the reduction of amino acid residues in comparison to ASYN-P WT and ASYN-P DM. With the guidance of experimental constraints obtained with EPR and CD spectroscopy, force fields were evaluated (see chapter 8.1.1). For samples reconstituted in methanol, the high secondary structure fraction adopted by ASYN-P short facilitated the simulations, leading to a high conformity between experimental distance distributions obtained from DEER and virtual distances calculated from the structural ensemble generated by MD simulations (Figure 22). By using the rigid TOAC spin label, the implicit label treatment was rendered possible and allowed for precise label positions with respect to the peptide backbone. With this, the obtained distance

distributions directly reports on the peptide structure. The simulated and experimental distance constraints both represent a structural ensemble dominated by α-helixes, which is in line with previous CD measurements. In contrast to CD data, the combination of EPR and MD simulations now allows for a fully atomistic view on the structural states adopted. With the precisely predictable spin label orientation, the MD simulations reveal a fully adopted helix that is stable throughout the simulation timescale (see Figure 22, right side). Here, the most prominent structures found in the simulation are bundled into a cluster that bundles states that highly resemble each other in terms of secondary structure parameters.

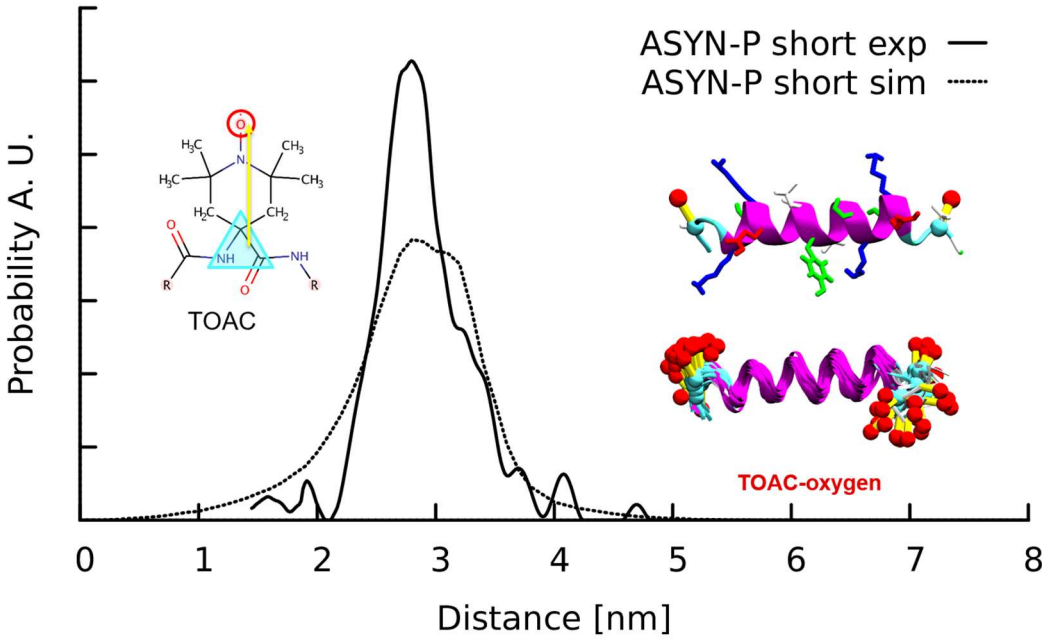

Figure 22: Distance distribution for the ASYN-P short fragment in methanol. Experimental DEER data for the TOAC-label (solid line) and the MD simulation data (dashed line). The position of the TOAC radical (indicated in red) is projected from a plane spanned by the backbone atoms of the labeled amino acid (highlighted in cyan) based on a distance obtained from electronic structure calculation of the TOAC molecule. The cluster on the right hand side highlight amino acid charges and hydrophilicity (blue - positive, red - negative, green - polar, white hydrophobic). The simulation data shows good agreement with the experiment and can be assigned to a mostly helical conformation of the peptide.

With ASYN-P short in methanol, both an accurate description of the experimental distance constraints as well as a deeper investigation into the underlying peptide structures is rendered possible using the combination of EPR and MD simulations. Using optimized force fields (see 8.1.1), DEER distance distributions obtained for ASYN-P short in aqueous solution were in good agreement with simulated datasets (Figure 23). Notably, the structural heterogeneity leading to the simulated distance distribution is significantly larger in aqueous solution. This is in line with results from CD measurements suggesting unordered states, leading to a diverse structural ensemble.

The conformations sampled in MD simulations cover a larger range of unordered and partially structured areas, depicted in the structure clusters shown in Figure 23. These clusters represent transient and thus short-lived secondary structure elements in the peptide. The distance regions represented by these MD simulation clusters are also populated in experimental constraints. However, a closer observation of the dataset revealed that even for a small distance region, the molecular structures leading generating said distances are highly heterogeneous. This implies that experimental distance distributions as obtained *via* DEER spectroscopy are not suitable to unambiguously pin point discrete molecular conformations. However, using additional information sources as shown with methanol, insights into the structural ensemble are possible.

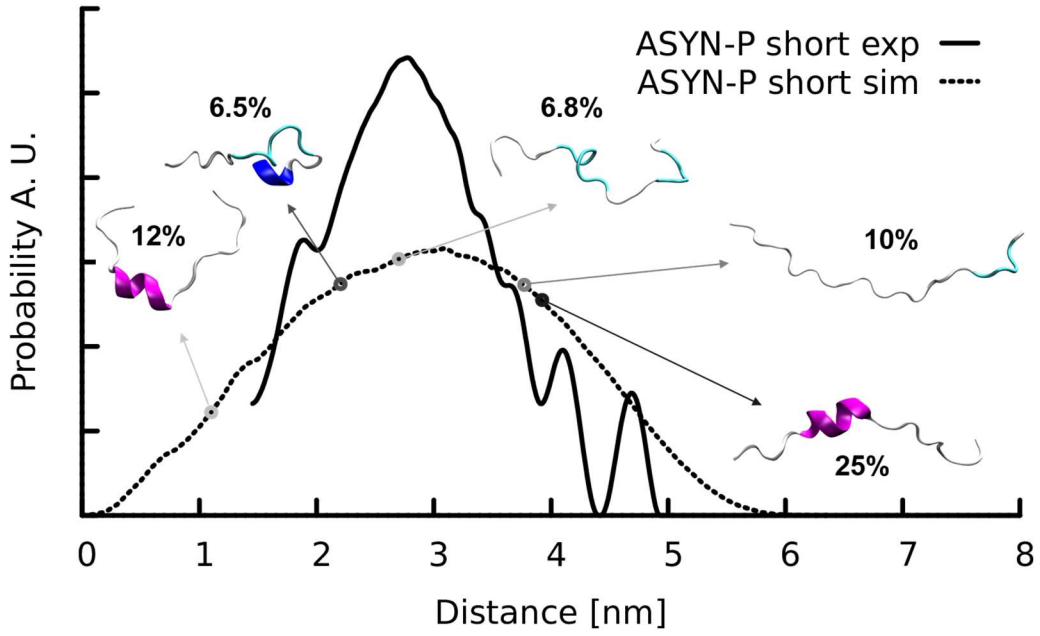

Figure 23: Distance distribution for the ASYN-P short in water. Representative structures are shown as central structures of the biggest clusters in cartoon representation. The corresponding DEER label distance is indicated as a circle on the distribution curve. The size of the cluster is given in percent. The range of simulated distances is in good agreement with the experimental data showing additional structures with smaller distances being below the experimental range. The wide distribution and the cluster centers are illustrating disordered character of the ASYN-P fragment in water showing only short transient secondary structure elements.

With the optimized using the shorter fragment, the disease mutation residue containing fragments ASYN-P WT and ASYN-P DM were used to conduct MD simulations. Primarily, this was carried out using methanol as a solvent. The resulting simulated distance distributions are compared to experimental restraints in Figure 24. For both the wild-type and the disease mutant containing peptide a high agreement between experimental distance constraints (solid lines) and simulated distance distributions derived from MD simulations was obtained. The significant changes as observed in DEER experiments are also reflected in MD simulations. Both techniques reveal a shift towards shorter distances as well as broadening of the distance range for ASYN-P DM in contrast to ASYN-P WT.

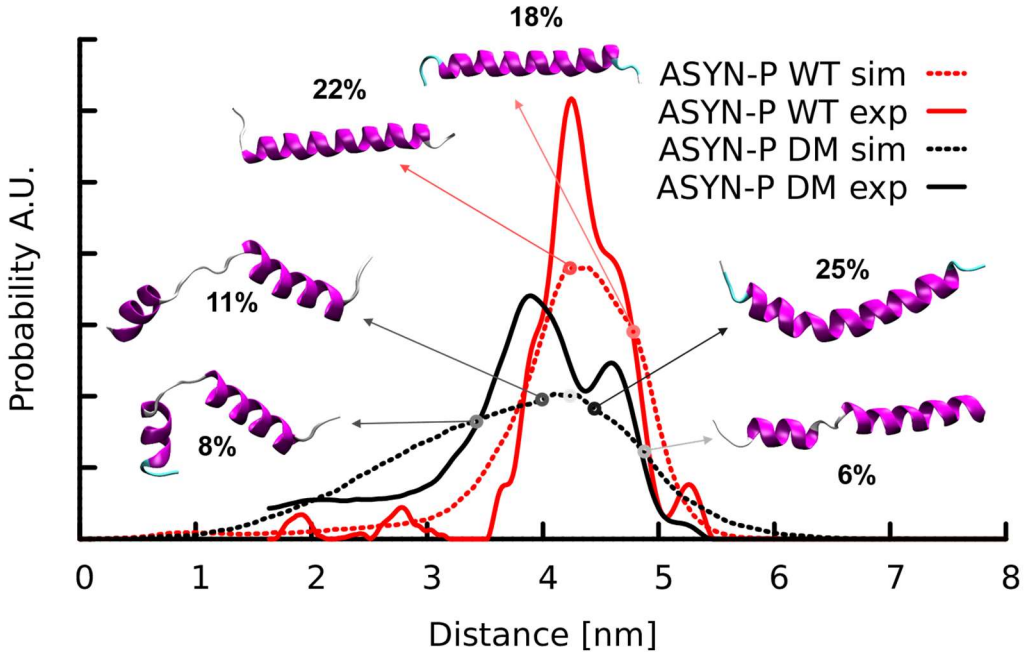

Figure 24: Distance distribution for the ASYN-P wild type (WT) fragment and the disease mutant (DM) in methanol. Representative structures are shown as central structures of the biggest clusters in cartoon representation. The corresponding DEER label distance is indicated as a circle on the distribution curve. The size of the cluster is given in percent. While the wild type ASYN-P fragment is maintaining the helical conformation with a rather narrow distance distribution, the disease mutant shows at least a kinked or broken helix initiated by the proline mutation with a wider distance distribution.

MD simulations calculate various structural models throughout the simulation time that can be clustered into characteristic states (structure models shown in Figure 24). The reduced helical content revealed by CD spectroscopy is also reflected in the clusters. For ASYN-P DM, breaking of the helix around the proline residue A30P is observed throughout the majority of the clusters that represent the highest contributions to the end-to-end distance distribution. While this behavior has been proposed for proline residues, the degree of unfolding around this residue can be followed precisely in MD simulations. Proline not only breaks the helix in the direct vicinity but also imposed larger propagation of unfolding in simulated cluster structures. This leads to a

pronounced shift towards shorter distances in contrast to the wild-type as bending of the helices decreases the label-to-label distance. This behavior is in contrast to the more stable helical state in ASYN-P WT which is reflected by cluster structures representing the maximum of the distance probability function. For ASYN-P WT, the helix is significantly more stable.

An aqueous environment led to significant broadening in the distance distributions for both ASYN-P WT and ASYN-P WT in conjunction with distinct changes in the CD spectra suggesting a conformational shift towards more flexible and unordered structures compared to the measurements in methanol. This absence of significant amount of secondary structure leads to large backbone fluctuations that are reflected in the broad DEER distance distributions. To assess the structural ensemble, especially regarding deviations between the two disease-mutation peptides, MD simulations were conducted (Figure 25). While the maximum of the simulated distance distributions is at lower distances than for experimental constraints in the aqueous case, the overall shape is sufficiently reflected and apparent differences reside mostly in the range below 2 nm. Distances lower than 2 nm are challenging to interpret using DEER spectroscopy due to exchange interactions.[87] In agreement with experimental data from DEER and CD, MD simulations lead to broad end-to-end distance reflecting the absence of significant secondary structure fractions. Representative clusters shown in Figure 25 depict the broad structural variety obtained in simulations. A direct comparison of ASYN-P WT and ASYN-P DM does not show significant differences induced by the point mutations, comparable distance distributions are in line with DEER datasets.

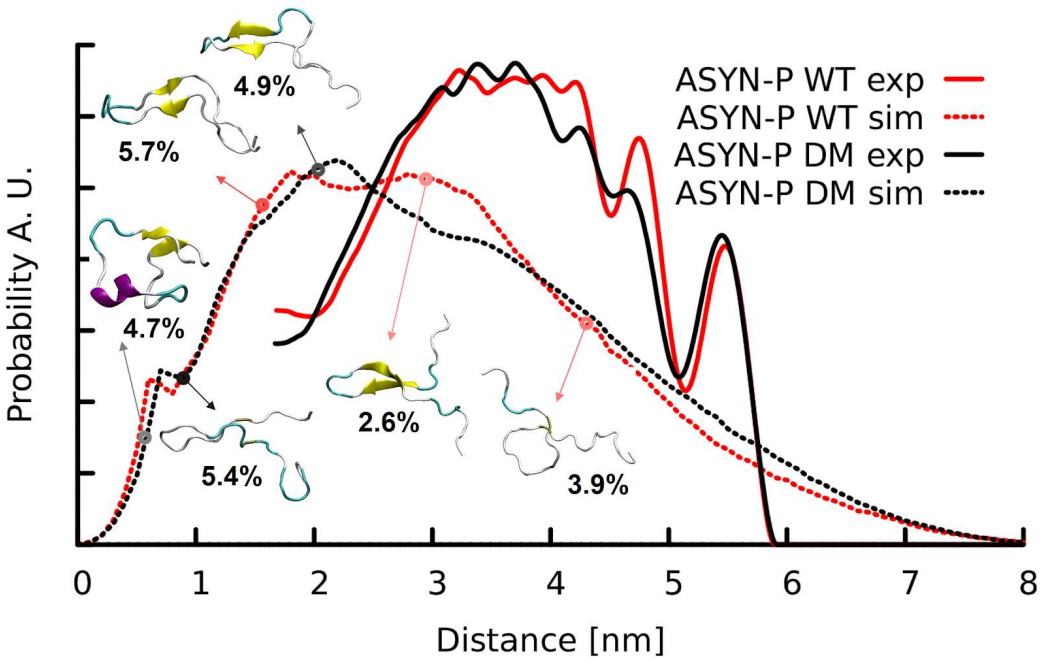

Figure 25: Distance distribution for the ASYN-P WT and DM in water. Representative structures are shown as central structures of the biggest clusters in cartoon representation. The corresponding label distance is indicated as a circle on the distribution curve. The relative size of the cluster is given in percent. The range of simulated distances is in good agreement with the experimental data showing additional structures with smaller distances being below the experimental range. The wide distribution and the cluster centers are illustrating disordered character of the ASYN-P fragment in water showing only short transient secondary structure elements. While both fragments show distinct fold differences in methanol, the water environment is levelling the differences from the DEER distance perspective but also from the simulation site.

To check the significance of certain areas of the distance distributions with respect to the differentiation of the underlying structural states, an area in the highest probability region of the distribution was chosen and searched for structures in the MD simulations reflecting this predicted end-to-end distance. In contrast to the rather homogeneous structure clusters obtained from this analysis in a methanol environment, the result is significantly more complex in aqueous solvent (Figure 26). The clusters representing specific areas in the distance constraints vastly differ in terms of the secondary structure elements they contain. In a small are of distances (see Figure 26), there are clusters found that include α-helical areas, β-sheet structures and unordered states. The heterogeneity of these clusters suggest that an end-to-end distance constraint, even with short peptides and rigid labels, leads to ambiguity in the structure composition.

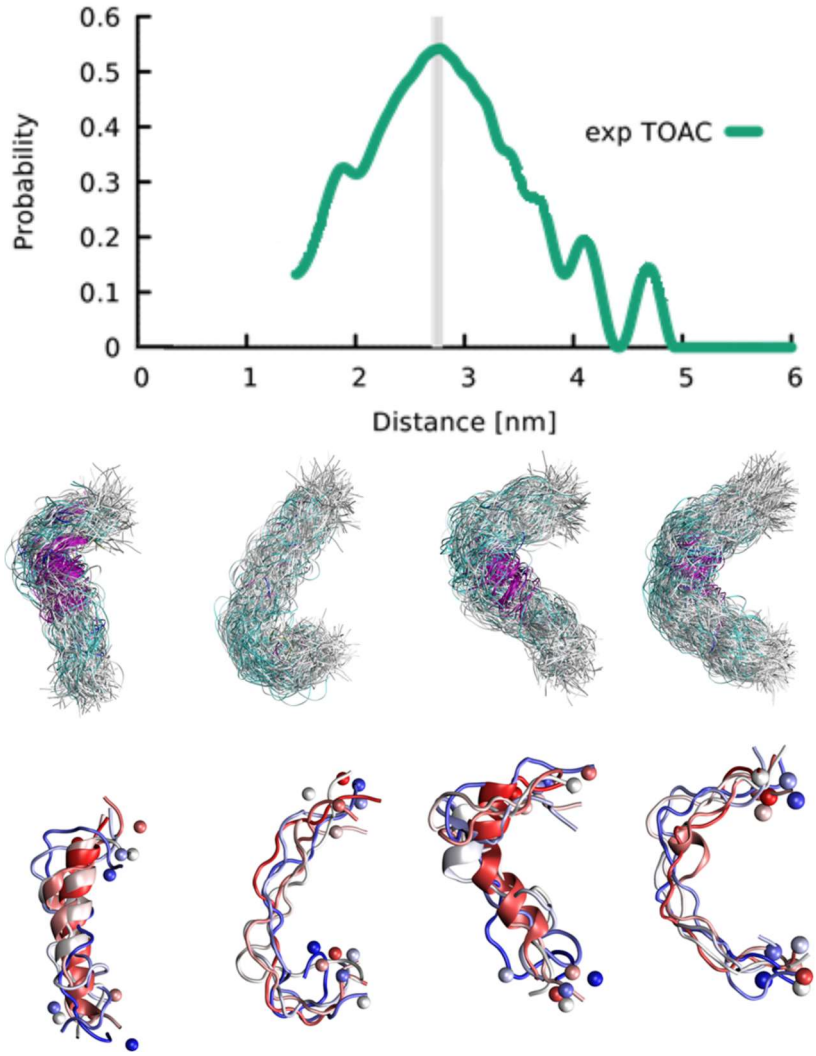

Figure 26: Distance distributions and simulated ensemble structures. Top: Experimental distance distribution obtained in aqueous solution for ASYN-P short. A small distance area in the maximum of the probability function was chosen (grey are). Middle: Four main ensemble clusters obtained from MD simulations that reflect the same end-to-end distance region. The high diversity between the four clusters is reflected in large deviations even in the secondary structure contents, as seen by the five discrete structures found in each of the clusters (bottom). Image adopted from Oleksandra Kukharenko, internal presentation.

The comparison of ASYN-P WT and ASYN-P DM in aqueous solution as well as in methanol showed the potential of a combined experimental and simulation approach. The interplay of MD with DEER and CD data adds structural details to pure experimental data, allowing for more insights into the effect of point mutations. In methanol, the peptides depict large structural differences as observed by all three techniques. Using MD simulated structure pools, helix breaking was found in variable degrees for ASYN-P DM. This lack in helical structuring as observed in methanol implies large deviations in the binding to *e.g.* membranes in cellular systems. This supports previous findings that found locally disrupted binding affinity to membranes for the A30P disease mutation.[148] These apparent structural differences might have an impact

on the interplay of ASYN with different cellular subsystems and further studies on hereditary Parkinson's disease could focus on these variations in structuring. In contrast to the situation on membranes, the two peptides did not exhibit significant structural changes in aqueous solutions. Earlier studies have shown that the fibrils formed by A30P mutated ASYN do not differ from ones formed by wild-type ASYN.[180] This could imply that the pathogenic impact of the A30P mutation is not based on misfolding characteristics but on the interaction with substrates such as biological membranes involving helical structuring of the protein.

In summary, a combinatorial approach including data from spectroscopic techniques and atomistic MD simulations was developed. Peptide fragments and a defined system were necessary to allow a direct comparison of experimental and simulation datasets. In the Peter group, MD simulations were performed on the basis of experimental constraints, ultimately leading to simulated end-to-end distance to be compared with DEER constraints. After evaluation of all parameters using the peptide ASYN-P short, the two peptides ASYN-P WT and ASYN-P DM were investigated. These two fragments contain the residue 30 that is a known location for the disease mutation A30P. Structural analysis in aqueous solution did not lead to detectable variations, suggesting that the A30P mutation does not induce a profound impact on the bulk protein in aqueous solution. In methanol, mimicking helix formation as seen in the presence of biological membranes, significant deviations were detected. Breaking of the helix in ASYN-P DM suggests a larger structural fluctuation for this peptide and can lead to variations in the interplay of mutated ASYN in the presence of biological binding partners, as suggested in earlier studies.[148] Here, not only the binding mechanism but the structural impact induced by the A30P mutation could be evaluated.

5. Dynamic and structural features of the activation loop in the kinase p38α

As shown in the last chapter, analysis of unordered structures is challenging due to the ambiguous ensemble of substates. In the following chapter, another approach to dissect disorder in a protein was developed. Here, an unordered region located in a rigidly ordered environment is analyzed. This rigid environment is depicted by the main part of the protein backbone in the kinase p38α that resides in stable secondary and tertiary structures and implicates anchoring points for the unordered moiety of interest - the unordered activation loop region. With the introduction of these fix points, analysis of structural changes impose a problem with reduced dimensionality and thus less ambiguity. Structural disorder and its implications to the biological function of p38α were analyzed.

5.1. The protein kinase p38α

Mitogen-activated protein kinases (MAPKs) play a crucial role in intracellular signaling pathways, particularly in cellular response systems triggered by stress signals.[181] Aberrations in these functions can lead to a variety of human disorders. Thus, there is great interest in dissecting and understanding the conformational plasticity of protein kinases and the effect of ligand molecules thereon.[182-184] The MAP kinase p38α has been shown to be linked to inflammatory diseases[185-186] and cancer[187] and its activity is regulated by structural changes in the activation loop region.[185] NMR data as well as free-energy calculations suggest a conformational equilibrium for the apo protein (*i.e.* for the isolated protein in absence of any substrates).[188-189] The modulation of the transitions between the two involved states (DFG-in and DFG-out, *i.e.* states of the Asp-Phe-Gly motif in the activation loop) using small molecules or by selective phosphorylation has been important for gaining a detailed understanding of kinase regulation and for the subsequent development of kinase inhibitors and drugs.[190-191] Kinase inhibitors can exhibit distinct mechanisms of inhibition and have thus been separated into types I to VI based on their binding mechanisms.[192-194] It is thus of utmost interest to understand and follow the impact of inhibitor binding to p38α. However, direct monitoring of the conformational equilibria of the activation loop within protein kinases remains challenging. Here, an approach to monitor the conformational equilibrium of a kinase of interest (*i.e.* p38α) was developed. This was achieved by a strategic spin labelling in the activation loop region and subsequent EPR mobility measurements.

5.2. Activation loop dynamics in a protein kinase

Accessing the conformational dynamics of the activation loop is rendered by a cwEPR approach, allowing the determination of label dynamics in liquid solution at physiological temperatures. The protein of interest, p38α, was strategically labelled with a spin label and subsequently monitored using EPR as schematically depicted in Figure 27.

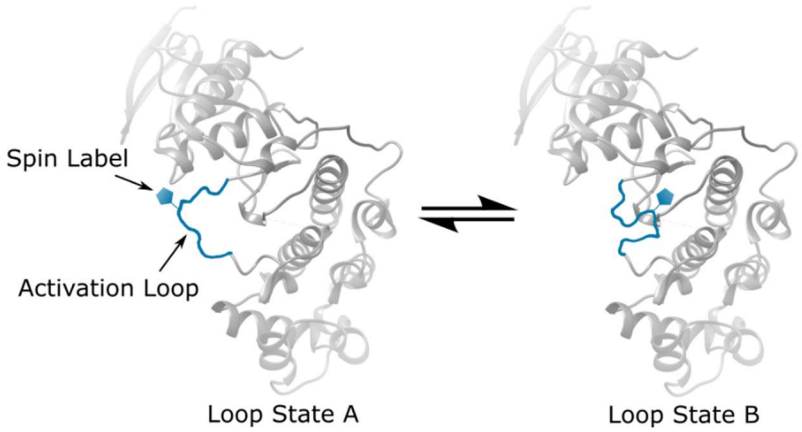

Figure 27: Schematic representation of the loop states and the spin label approach to observe structural dynamics.

Four point mutations were thus introduced into p38α: C119S, C162S and F327L and A172C, where the amino acid 172 is located roughly in the middle of the loop region. C119 and C162 are surface-exposed endogenous cysteine residues that had to be disabled to prevent multiple spin labeling reactions. While the replacement of phenylalanine with leucine at position 327 is not directly related to the spin labeling procedure, this mutation leads to increased activity of the kinase.[195] This mutant has also been used in previous studies using fluorescent probes and proved to be a viable and non-perturbing mutation.[196] Samples were prepared and purified by Jörn Weisner as described in chapter 8.1.2.

The protein stock solutions were labeled using thiol-specific spin label MTSSL ((1-oxyl-2,2,5,5-tetramethylpyrroline-3-methyl) methane- thiosulfonate, Figure 28). For details on the labeling and isolation procedure, see chapter 8.1.2.

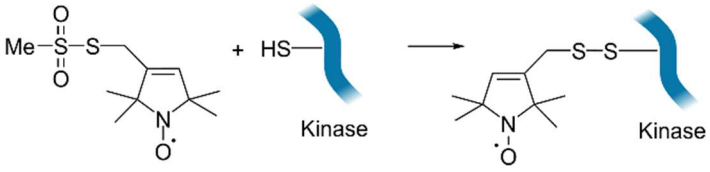

Figure 28: SDSL using MTSSL ((1-oxyl-2,2,5,5-tetramethylpyrroline-3-methyl)methane-thiosulfonate), which is attached to a cysteine residue.

A quantitative removal of the unreacted label in an aqueous environment turned out to be challenging. Even after ten washing steps, which should theoretically lead to a dilution of approximately one to one billion,[2] a small amount of spin label was detected in the recovered protein sample (see Figure 29). This was typically accounted to 0.1-5 % of free spin label with respect to the protein concentration. A possible explanation for the unfinished isolation step could be the nonpolar spin label being adhered to the nonpolar membrane of the spin filter and thus not being washed away completely. Its EPR signal was subtracted prior to spectra analysis. This was done using reference spectra from unreacted and separated spin label solution (see Figure 29). It should be noted that the MTSSL spin label result in a five-peak spectrum after labelling instead of the typically expected three-peak nitroxide spectrum. This is due to partial spin-label dimerization that occurs spontaneously in solution with a slow reaction rate when compared to the thiol-reaction with cysteine residues and does thus not disturb the labeling reaction. Labeling success was initially shown *via* EPR spectroscopy, revealing a slow-motion protein spectrum for all labeling reactions (see *e.g.* Figure 29). Quantitative spin counting, which allows for the determination of the sample spin concentration, revealed a good correlation between the expected protein and the spin label concentrations. As BCA assays and absorption measurements proved to be limited in their precision and resulted in significantly different concentrations, we chose to quantify the labeling efficiency using mass spectrometry.

[2] 100 µL is diluted to a volume of 1 mL in each step, leading to a ten-fold dilution and thus a dilution of 1 to 10^{10} after 10 steps.

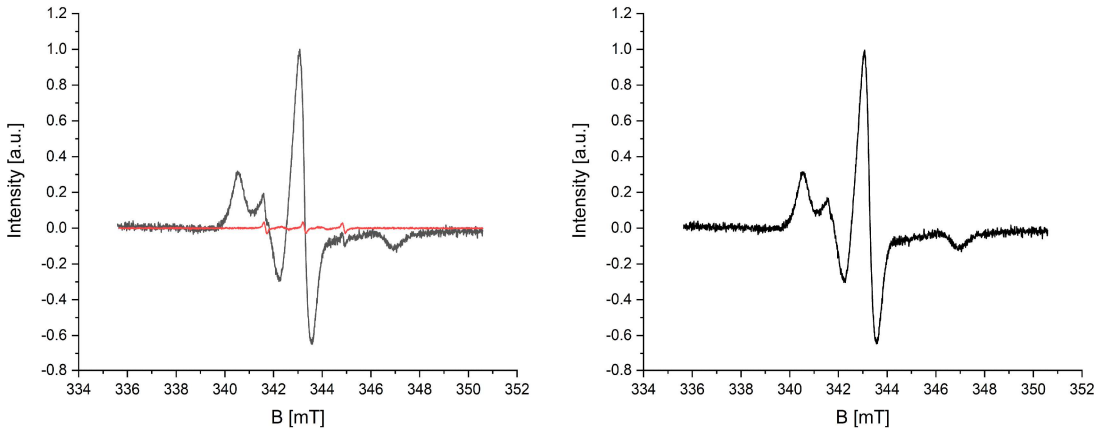

Figure 29: Exemplary process for the removal of free spin label signal. Left: Protein spectrum after labeling reaction (black) with small amounts (typically less than 1%) of unbound spin label still present and the scaled free spin label signal (red) to be subtracted. Scaling and shifting was done manually. Right: The resulting spectrum after the correction step.

Analysis of mass spectrometric data proved quantitative reaction to the desired product with no unreacted protein left in the sample (see Figure 30). This is in line with expectations for the highly reactive MTSSL and surface-accessible cysteine residues.

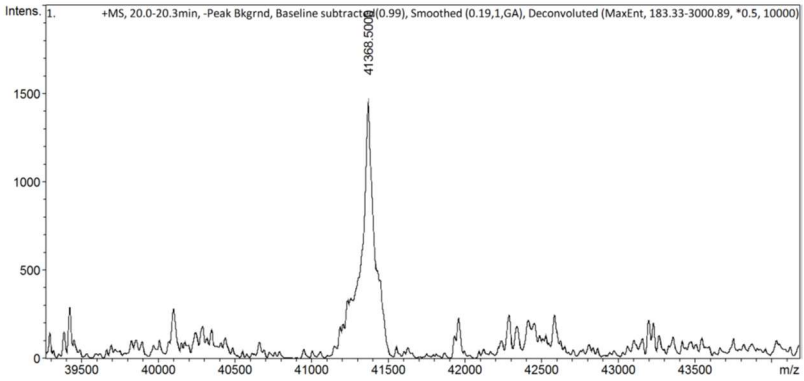

Figure 30: Mass spectrometry of labeled p38α, measured with Daniel Hammler in the group of Andreas Marx. The data shows quantitative single labeling (expected mass 41369 Da) with neglectable signal rising from unlabeled p38α (expected mass 41185 Da) or doubly labeled protein (expected mass 41553 Da).

To ensure that the introduction of point mutations and subsequent SDSL procedures did not disturb the protein's structure, enzyme kinetic characterizations were carried out by Jörn Weisner in the lab of Daniel Rauh, Dortmund. Shortly, these showed that the catalytic activity of spin labeled p38α is slightly reduced, yet still functioning (see chapter 8.1.2 for details). These results suggest that the proposed labeling approach is feasible and applicable in this scenario.

Free-energy calculations and NMR studies suggest an equilibrium between the DFG-out and DFG-in states.[188-189] The EPR spectrum for the apo protein was carefully analyzed with respect to multiple spectral species apparent. Spectral simulations were carried out using EasySpin[72], for details see chapter 8.1.2. Shortly, two distinct spectral components

were identified: Already in the raw data (see Figure 31, top), a splitting of peaks can be seen in the low-field part of the spectrum. This is an obvious trait of a system consisting of at least two components $S_{A,B}$ that differ in their dynamics or hyperfine splitting with a being the relative amount of component S_A.

$$S = a\,S_A + (1-a)S_B$$

Indeed, two components were sufficient to describe the experimental spectrum with good agreement: The main fraction consists of a slow component S_A that could be described using an anisotropic rotation while the smaller fraction of component S_B could be described with a significantly faster, isotropic rotation (see Figure 31, bottom).

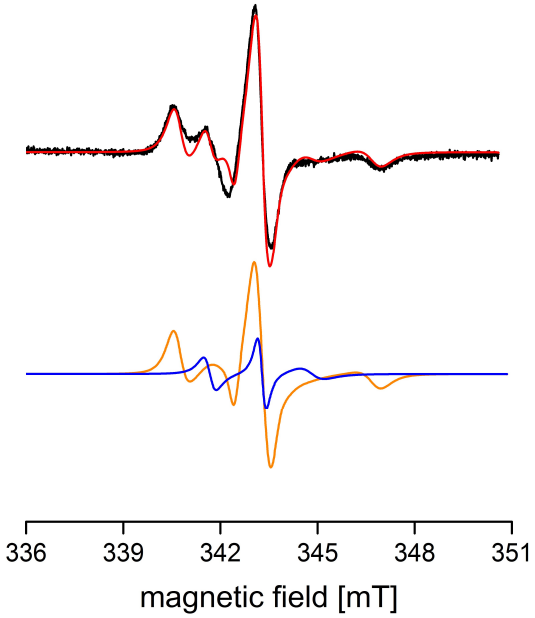

Figure 31: Top: Raw data (black) for spin labeled p38α and the corresponding spectral simulation (red). Bottom: The spectral components S_A (yellow) and S_B (blue) used to describe the spectrum in A.

Anisotropic rotation can be caused by a steric hindrance of the spin label, impeding a free rotation in all dimensions. To further substantiate this steric constraint, a PyMOL simulation of the spin label rotamers attached to the loop was carried out, showing a clear asymmetry in the possible spin label rotamers caused by clashing with amino acid side groups (see Figure 32). The spectral simulations then resulted in a ratio S_A/S_B between the two components of about 9:1. These two species hint at an equilibrium between different states of the activation loop dynamics and could be linked to the extensively discussed DFG-in and DFG-out states.[12, 197] Yet, further studies were needed to evaluate this indirect link from spin states to the activation loop structure.

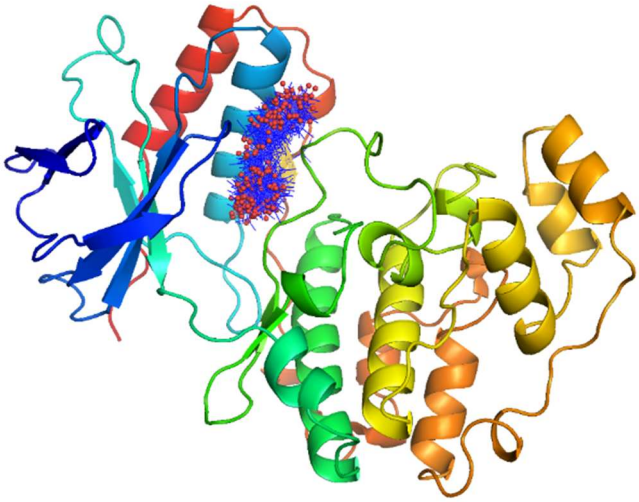

Figure 32: Using The PyMOL Molecular Graphics System (Version 1.8 Schrödinger, LLC.) and the plugin MTSSL Wizard[198] (Speed: Thorough, vdW restraints: tight) rotamers for the spin label were simulated.

The fast spectral simulations shown resulted in good agreement with the experimental data. For a more accurate description of the experimental data, an improved and vastly more complex spectral simulation system was developed. For this, an orienting potential was introduced.[199] This describes a potential energy leading to a ordering of the nitroxide to a director axis as it is often the case for (bio-)polymer bound spin labels. This *M*icroscopic *O*rdering while maintaining *M*acroscopic *D*isorder (*MOMD)*[199] model introduced in EasySpin simulations with ordering potential coefficients $\lambda_{2,0}, \lambda_{2,2}, \lambda_{4,0}, \lambda_{4,2}, \lambda_{4,4}$. The indicated approach resulted in a significantly improved agreement between the simulations and experimental data as shown in Figure 33. The drawback is the vastly increased computational effort needed for these calculations. In order to verify the rigidity and reliability of both approaches, the resulting equilibria constants were compared, showing similar results with respect to the ratio between the two spin components (Figure 33).

The data shown for the apo p38α thus hints to an equilibrium of two substates which is present even without the addition of small molecule inhibitors and has not been shown experimentally shown to this point.

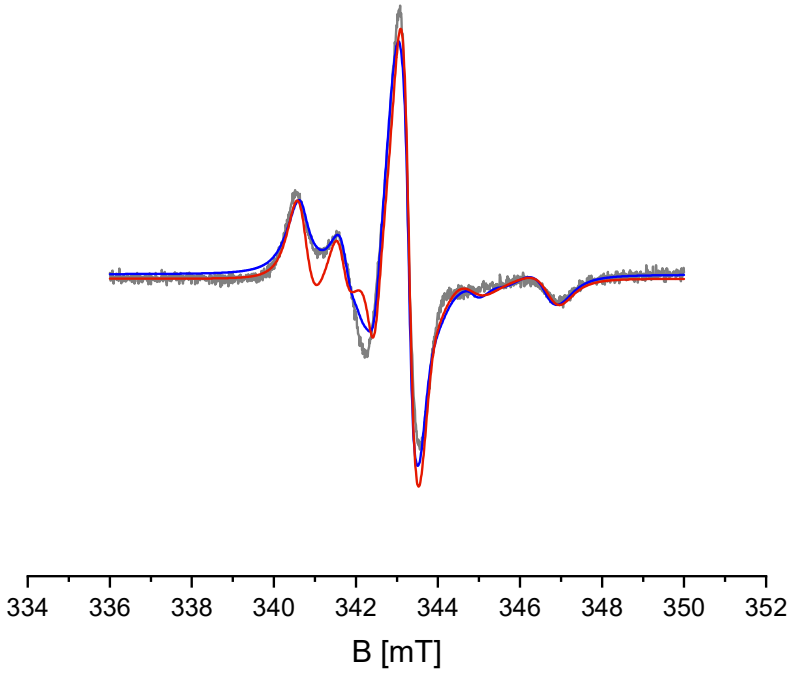

Figure 33: Comparison of experimental data for p38α (grey), spectral simulations using an anisotropic rotation for S_A (red) and simulations with an orienting potential applied (blue).

Assuming that the spin components $S_{A,B}$ reflect the DFG-in and DFG-out states of the activation loop, this should be an equilibrium prone to be shifted towards one or other side using environmental influences. These can be changes in the temperature, solvent or pH. In addition, small molecule inhibitors are known to interact with the loop equilibrium. These inhibitors are separated in several categories. Here, type I and type II inhibitors were chosen. While type I inhibitors are expected to impose only minor effects on the activation loop, type II inhibitors should favor the DFG-out conformation.[197] Thus, a total of eight different inhibitors belonging to either the type I or II were chosen for further studies on their impact on the loop dynamics. For this, p38α at a concentration of 50-100 µM was mixed with varying amounts of the inhibitors RL45, RL48, Sorafenib, Regorafenib, Skepinone-L, SKF-86002, SB203580 and BIRB-796 (10 mM in DMSO stock solutions) to yield a final molar ratio of p38α:inhibitor of 1:3, 1:6 or 1:12.[200-205] The mixture was incubated for 90 min at 21 °C while gently shaking the flask. The final amount of DMSO in the samples did not exceed 5% in any measurement to prevent unfolding of the protein. As all of the inhibitors show nanomolar activities and the EPR measurements were conducted at micromolar concentrations (see 8.1.2), full saturation of the kinase with inhibitors can be expected. To evaluate this, the amount of inhibitor was varied and the resulting EPR spectra were analyzed. While for seven inhibitors no change was observed, BIRB-796 showed a significant dependence to the amount of inhibitor added (see Figure A. 5 to Figure A. 11). This hints towards binding of several molecules to one protein. Unfortunately, this could not be proven using isothermal calorimetry titration (ITC) experiments.[206] Thus, BIRB-796 was excluded from

further studies and following experiments were conducted using the seven remaining inhibitors (Figure 34).

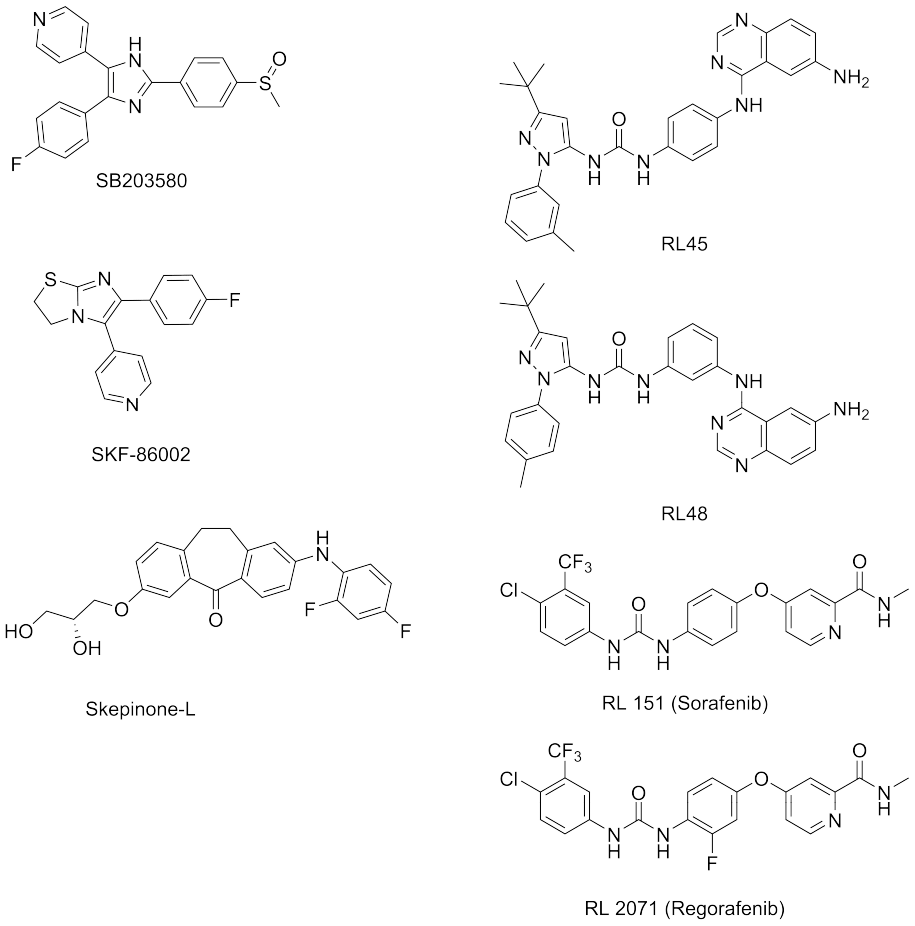

Figure 34: Structure formulas of the seven small molecule inhibitors used. Three type I inhibitors (left) and four type II inhibitors (right) were chosen.

The remaining inhibitors are differentiated between type I (Skepinone-L, SKF-86002, SB203580) and type II (RL45, RL48, Sorafenib, Regorafenib) based on their binding characteristics as discussed in chapter 5.1. All of these showed a significant impact on the EPR spectrum when compared to the apo p38α that can be observed even in the raw data (Figure 35). Remarkably, the three type I inhibitors and the four type II inhibitors result in spectra that clearly separate the inhibition types while being virtually identical within the groups. Typically, the inhibitor types are discriminated using X-ray crystallographic studies. This EPR approach imposes a quick and elegant way to differentiate between inhibition types.

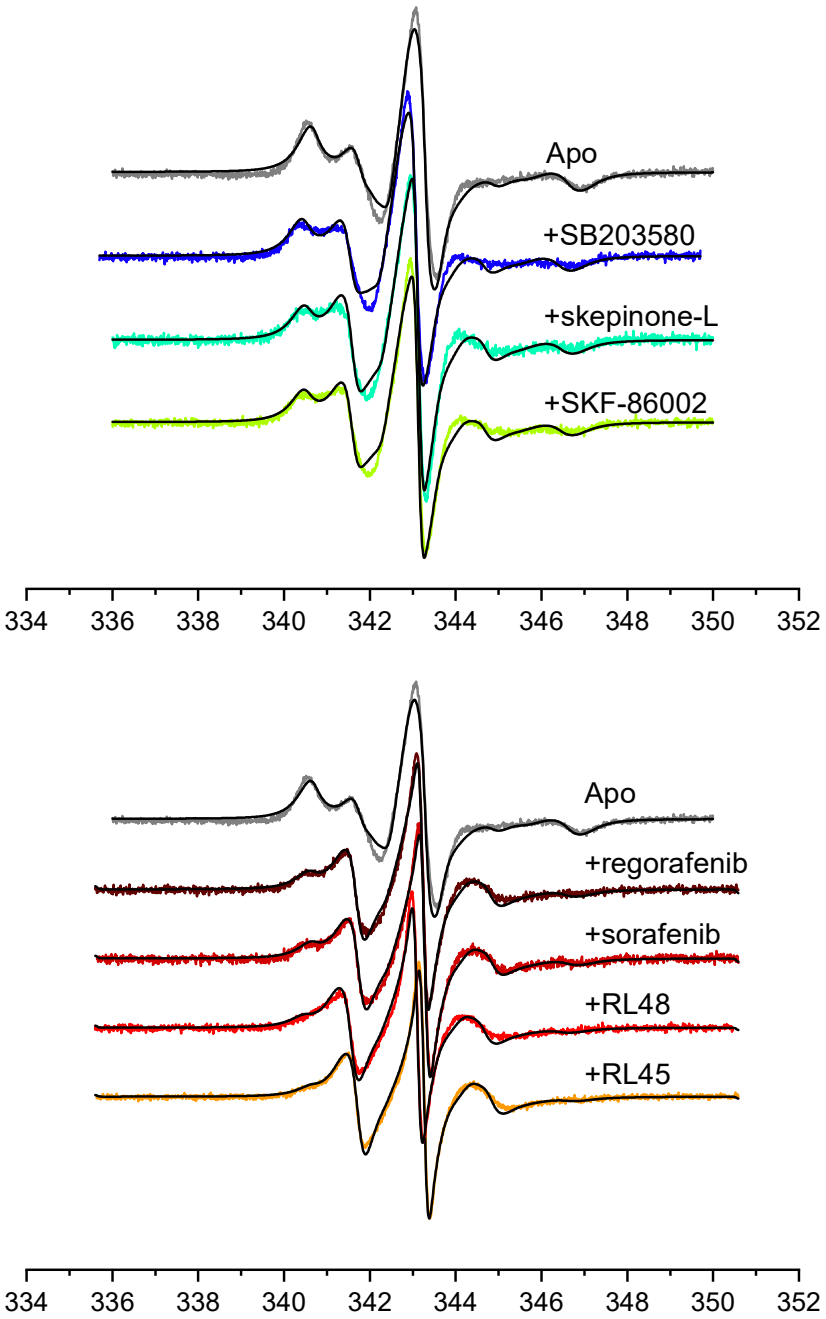

Figure 35: X-Band EPR spectra for apo p38α (grey) and upon addition of: type I inhibitors (skepinone-L, SKF-86002, SB203580, top) and type II inhibitors (RL45, RL48, sorafenib, regorafenib, bottom) at T=293 K.

In addition to this, spectral simulations of the spectra allow for a full quantification of the underlying equilibria. The fraction of the slower rotating component S_A can be expressed by the factor a. For the apo p38α, a was found to be 0.9±0.025, *i.e.* that the relative population of the S_A state is 90%. This state is assumed to be the DFG-in state of the activation loop based on the inhibitor effects shown in the following. As it is known for type II inhibitors to favor the DFG-out conformation of the loop region, a shift of the equilibrium towards S_B in the type II inhibition assay would be expected. Indeed, while a shift towards S_B is detectable for type I as well as type II inhibitors, this shift is

remarkably more pronounced in the latter case. While type I inhibitors lead to a ratio of around 70/30 for S_A /S_B, type II inhibitors lead to roughly a 50/50 equilibrium (Figure 36). Thereby, the hypothesis of $S_{A,B}$ reflecting the DFG-in and DFG-out states is encouraged. It can also be deducted from this data that the compounds act in a mechanistically different matter that differs in the impact on the activation loop dynamics.

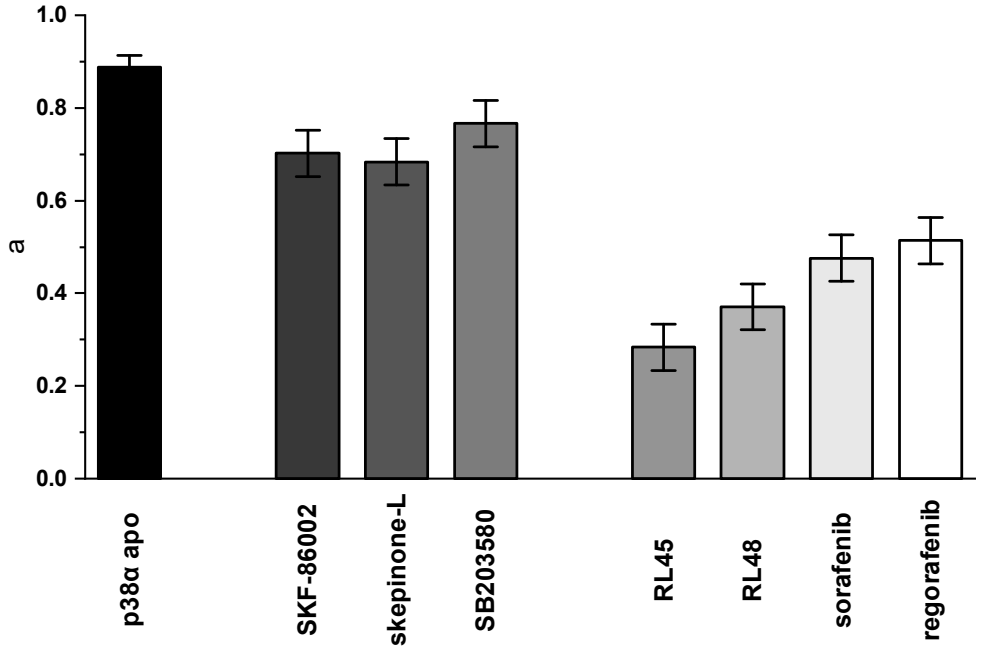

Figure 36: Spectral fraction *a* of p38α upon addition of seven different inhibitors at 293 K. The relative amount a of the spectral component S_A (allocated to DFG-in state) is shown. The inhibitors are grouped in type I inhibitors (middle section) and type II inhibitors (right). The estimation of the error is explained in chapter 8.1.2.

The equilibrium of the activation loop states was studied in a temperature-dependent experiment. For this, EPR spectra for p38α apo and in combination with all of the above inhibitors were collected in a temperature range from 278.15 to 305.65 K / 5 to 32.5 °C (Figure A. 12 to Figure A. 19). Lower temperatures were not feasible due to freezing of the aqueous solvent. Assuming a two-state equilibrium reaction, change of temperature should lead to a shift in the relative fractions of the states depending on the enthalpy and entropy changes occurring during the reaction. In this case, the refolding process of the activation loop is observed. For this, the full series of temperature series for apo p38α and with all the inhibitors were collected and analyzed using spectral simulations. As stated above, orienting potentials introduce a major computational effort to the spectral simulations and is thus not feasible for the amount of spectra collected. Therefore, a more efficient simulation approach was chosen that omits the need for orienting potentials (Figure 37). To make sure these simulations are in line with the results achieved using orienting potentials, the resulting equilibria were compared, showing comparable numbers in all cases (Table 1).

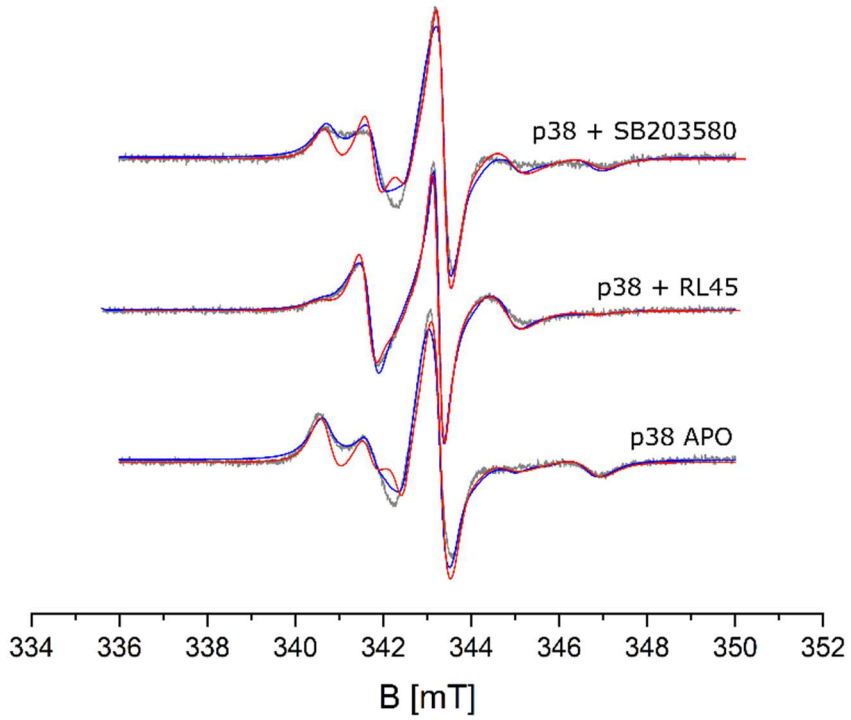

Figure 37: Exemplary comparison of the experimental results (grey) with the corresponding spectral simulations obtained with (blue) and without (red) the assumption of an orienting potential for the apo p38α and after the addition of RL45 / SB203580.

Table 1: Comparison of the spectral simulations with and without the use of an orienting potential and the resulting weighting parameter *a*.

	a	
	With orienting potential	Without orienting potential
p38α apo	0.89 ± 0.025	0.88 ± 0.025
+SKF-86002	0.70 ± 0.05	0.69 ± 0.05
+skepinone-L	0.68 ± 0.05	0.67 ± 0.05
+SB203580	0.76 ± 0.05	0.69 ± 0.05
+RL45	0.28 ± 0.05	0.38 ± 0.05
+RL48	0.37 ± 0.05	0.39 ± 0.05
+sorafenib	0.47 ± 0.05	0.48 ± 0.05
+regorafenib	0.51 ± 0.05	0.52 ± 0.05

The equilibrium ratios obtained from the spectral simulations were used to calculate the reaction constant K (K in this case describes the fraction of $\frac{Folding\ state_2}{Folding\ state_1}$) for the two-state transition and collected in a Van't Hoff plot of ln(K) over 1/T (see Figure 38 A for an exemplary dataset, Figure A. 12 to Figure A. 19 for the full dataset). The slope of the regression line reflects -ΔH/R (with R being the gas constant) while the intercept is given by ΔS/R. Using error propagation starting from the initially approximated error for *a* and a weighted linear fit, the resulting error in ΔH and ΔS was calculated. Temperature-dependent analysis of the equilibrium constant K as shown in Figure 38B again highlights spectral separation of spectral components for apo p38α and the type I and type II inhibitors.

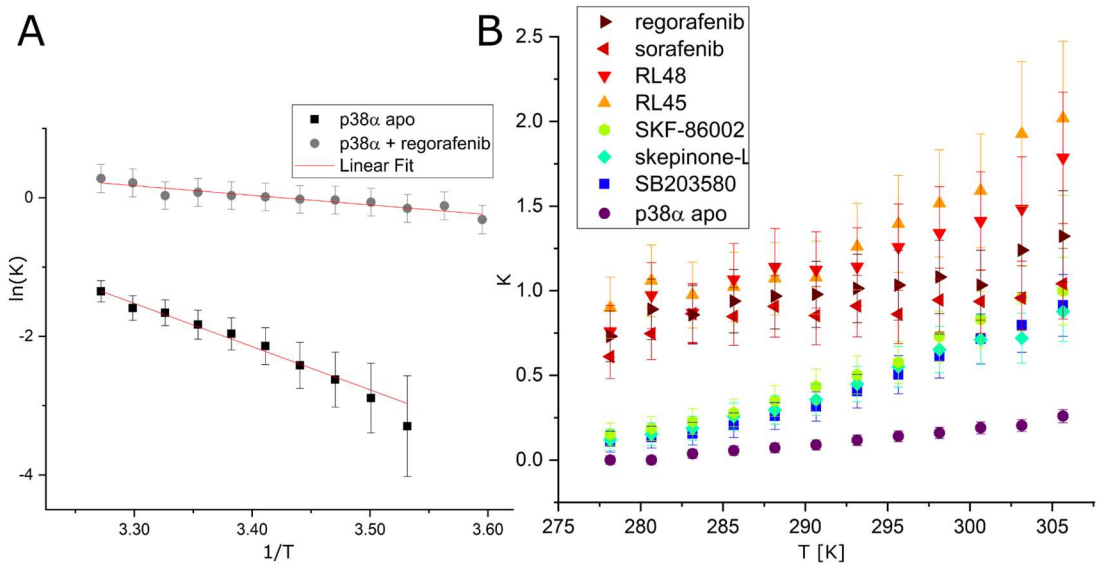

Figure 38: Temperature dependent EPR analysis. A: Van't Hoff plots for p38α with and without regorafenib and the corresponding linear fits used for the calculation of thermodynamic parameters. B: Temperature-dependency of the reaction constant K for all assays showing the equilibria in the two-state system. For the full data set, see appendix.

For a two-state equilibrium reaction, a linear behavior for ln(K) over 1/T is expected. This was the case for all spectra analyzed here, supporting the assumption taken. The Van 't Hoff analysis allowed the determination of ΔH and ΔS for the DFG-in to DFG-out transition (Figure 39). Free energy calculations for the apo protein predicted ΔH≈-TΔS≈15.44 kJ/mol.[189] The values obtained for apo p38α are larger but still in the same order of magnitude (52 kJ/mol). Interestingly, the enthalpy parameters for the type I inhibitors do not significantly differ from those obtained for the apo protein. The same is the case for ΔS, which is not significantly changing between the apo protein and the samples with type I inhibitors. This contradictory result to the room temperature measurements discussed above can be explained by the insufficient data availability. For this analysis, a larger accessible temperature range, especially towards higher temperatures, would give access to more precise analysis of the thermodynamic parameters. Unfortunately, this is not possible due to thermal unfolding of the protein at higher temperatures. The observed differences in the room temperature measurements between apo and type I inhibitor samples are thus non-significant for the given noise level. In contrast to this, type II inhibitors show significantly reduced enthalpy and entropic contribution, indicating a pronounced shift towards the DFG-out conformation. Here, an increased preference for the DFG-out state is observed, in line with the expectations for type II inhibitors.[12]

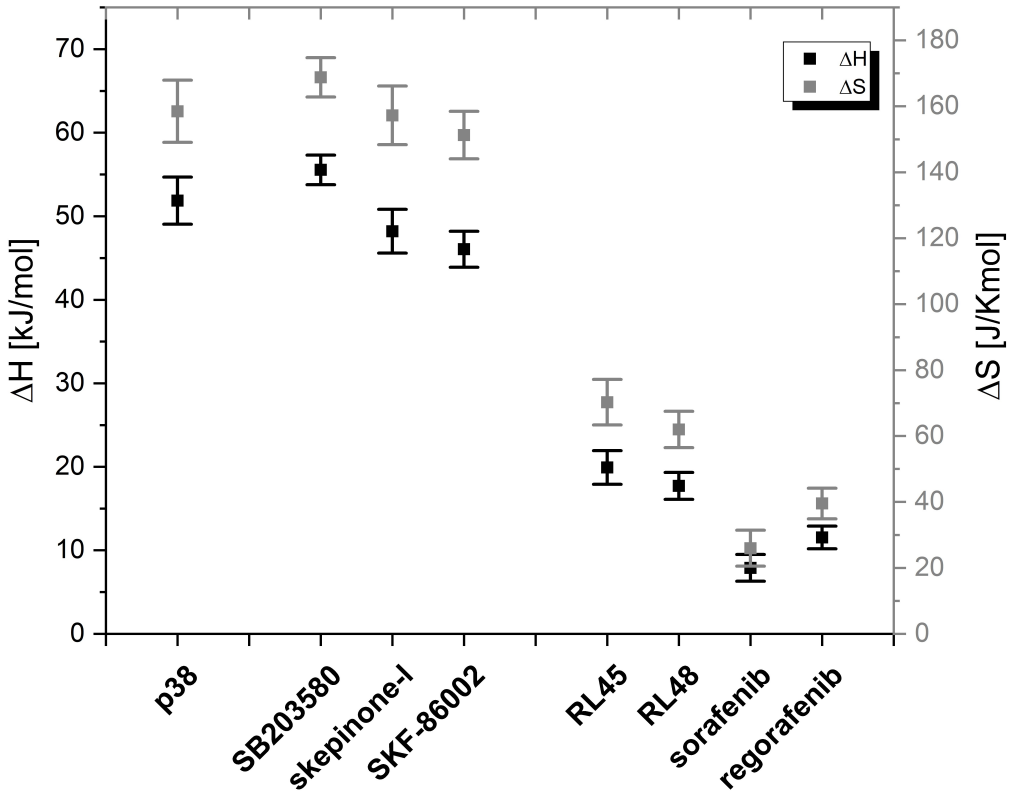

Figure 39: Thermodynamic parameters for the conformational equilibrium as obtained from temperature dependent EPR measurements with and without addition of inhibitors showing a clear separation of type I and type II inhibitors.

The measurements in presence of inhibitors have shown a shift of the loop equilibrium towards the S_B or DFG-out state, the extent of this shift was dependent on the type of inhibitors used. In contrast to the inhibition and thus deactivation of the kinase, binding of adenosine triphosphate (ATP) or its derivatives potentially lead to increased activity.[207] Binding can occur not only with ATP, but also with adenosine monophosphate (AMP) and adenosine diphosphate (ADP, see Figure 40). This reaction is usually catalyzed by magnesium ions.[208] Binding to the protein and activation could potentially affect the activation loop structure and/or dynamics and is thus an alluring subject for further studies. The binding experiments were carried out in analogy to the inhibitor assay: To the labeled p38α various amounts of ATP and its derivatives were added, either without or with the addition of $MgCl_2$ (to a final concentration twice as much than for the ATP derivative). Interestingly, none of the combinations above lead to a significant effect in the EPR spectra (Figure 41). There are several explanations for the absence of observable effects, these will be discussed in the following.

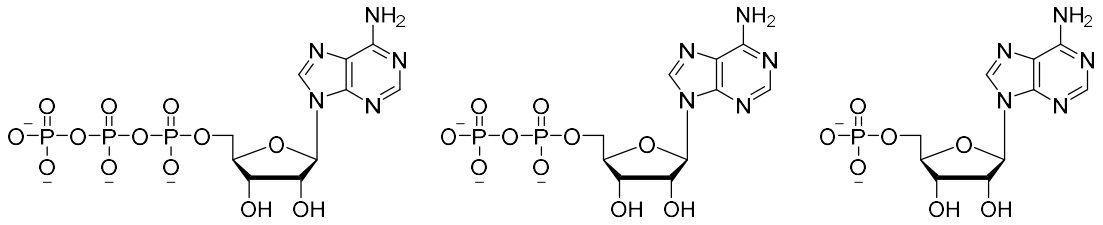

Figure 40: Structure formulas of ATP (left), ADP (middle) and AMP (right).

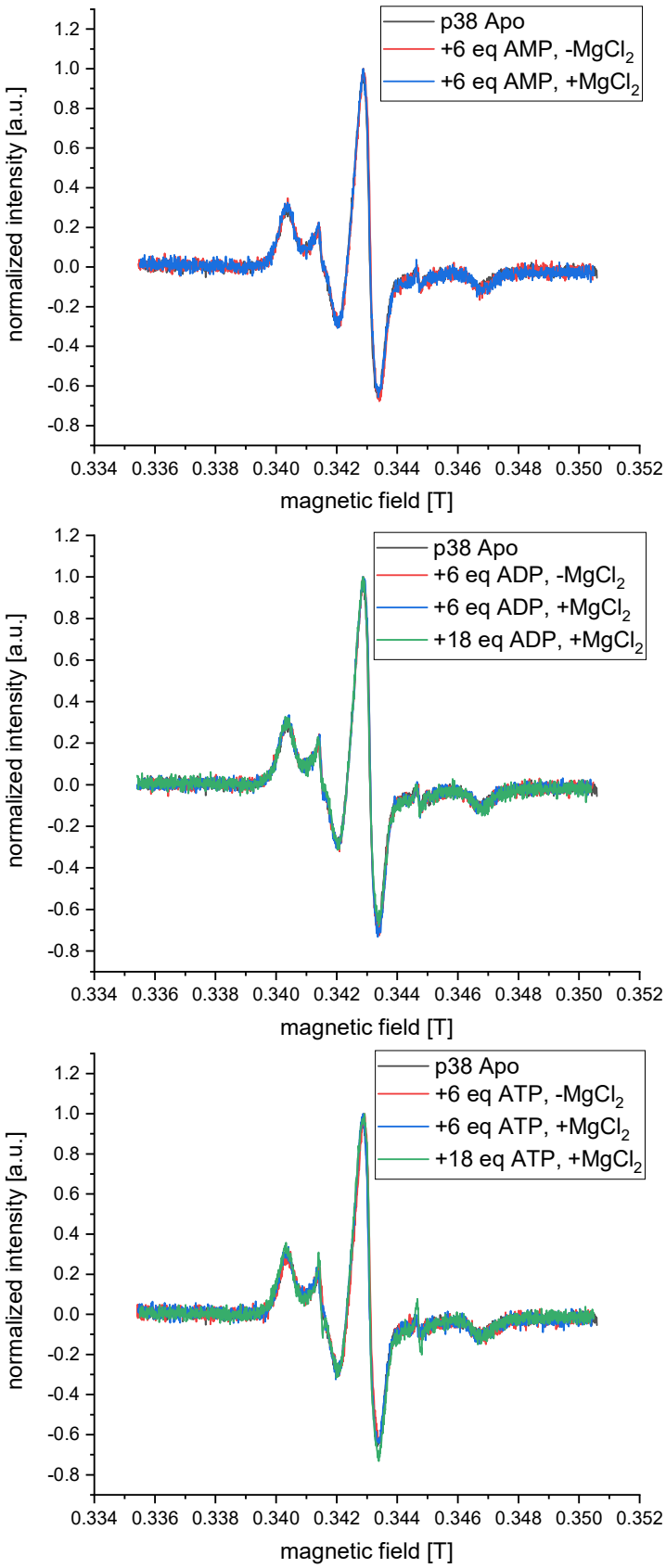

Figure 41: EPR spectra of p38α with varying amounts of AMP (top), ADP (middle) or ATP (bottom). Spectra have been recorded either in the presence of $MgCl_2$ ("+$MgCL_2$") or without ("-$MgCl_2$"). No significant changes are observable.

First, it might be possible that the binding of ATP does not induce an impact on the activation loop at all. This is unlikely, as the binding of ATP to p38α is well-studied and thus should also influence the activation loop. While binding affinity is indeed affected by factors such as phosphorylation and the p38α used here are non-phosphorylated, the impact of phosphorylation on binding affinities has proven to be minor and the concentrations used are expected to induce a significant effect.[209-210] This is supported by studies on the Aurora-A kinase, which shares many common traits with p38α and where inhibitor binding is not dependent on the phosphorylation state of the kinase.[211]

Another explanation is that there is indeed an effect of ATP to the loop, yet this effect is not influencing the loop dynamics in a sufficient degree to be detectable in this approach. This could then be a very small effect or only affecting the structure without influencing the loop dynamics significantly. Again, this hypothesis seems to be rather unlikely as a minuscule influence will not change the kinase activity itself and a structural impact will change the dynamics in virtually all cases.

Another explanation of undetectable changes is the simple absence of changes. If ATP (or its derivatives) are not bound to p38α, no change in the dynamics is expected. This again could have several reasons. ATP is prone to hydrolysis in aqueous solutions and could thus be modified in the timescale of the experiment. To check this, the incubation time prior to the EPR measurement was reduced gradually from 90 minutes to 10 minutes. This led to no detectable changes in the spectrum (data not shown). Another possibility to circumvent hydrolysis is the usage of non-hydrolysable ATP analogues. This approach will be discussed further in chapter 5.3.2.

To conclude, this study using several inhibitors found that p38α in its apo-form is existing in a coexistence of DFG-in and DFG-out in an equilibrium. Crystal structures obtained in the presence of type II inhibitors show exclusively the DFG-out state.[12] In contrast, in solution rather than in the crystal state, a significant fraction of p38α featuring a DFG-in like state in the presence of a saturating excess of type II inhibitors was observed here. This might also suggest that type II inhibitors bind to a DFG-in like state but with weaker affinity, *i.e.* in solution a coexistence of both states under all investigated conditions is observed that cannot be resolved using protein X-ray crystallography. This study thus experimentally revealed the existence of a two-state equilibrium for p38α while the addition of inhibitors shifts the equilibrium between these two states.

This approach allowed a direct monitoring of conformational equilibria of the activation loop in a protein kinase using EPR spectroscopy in solution. Quantitative analysis including spectral simulations enabled insights into equilibrium states, which has not yet been possible using state of the art techniques. In contrast to the method demonstrated here, NMR and pulsed EPR studies give direct access to structural information, *i.e.* distance constraints.[212-213] However, the EPR mobility measurements approach provides insights into the two protein states in terms of mobility as compared to the structural changes observed in distance determinations. Moreover, temperature-dependent analysis enabled quantitative insights into inhibitor-induced changes of the structural ensemble.

The results presented in this chapter focus on the dynamics of the activation loop and how it is influenced upon binding of inhibitors. To assess this in a more structure-focused way, further studies using pulsed EPR distance measurements were carried out.

5.3. Structural insights into p38α using long-range distance restraints

In contrast to focusing on the dynamics and their underlying equilibrium states, pulsed EPR allows for a more structurally oriented insight. The precise measurement of not only the distance between two spin labels, but also their flexibility is rendered possible *via* double labeling and distance measurement at cryogenic temperatures. Thus, the structural changes occurring in the activation loop can be resolved with high precision as to be shown in the following.

5.3.1. Distance measurements using multiple label position combinations

The experimental approach requires the introduction of a second spin label in addition to the already introduced label position 172 inside the activation loop. Choosing the same loop label position as in the previous experiments facilitated the expression and ensured that this label is non-perturbing to the protein function. The second spin label had to fulfil several requirements which are typical for many distance measurement studies and are discussed in chapter 3.1.

Having considered all the SDSL factors mentioned in chapter 3.1, five different double point mutation constructs for p38α were chosen (see Figure 42):
A172C + C119C / A277C / A309C / S347C / S251C.

C119 is a native cysteine residue which was replaced by serine in four out of five constructs. In addition, the F327L point mutation (see chapter 5.2) was retained. The constructs will be named after the second cysteine residue (*e.g. p38α 119* for the construct p38α A172C, C119C, F327L) in the following.

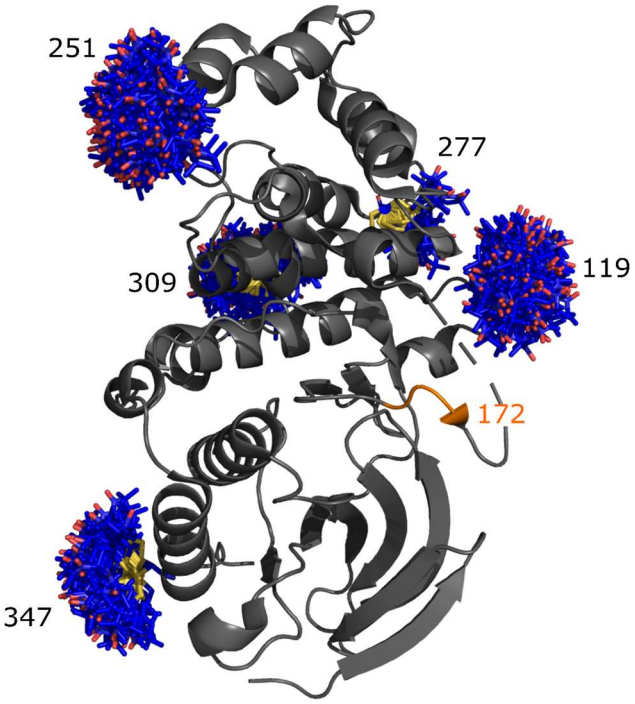

Figure 42: Rotamer calculations for the spin label positions chosen for p38α (PDB 1QUE). The loop region is partly highlighted in orange, calculated spin label rotamers are shown in blue/red. Notably, position 277 has a restricted amount of predicted conformations, presumably leading to narrower distance distributions. Created using PyMOL[67] and MTSSL-Wizard.[198]

Expression, isolation and SDSL procedures were carried out similar to chapter 5.2, except for the doubled amount of spin label added during labeling. The labeling success was monitored using cwEPR. As the estimation of the labeling degree using the comparison of spin counting and protein concentration measurements proved to be unreliable (compare chapter 5.2), the labeling degree was determined in subsequent distance measurements. For a given pump pulse length and shape and thus excitation profile, the obtained modulation depth is proportional to the degree of double labeling. With the given experimental setup, a modulation depth of around 20% was expected (rectangular pump pulse, approx. 20 to 22 ns) and found for all labeling combinations. Thus, quantitative labeling was assumed.

Labeling was successful and highly reproducible for all five constructs. Consequently, distance measurements were carried out for the apo samples. For this, the protein concentration was adjusted to approximately 60 µM. Details on optimal concentrations for DEER experiments can be found in Jeschke *et al*, 2007.[214] In analogy to previously shown experiments, a high deuteration degree in the final sample was pursued. Therefore, the washing buffer in the isolation steps was deuterated by exchange of water with D_2O and usage of perdeuterated glycerol (glycerol-d_8) (see chapter 8.1.3 for details).

With this, distance measurements for all five constructs were obtained with high signal-to-noise ratios, allowing a reliable distances analysis for all the restraints found (Figure 43). Notably, nearly all of the obtained distributions span over a large distance range, *e.g.* p38α 251 constraints span from approximately 1.5 nm (lower detection limit for DEER) to around 5 nm. Broad distances reflect a high flexibility in backbone and/or the spin label linker. Additionally, all measurements as shown in Figure 43 result in bi- or multimodal distance distributions. As shown in chapter 5.2, for apo p38α an equilibrium between loop states is expected. Here, a broad structural variety can be observed for all measured samples. While this behavior is in line with previous results, the distance distributions do not allow a direct interpretation and classification to the DFG-in and DFG-out states, *i.e.* for a bimodal distance distribution, the obvious assumption that each mode belongs to one single state is not necessarily true. It could, *e.g.*, also be explained by the existence of flexible states leading to overlapping distance distributions. In other words, a clear separation of two states in the distance regime is not necessarily the case. In addition, it is difficult to attribute the distance restraints to a specific loop state without further knowledge. This will be discussed in more detail later in this chapter.

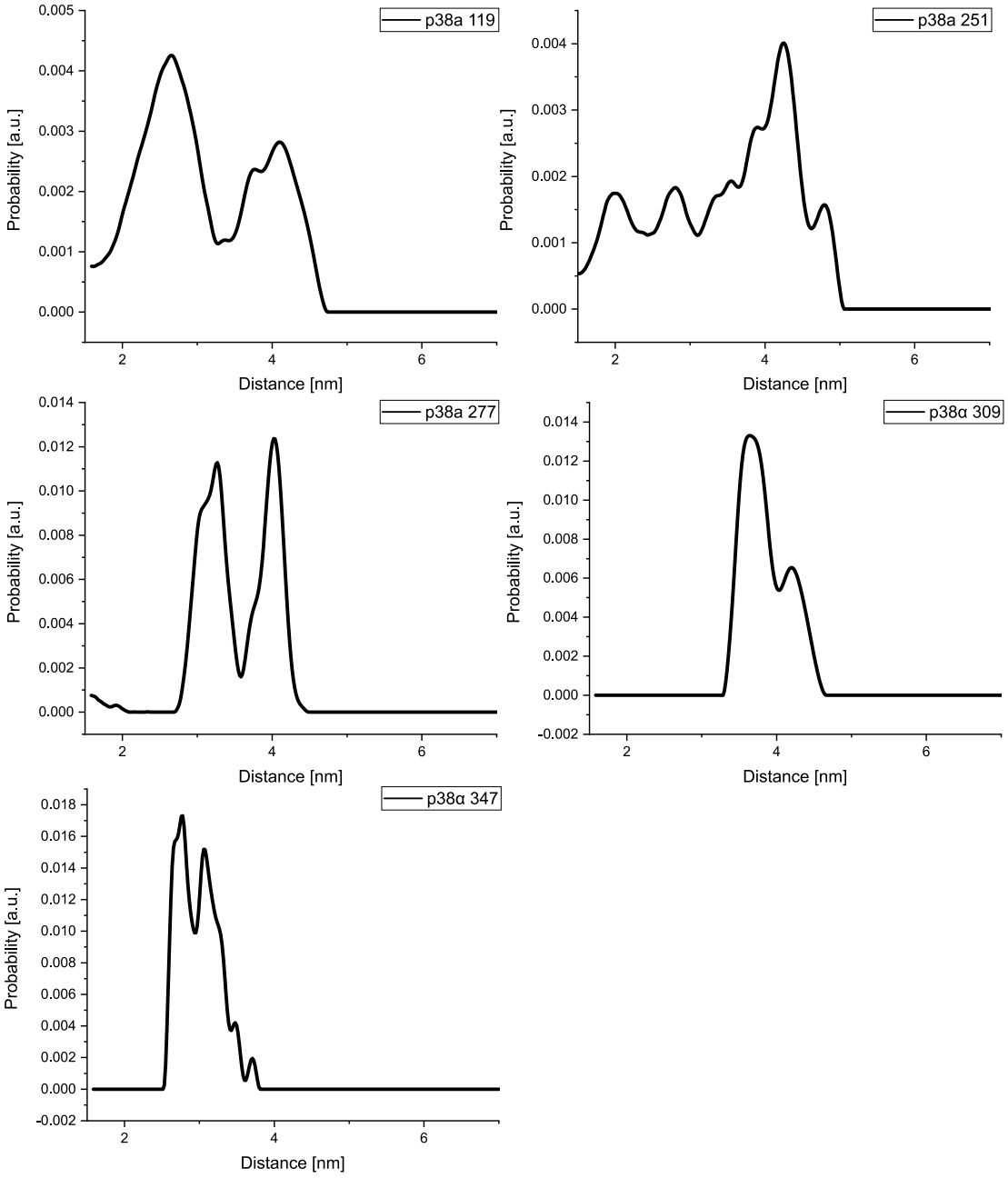

Figure 43: Distance distributions obtained for the five doubly labeled p38α constructs. For raw data and analysis details, see chapter 8.1.3 and Figure A. 20 to Figure A. 24.

5.3.2. ATP binding and its structural impact on p38α

With doubly labeled p38α constructs and thus the possibility to gain distance restraints, the previous experiments aspiring an observation of ATP binding effects to p38α were continued.

As discussed in chapter 5.2, binding of ATP can lead to an increased kinase activity. The structural changes occurring during this interaction are thus a suitable target for further studies. While there were no detectable changes in the EPR mobility experiments conducted in the last chapter, this does not necessarily rule out the presence of structural changes: If changes are not significantly altering the dynamics of the loop region and consequently the spin label, small changes in the three-dimensional structuring of the loop region would be undetectable in a EPR mobility measurement. In contrast to this, DEER is sensitive to even minor structural changes. Thus, the addition of ATP to the p38α constructs was studied using EPR distance measurements (Figure 44, left). The raw data traces are shown in Figure A. 20 to Figure A. 24. The resulting form factors do not exhibit significant differences (Figure 44, right). This can be directly interpreted to indistinguishable distance distributions for these two samples, without further processing *via* Tikhonov regularization. The addition of ATP to the kinase did therefore not induce structural changes detectable with DEER experiments, ruling out one hypothesis from chapter 5.2.

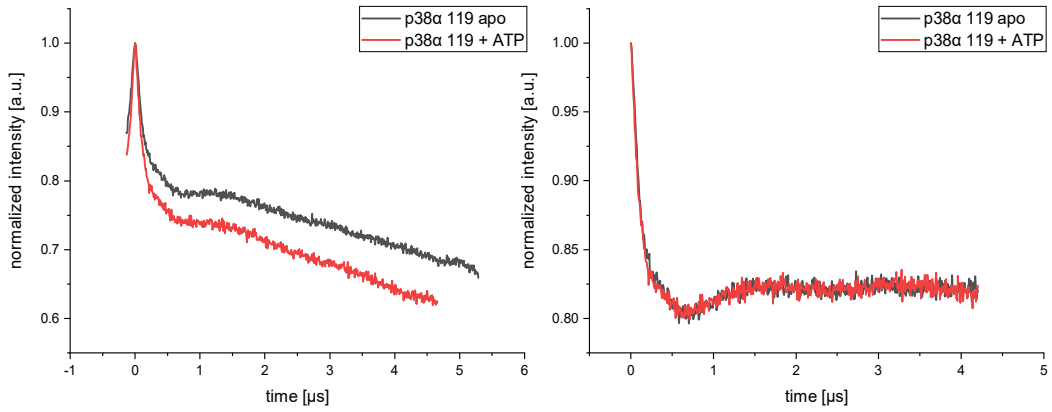

Figure 44: Left: Raw data trace for p38α with (red) and without (black) addition of 7 molar equivalents of ATP. Differences in modulation depth are due to the non-equal pump pulse lengths. Right: Modulation depth scaled form factors for both measurements, showing no significant differences.

ATP in solution is hydrolyzed rather quick, depending on temperature and the solvent it is exposed to. This could, in principal, impede the possibility to detect structural changes of ATP binding to p38α. Thus, two ATP derivatives that are non-hydrolysable were tested (Figure 45): AMP-PNP (Adenylyl-imidodiphosphate) and AMP-PCP (Adenylylmethylenediphosphonate). In these structures, an oxygen atom is replaced with either nitrogen or carbon, substituting the hydrolysable phosphoric

anhydride moiety with more stable imidodiphosphate or methylenediphosphonate groups.[215] Assuming these derivatives are accepted by the kinase and thus act similar to ATP, AMP-PNP and AMP-PCP are considerately more stable and should facilitate distance measurements.

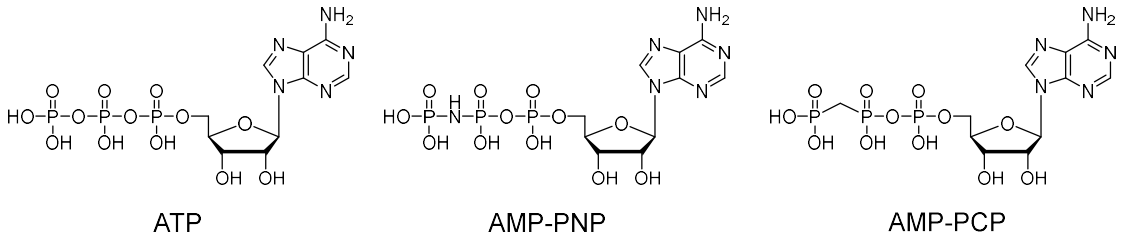

Figure 45: ATP and its non-hydrolysable derivatives used in this study.

In analogy to ATP, excess of ATP-derivatives was added to doubly labeled p38α 277. The distinct bimodal distance distribution found for apo p38α 277 should be sensitive to even minor changes in the structure. DEER measurements were conducted for both AMP-PNP and AMP-PCP, analyzed and compared with the apo protein (Figure 46). A comparison of the modulation depth normalized form factors after background correction showed small differences occurring in the measurement with AMP-PNP. These result in no detectable changes in the distance distributions in all three measurements, though, suggesting that no detectable structural changes occur when the kinase is mixed with non-hydrolysable ATP-derivatives.

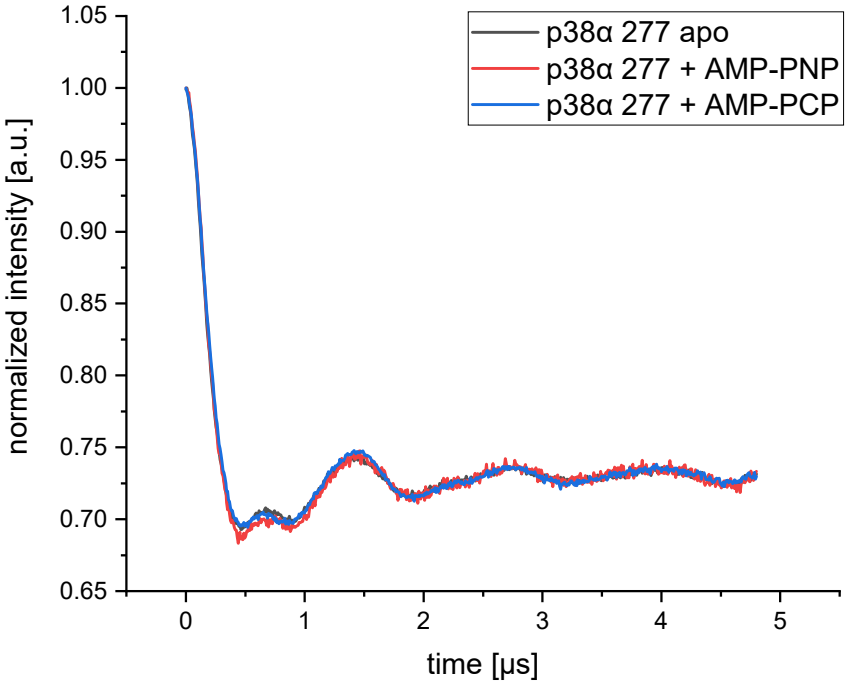

Figure 46: DEER data obtained from measurements with and without ATP-derivatives for p38α 277. The form factor after background correction is shown, normalized to the modulation depths to facilitate the analysis by eye. All three datasets show only insignificant changes.

After having ruled out several possibilities explaining the apparent absence of structural impact of ATP on p38α, as a next step the acceptance of ATP to the kinase was tested. Kinase activity is typically observed *via* activity assays in presence of substrates. The binding of ATP itself is usually not observed directly, but the consumption thereof.

To directly evaluate the binding of ATP, two different approaches were pursued: First, an EPR experiment assessing ATP binding to p38α was designed. For this, two ATP analogues (kindly provided by Daniel Hammler, AG Marx) were used. These compounds, DH140 and DH156, are modified ATP molecules to enable spectroscopic observation (see Figure 47).[216] Both are bearing a modification at the 2′ position containing a linker attached to a standard nitroxide spin label analogue to MTSSL. While in DH140 the linker moiety is rather long, the nitroxide in DH156 is bound closer to the ATP. This should result in different acceptance levels to kinases. While the long linker in DH140 is unlikely to disturb the ATP moiety directly as in DH156, it introduces more steric hindrance to the molecule itself and might be more problematic in tight binding pockets. Thus, the acceptance of both molecules to p38α, which was not tested prior to this experiment, was proposed to be different for these two compounds. Several techniques allow the experimental analysis of binding processes, in this case the observation *via* cwEPR was chosen. While unbound ATP-analogues is expected to tumble fast in solution and result in a narrow, practically isotropic spectrum, binding to p38α should lead to a more restricted rotational mobility and consequentially be reflected in the EPR spectra.

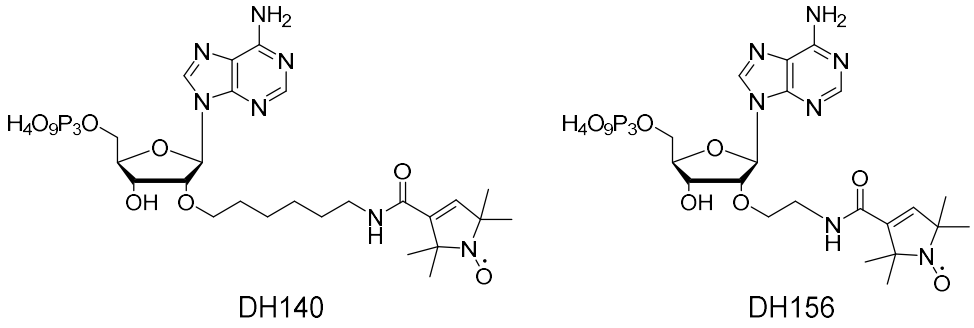

Figure 47: Spin labeled ATP analogues provided by Daniel Hammler, AG Marx. The ATP analogue is modified at the 2′ position with a linker bearing a nitroxide spin label.

To carry out the above described assay, unlabeled p38α (*p38α WT*) with a concentration of 100 µM was mixed with one molar equivalent of either DH140 or DH156 in conjunction with 10 molar equivalents of $MgCl_2$ (all in standard TRIS buffer). The use of only one equivalent of ATP-derivative was reasoned to assure a significant fraction of the compound being bound to p38α and thus avoiding the presence of a large background signal from unbound compounds. Directly after mixing, EPR spectra were collected every 5 minutes to up to 2 hours. By this, binding or relatively fast consumption should both be observable if occurring. Analysis of the resulting spectra showed a

similar picture for both compounds: Both DH140 and DH156 exhibit fast rotational movement reflected in isotropic EPR spectra. The addition of p38α and magnesium salt did not impose a significant impact on the spectral shape (see Figure 48). Binding of the compounds to p38α, be it covalent attachment or only a coordination, should lead to a significant impact on the rotational mobility observable *via* EPR. The apparent absence of changes in the spectral shape can be interpreted as non-binding of these compounds to the kinase. While a spin labeled ATP analogue is certainly a powerful tool to study not only binding kinetics but also for a structural view, at this point binding was be observed.

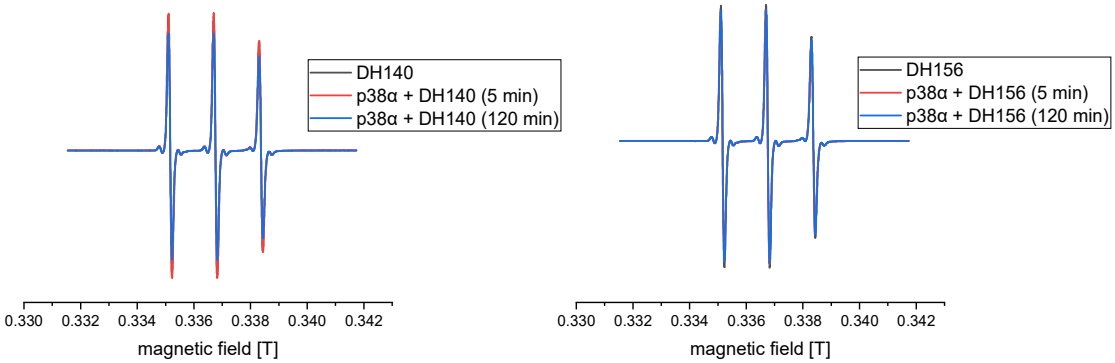

Figure 48: cwEPR spectra for spin labeled ATP-derivatives. Left: Comparison between the free, isolated DH140 (black) and after mixing it with p38α and MgCl2. Time steps of 5 minutes (red) and 120 minutes (blue) are shown. Right: Analogue spectra for DH156 without (black) and with (red, blue) p38α. No distinct changes in line shapes are detectable.

In parallel to the EPR assay, Jörn Weisner conducted an assay similar to the Fluorescence Labels in Kinases (FLiK) assay.[196] In short, binding of substrates to the vicinity of the activation loop changes the local polarity and thus the emission spectrum of a fluorophore attached to the activation loop, at the same position that was used prior to SDSL EPR measurements.

This was done for ATP, AMP-PNP, AMP-PCP, DH140 and DH156. As binding of inhibitors also influences the activation loop region as shown before, the inhibitors SB203580, Sorafenib, Skepinone-L were used as a positive control (see Figure 49). The results suggest no apparent binding effect for the ATP derivatives, while inhibitors show a distinct shift in the fluorescence spectrum. The addition of GST-fused ATF-2, which serves as a substrate for $p38\alpha^{217\text{-}218}$ did not alter the emission behavior for both ATP analogues as well as the control group.

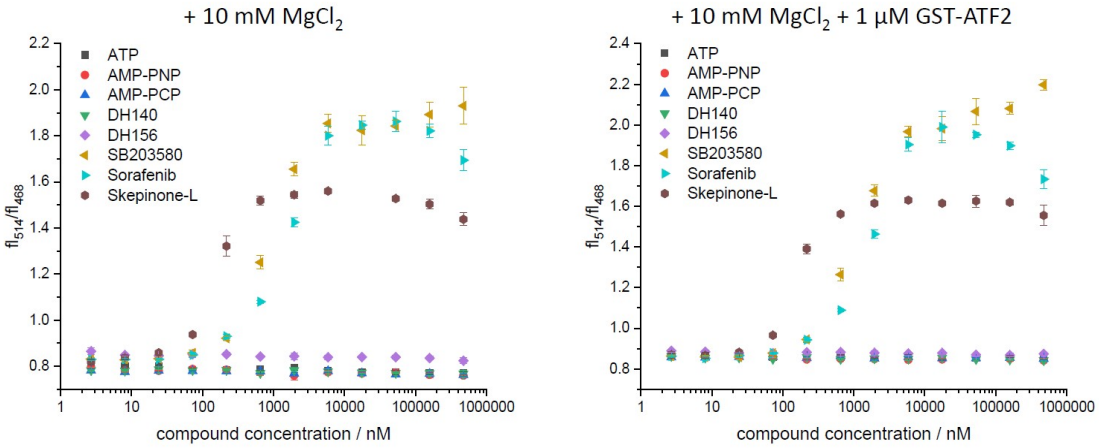

Figure 49: Binding assay carried out by Jörn Weisner, Dortmund. The fluorescence emission spectrum of an attached fluorophore is observed *via* the ratio at 514 and 468 nm. Left: No binding effect on the spectrum is apparent for DH140, DH156, ATP, AMP-PNP and AMP-PCP. Inhibitors (SB203580, Sorafenib, Skepinone-L) show significant binding effects. Right: The same result is observed with the addition of a substrate (GST-ATF2). Image kindly provided by Jörn Weisner.

The results obtained here are in line with the EPR data, showing no apparent binding of ATP to p38α. While this result is surprising for a kinase that is actively consuming ATP in an *in vivo* environment, this is explained by the simplified approach that was conducted here. In a cellular environment, kinases are typically activated in a cascade where mitogen-activated kinase kinases (MAPKKs) such as MKK3 or MKK6 are the key players.[219-221] To circumvent the need for a complex system consisting of a full kinase cascade, the aforementioned F327L mutation was introduced to the sequence. This is known to increase the kinase activity.[195] Apparently, this is not sufficient for this assay, imposing the need for further experiments using pre-activated p38α. While this is challenging due to the rather high sample amounts needed for EPR studies, this will be pursued in further studies.

5.3.3. Inhibitor effects on the activation loop structure

For all five double mutants in their apo state, broad and multimodal distance distributions were obtained (Figure 43). While the addition of ATP and derivatives did not lead to significant changes in the distance distributions, EPR mobility measurement in the presence of inhibitors have shown a large impact on the dynamics of the label attached to the activation loop. With the doubly labeled p38α constructs, EPR distance measurements were conducted in a similar fashion than in chapter 5.2.

In short, the labeled double mutant constructs (with concentrations of approx. 50 to 100 μM) were incubated for 90 minutes at 21 °C in the presence of an excess of 6-fold molar equivalents of the inhibitors RL45, RL48, Sorafenib, Regorafenib, Skepinone-L, SKF-86002 or SB203580. Subsequently, distance measurements were performed in Q-Band at 50 K. While measurements for p38α 119 and 251 were carried out using a Bruker EN 5107D2 resonator and a 15 W solid state microwave amplifier (10 μL sample volume), for p38α 277, 309 and 347 a Bruker QT-II resonator equipped with an arbitrary waveform generator and a 150 W amplifier was used (60 μL sample volume). In all cases, rectangular pulse shapes were applied. Therefore, measurements conducted on the two different experimental setups are directly comparable despite the substantial gain in signal-to-noise ratio upon usage of larger samples. DEER datasets were collected for all five double mutants in combination with either the type I inhibitors (Skepinone-L, SKF-86002 and SB203580) or the type II inhibitors (RL45, RL48, Sorafenib and Regorafenib). Analysis was done using DeerAnalysis 2016 and Tikhonov regularization.[222] For all experimental parameters and data analysis details, see chapter 8.1.3. All distance measurements resulted in data with high signal-to-noise ratios, enabling d2 times sufficiently long for a reliable distance analysis of the detected distances (between 4 and 10 μs). The distances did not exceed 5 nm significantly, which is in the accessible distance range for these samples. In the following, two exemplary datasets are shown which are representative for all measurements. For the full set of raw data and form factors for DEER measurements in presence of inhibitors, see Figure A. 25 to Figure A. 34.

Prior to the comparison of the distance constraints with the ones obtained for the apo protein, the results for the different types of inhibitors were compared. Strikingly, type I inhibitors lead to narrow distance distributions with form factors that were in most cases indistinguishable in the datasets for SB203580, SKF-86002 and Skepinone-L (exemplary data: for p38α 119, Figure 50 left and for p38α 309, Figure 51 left). Comparison of the normalized form factor instead of the raw data traces disposes differences in modulation depths and background densities. The insignificant differences in form factors lead to near-identical distance distributions that deviate mostly because of uncertainties in the Tikhonov regularization applied (Figure 50 right and Figure 51 right). These results are remarkably similar for all five double mutant

constructs studied (see 8.1.3 for all datasets), suggesting that the inhibition with type I is mechanistically highly conserved. While the width of the distance distributions is generally a combination of the inherent flexibilities of the protein structure as well as the spin label linker, a narrow distribution suggests that both of these adopt a rigid conformation. Narrow distance distributions thus can be interpreted as a more rigid structuring of the activation loop region in the vicinity of the spin label linker and the high similarity between the type I inhibitors hint at a distinct conformational state adopted.

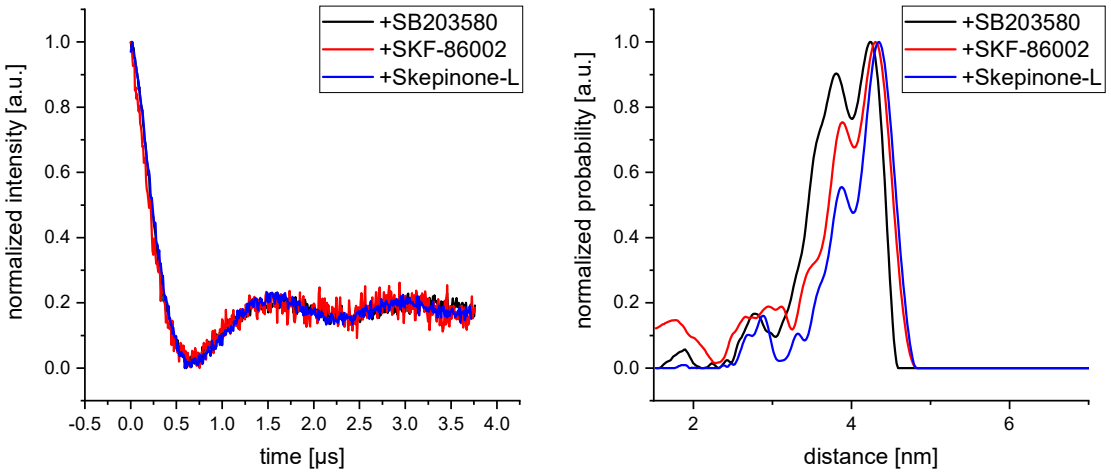

Figure 50: Distance data obtained for p38α 119 in combination with type I inhibitors. Left: Modulation depth scaled form factors obtained for the three type I inhibitors, showing no significant deviances from each other. Right: Resulting distance distributions obtained *via* Tikhonov regularization. Deviations are non-significant and rise from uncertainties in the distance analysis.

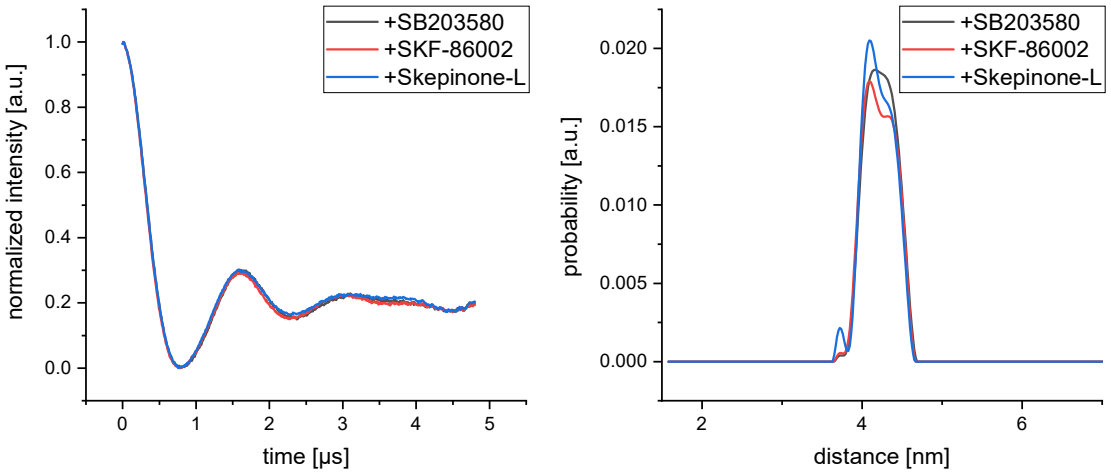

Figure 51: Distance data obtained for p38α 309 in combination with type I inhibitors. Left: Modulation depth scaled form factors obtained for the three type I inhibitors, showing no significant deviances from each other. Right: Resulting distance distributions obtained *via* Tikhonov regularization. Deviations are non-significant and rise from uncertainties in the distance analysis.

Type II inhibitors also led to a profound impact on the DEER data. Comparison of the scaled form factors and resulting distance distributions (exemplary data: for p38α 119, Figure 52 and for p38α 309, Figure 53) shows a high similarity, yet alterations in the form factors can be observed. These are also translated into some diversity introduced to the distance distributions, showing small yet significant variations in the relative distance peak intensities between the different inhibitors. Still, the consensus of type II inhibitors is high while clearly separating them from type I inhibitors. The distributions obtained are typically broader than for type I inhibitors, hinting to more flexibility in the loop region. In contrast to type I measurements, the apparent deviations in the DEER data hints that the conformational space adopted for type II inhibitors is not unique and structural variation is possible.

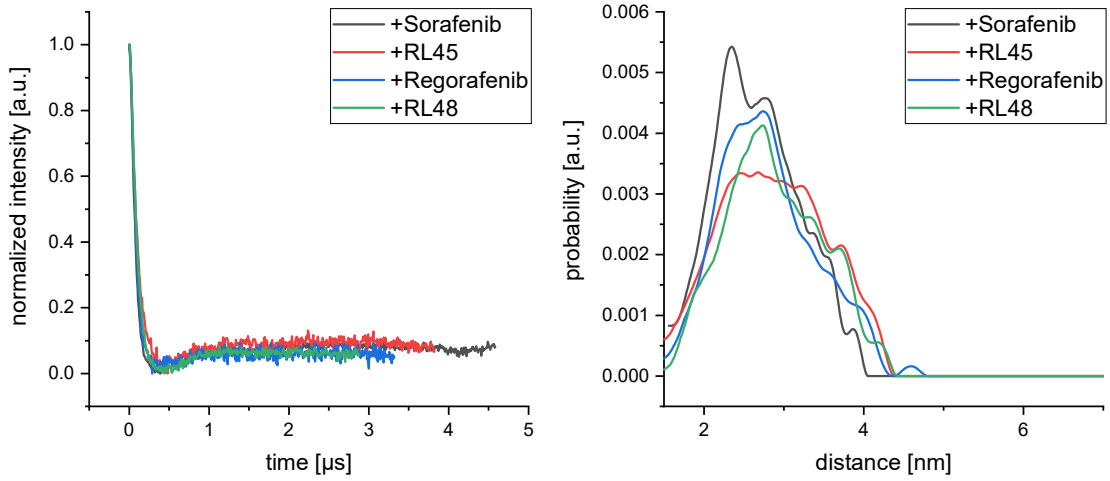

Figure 52: Distance data obtained for p38α 119 in combination with type II inhibitors. Left: Modulation depth scaled form factors obtained for the three type II inhibitors, showing no significant deviances from each other. Right: Resulting distance distributions obtained *via* Tikhonov regularization.

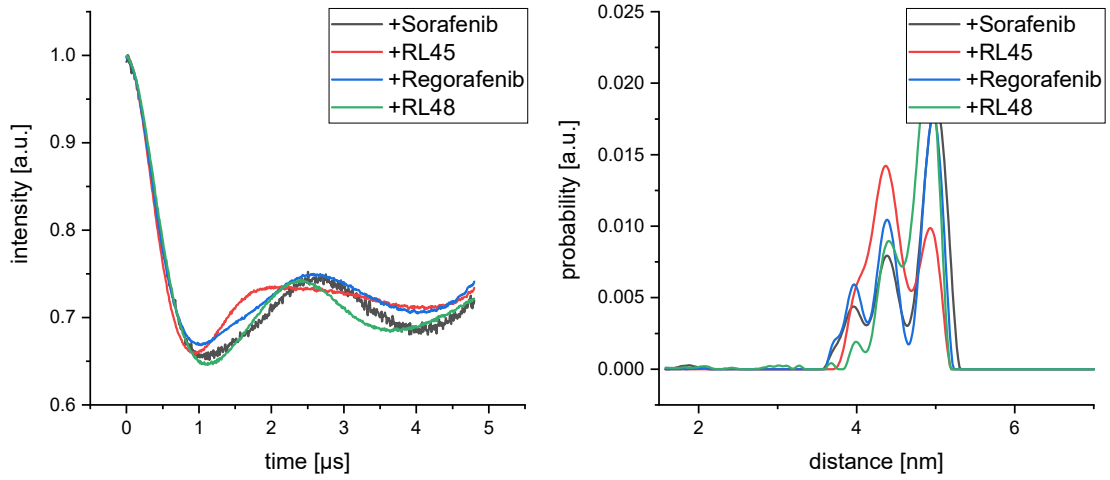

Figure 53:. Distance data obtained for p38α 309 in combination with type II inhibitors. Left: Modulation depth scaled form factors obtained for the three type II inhibitors, showing no significant deviances from each other. Right: Resulting distance distributions obtained *via* Tikhonov regularization.

Next, the distance constraints obtained in the presence of either type I or type II inhibitors were compared with the p38α datasets (Figure 54). For all five double mutants in combination with the seven inhibitors, significant changes in the distance distributions are detectable. Because of the high amount of datasets, the comparison of distance constraints was done for the apo p38α datasets in combination with one type I inhibitor (SB203580) and one type II inhibitor (sorafenib). The distance constraints for all other inhibitors are summarized in Figure A. 35 and Figure A. 36.

In all datasets, distinct variations in the distance restraints for apo p38α, type I inhibitors (as represented by SB203580) and type II inhibitors (represented by sorafenib) are observed. While type I and II inhibitors lead to distance distributions with small to medium overlap with each other, the distribution shapes are clearly separated. The data strongly suggest that the different types of inhibition lead to distinct states of the activation loop that differ not only from each other but also from the apo state.

Type I inhibitors induce narrow distance distributions in all cases, showing a higher rigidity than measurements for the apo protein. In most apo measurements, the data suggests a bimodal distribution. Strikingly, type I inhibitors induce a conformational shift leading to distance constraints strongly overlapping with one of the modes already present in the apo state. This is especially obvious for p38α 119, 277 and 309, where not only the mean distance corresponds to a part of the apo distribution but also the distribution shape is similar. Additionally, the distances covered for type I inhibitor datasets are virtually completely preoccupied in the apo samples and no new distance areas are populated upon ligand binding. These results can be interpreted in that the type I inhibitors bind using conformational selection and stabilize a state which is already present in the structural ensemble for the apo p38α.[223-224]

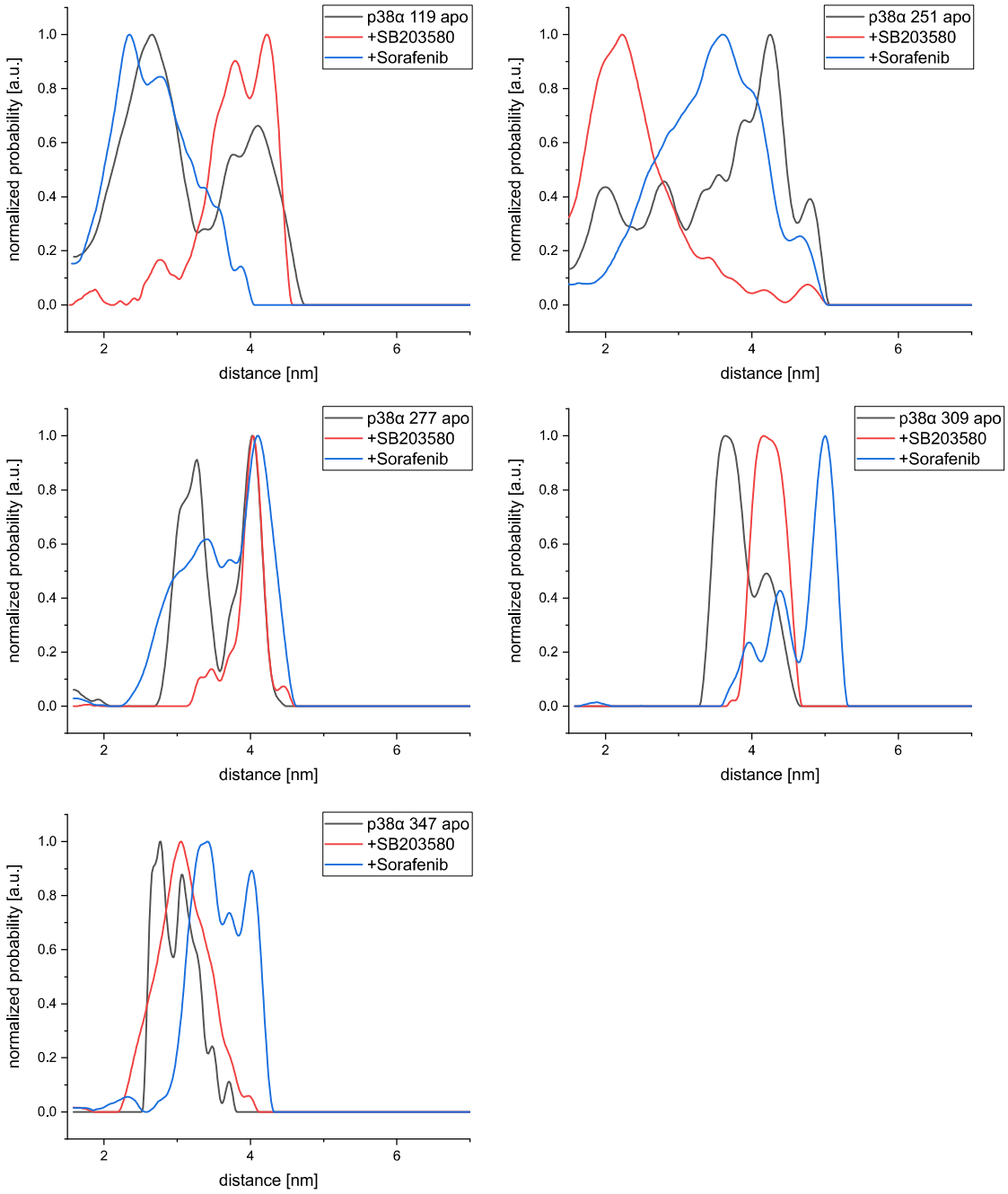

Figure 54: Distance distributions obtained for the five doubly labeled p38α constructs in the presence of either type I (+SB203580) or type II inhibitors (+Sorafenib). For raw data and analysis details, see chapter 8.1.3 and Figure A. 20 to Figure A. 34.

Type II inhibitors led to vastly different results. While the distributions obtained are narrower than for the apo p38α in some cases (*e.g.* for p38α 119), most of the constraints exhibit a comparable width. Still, there is a significant shift in most cases. In addition, the distribution shape is typically altered when compared to the apo data. For all five double mutants there is significant overlap of distance regions present. However, there are also distance regimes that strongly differ from this. This can be seen especially for p38α 309 and 347 (Figure 54), where the majority of distances covered have not been populated before. These observations hint, in contrast to the conformational selection suggested for type I inhibitors, to an induced fit mechanism where the loop structure is

altered after binding of the inhibitor. It should be noted that the results shown do not directly reflect on changes in the binding pocket of p38α, but a conformational change of the activation loop adjacent to this area and thus influenced by substrate binding.

The herein presented results suggest that the influence of small-molecule inhibitors to the kinase structural ensemble is strongly depending on the inhibitor type and that the kinase structural view should be interpreted as a conformational ensemble instead of a steady-state structure typically obtained *via* techniques like X-ray crystallography. This dynamic ensemble allows a preselection for inhibitor binding as suggested for type I inhibitors here. To facilitate the interpretation of these findings, a multilateration approach was conducted and will be presented in the following.

5.3.4. Multilateration of a loop-attached spin label

Due to the evidently high flexibility inherent in the activation loop region, the majority of published crystal structures cover this region incompletely. This is not unexpected due to the highly dynamic nature of the activation loop leading to a broad distribution of electron density. This widely spread electron density hinders structure mapping. Despite said difficulties, structure predictions of p38α in combination with small-molecule inhibitors are available (*e.g.* PDB 3GCU, 3QUE). As observed in the distance measurements, incubation with inhibitors leads to a higher rigidity of the activation loop, thus increasing the chances of successfully mapping it in a crystal structure analysis. Available crystal structure cover for example p38α in combination with the type I inhibitor skepinone-L (3QUE) or the type II inhibitor RL48 (3GCU).

Under the assumption that both the crystal structures and the distance determinations carried out after incubation with the corresponding inhibitors report on the same protein structure in the sample, the distance constraints obtained should coincide with the intramolecular distances predicted for the crystal structures. To evaluate the conformity of both experimental techniques, theoretical distance constraints based on the crystal structure models were simulated. This is conducted using the MMM package (Multiscale Modeling of Macromolecules).[66] In short, two spin labels at the residues used in the DEER experiments are labeled *in silico* using a rotamer library to cover the conformational flexibility inherent to the label itself and its linker to the protein backbone. This flexibility is then included in a prediction of distance constraints for a given pair of labeled residues. Using this with the crystal structures 3QUE and 3GCU, a full set of simulated distance distributions was generated and compared with the experimental results (Figure 55).

Experimental results for p38α double mutants incubated with the type II inhibitor RL48 were compared with the crystal structure 3GCU obtained using X-ray crystallography of p38α in presence of the same inhibitor. The five different constructs lead to diverse distance distributions. While there is significant overlap between the simulations and the experimental results for samples like p38α 309 and p38α 119, there are large deviations in other samples (*e.g.* p38α 251). Taken together, significant deviations between EPR datasets and X-ray based simulations suggest that the structural model found in p38α crystals in presence of type II inhibitors is not consistent with EPR datasets in frozen solution. At least partial overlap is found in all datasets, suggesting that the crystal structure reports on a single conformation that might be reflected in the conformational space found in EPR experiments.

Due to the technical realization of crystallographic studies, it is not possible to report on any conformational freedom in the activation loop region using X-ray studies. The activation loop structure as reported in the X-Ray datasets is representing a single loop conformation. While this indeed could be also covered in the conformational space adopted in solutions and thus selectively retained during crystallization, the found loop structuring could also be induced by the crystallization process. These observations explain obvious deviations between datasets created with EPR and X-Ray studies and highlight the possibility to reflect conformational flexibility in proteins using EPR spectroscopy in frozen solution instead of crystallized protein samples.

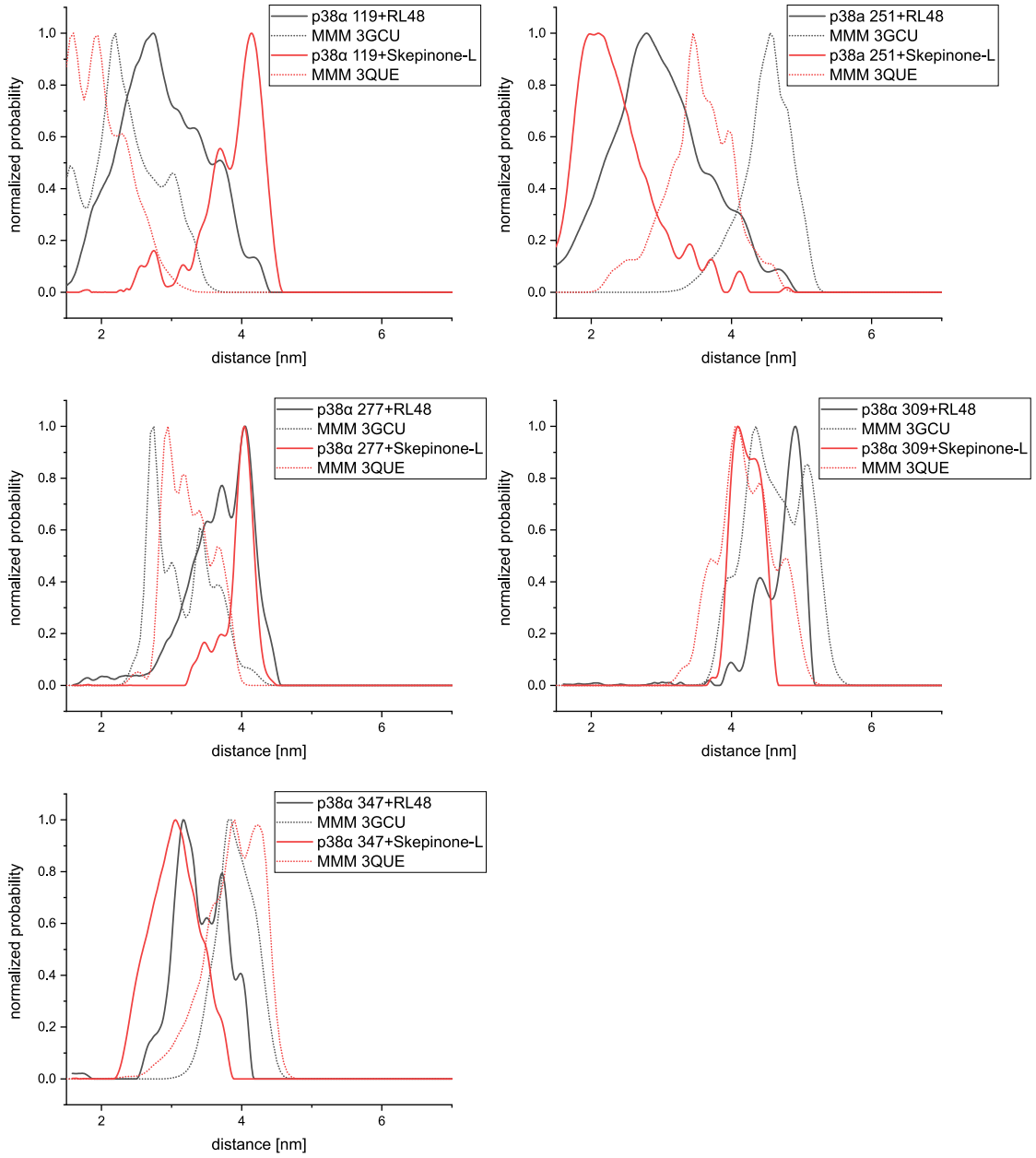

Figure 55: Comparison of simulated distance distributions (dotted lines) obtained *via* calculation of rotamer populations with experimental results (lines). Rotamer calculations were carried out using MMM[66] and the crystal structures 3GCU (p38α bound to RL48) and 3QUE (p38α bound to Skepinone-L). As for experimental results, the experiments conducted in the presence of the inhibitors corresponding to the crystal structure environment are shown.

P38α crystallized in presence of Type I inhibitors is reflected by the structure 3QUE. This model was obtained in presence of skepinone-L and is thus used for the comparison with the experimental data for p38α incubated with this inhibitor. A closer observation of the distance distributions for the five double mutant constructs shows a different situation. While the *in silico* data is overlapping to a significant degree with experimental data for the construct p38α 309, there is virtually no agreement for p38α 119 and 277

datasets. This obvious disagreement leads to the conclusion that in this case the structures observed in DEER experiments differ from those captured in a protein crystal.

The interpretation of the agreement between simulated and experimental distance distributions is helpful for a comparison between results obtained by EPR and X-ray. However, as seen above, the combination of various datasets that differ in the degree of agreement renders it difficult to interpret a comprehensive deduction for the full dataset. A comprehensible analysis that implicitly includes all restraints would be helpful. One approach covering this issues is multilateration.[108, 113, 115, 163, 225] Here, distances obtained from known anchoring points to a target with unknown position are combined in a GPS-like approach to localize the position of interest. For the case of the activation loop region of p38α, the fixed anchoring points are realized by spin labels (termed *anchoring labels* from here on) attached to the rigid areas of the protein while the unknown location is the label attached to the flexible activation loop region. The combination of different distance restraints from evenly distributed anchoring labels to the loop label then allows for a three-dimensional localization of the loop-tethered spin label. Theoretically, three different combinations of distance distributions should lead to two possible locations for the unknown label position. This is reduced to a single, unambiguous space with a fourth label pair, more distance constraints increase the reliability and precision of the method. Notably, for this method also the flexibility of the spin label linker has to be taken account for in a rotamer approach, limiting the maximum achievable precision. Rotamers are calculated for the anchoring labels, this information is included in further data processing. There are several software packages available, the following results were calculated using the multilateration module in MMM.[66] Multilateration should be considered as an alternative way of visualizing EPR datasets while still being based on the same datasets. Therefore, the visualization of distance datasets is helpful to better understand the distance restraints and should not lead to contradictory results.

Multilateration is carried out under the assumption that there is no movement involved for the fixed anchor points, with the exception of spin label flexibility which is included in the calculation. In this case, this leads to the assumption that the p38α structure is rigid in the vicinity of the anchoring labels. While this is typically a good estimation especially for helical structures that were specifically chosen as label areas, the consistency of the protein structure for p38α was reviewed for two crystal structures to ensure the validity of this approach. This was done *via* a crystal structure alignment between the structures 3QUE (p38α in complex with skepinone-L) and 3GCU (p38α in complex with RL48), resulting in a high overlap of protein structures (see Figure 56). No domain movements larger than the inherent uncertainty introduced *via* spin label motions can be detected within these crystal structures, despite the large movements

occurring in the activation loop region. With this, multilateration calculations under the assumption of a rigid protein structure depicts a reasonable approximation.

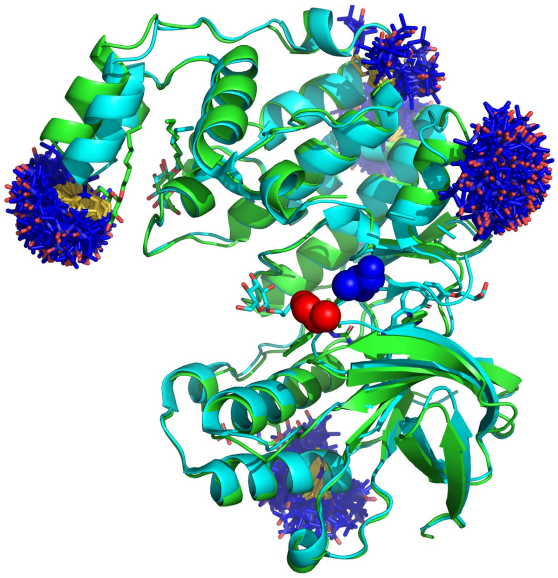

Figure 56: Structure alignment for the structures 3GCU (green) and 3QUE (cyan). The rotamer calculations for the anchoring labels are depicted as dark blue sticks. Positions of the residue 172 are depicted as spheres for 3GCU (red) and 3QUE (blue), respectively. Created using PyMOL[67] and MtsslWizard.[198]

The distance restraints obtained from the anchoring points are approximated with a single Gaussian distribution during the data processing. While this is a good approximation for most of the inhibitor-dependent, unimodal distance measurements, for the broad and often multimodal constraints obtained with p38α apo this imposes significant drawbacks (see Figure 57). The presence of multiple distinct maxima in the distance distribution cannot be reproduced by a single Gaussian curve. For the multilateration approach, this means that some degree of precision in the three-dimensional localization is lost during the data processing. This can be partly compensated by using more than just four distributions necessary for an unambiguous localization. In this case, five double mutant constructs and thus five distribution sets were measured. While measurement precision is thus impeded using the approximation of a Gaussian distribution, the reliability of the localization is largely dependent on the coverage of the Gaussian to the full distance distribution. Assurance that no significant contributions of the experimental distance constraints are lost during data processing is important and indeed this approximation typically covers the whole distance range bearing significant probabilities (see Figure 57). Therefore, multilateration of the spin label attached to the activation loop region is a feasible approach for p38α distance datasets, especially for the unimodal distribution obtained for measurements in presence of either type I or type II inhibitors.

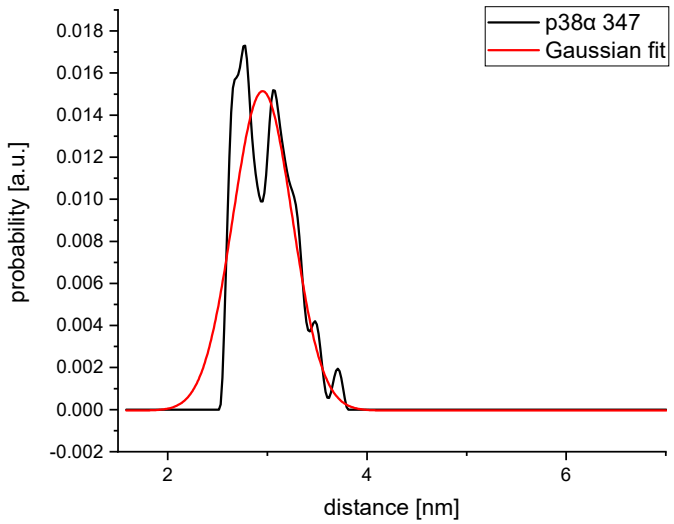

Figure 57: Representation of the Gaussian fit used in the multilateration algorithm. The experimental dataset for p38α 347 (black) features two distinct maxima which are not reflected in the single Gaussian (red).

There are a numerous reported crystal structures available for p38α, yet only in few cases the structure of the activation loop region around the residue 172 is resolved. This is typically the case for samples that are co-crystallized with small molecule inhibitors. Multilateration analysis is not impeded by this, as a rigid structure is only needed around the anchoring labels for the calculation and the activation loop label is localized only depending in the restraints given by the distance distributions extracted from experiments. In addition to this, uncertainty introduced by the spin label flexibility and thus delocalization of the spin centers in the backbone is included in the calculations.

Multilateration for apo p38α

Multilateration for p38α apo was conducted based on the crystal structures 3QUE (Figure 58) and 3GCU (Figure 62) with both including a structural localization of the activation loop region around the label position. Therefore, all the experimental distance constraints for the five double mutant constructs were analyzed using DeerAnalysis and the distance distributions fitted using a Gaussian distribution. The center positions and widths of these were inserted into a restraint file that is interpreted by MMM. Successful calculations are then processed as a volume that represents the three-dimensional probability densities for the spin label positions. The volume of this domain is determined by the sum of the position probabilities, in the following 50 % is chosen, as supposed in the MMM package.[66]

It is important to note that a successful multilateration is only possible if the anchoring spin labels used lead to a robust an unambiguous distance restraints dataset. If there are structural changes around the anchoring labels in the various protein

mutation constructs, the multilateration will not be successful. With the label combinations used, a successful multilateration could be shown in all cases. In Figure 58, the resulting volume for apo p38α is depicted in blue. Notably, the estimation of the spin label position includes a larger area that spans over a significant part of the kinase. This translates into an extensive flexibility of the label and thus the loop region, combined with artificially increased localization uncertainties due to data processing constraints discussed above. Still, the high flexibility was also observable and is in line with the direct interpretation of DEER datasets. For crystal structures that include the activation loop region, an *in silico* rotamer calculation for the spin label introduced at position 172 can be included in the representation, facilitating the interpretation of these structures. For both structures used in the apo multilateration, there is small but significant overlapping between the predicted rotamers and the probability volumes. This impedes a quantitative interpretation, yet leads to the conclusion that the proposed crystal structures include an activation loop structure that might be already present in the apo kinase in solution as already discussed based on the distance restraints.

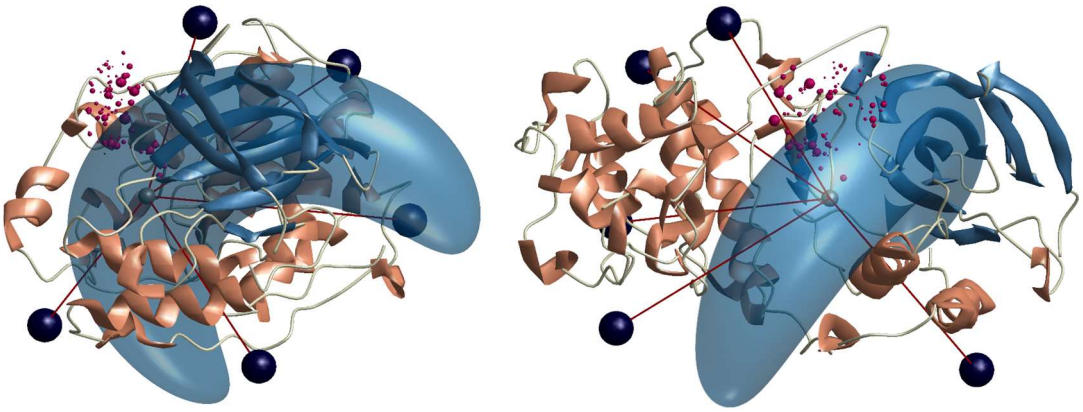

Figure 58: Multilateration result for p38α apo. The secondary structure of the crystal structure 3QUE is shown from two different perspectives together with the rotamers calculated for the spin label attached to the position 172 (purple dots representing the unpaired electron, size of the dots represent the occurrence probability. The center of probabilities for the backbone labels are depicted as dark purple dots, leading to the multilateration of the spin label attached to the activation loop (small blue sphere). The blue volume represents the 50 % probability volume for the localized spin moiety.

Multilateration in presence of type I inhibitors

Type I inhibitors induced a profound narrowing in the distance constraints obtained from DEER experiments, leading to mostly unimodal distributions that were highly conserved for all three type I inhibitors. As the datasets for the different type I inhibitors are virtually indistinguishable, data obtained for skepinone-L was arbitrarily chosen as a representative dataset for the further data analysis. The multilateration using these datasets indeed shows a significant difference to the results obtained for apo p38α (see Figure 59). Instead of the broad probability volume in the absence of inhibitors,

skepinone-L results in an exceptionally narrow localization volume. Notably, this volume is smaller than the one covered by the rotamer simulations for the spin label attached to the activation loop. Therefore, despite the usage of flexible spin labels that impede the achievable precision in this multilateration approach, the position of the loop label was determined accurately. The shape of the probability volume resembles a flat ellipsoid. This could be an effect of the anchoring labels not being perfectly even distributed in space, restricting the analysis resolution in certain dimensions. The localization effect for the spin label implies a higher rigidity of the activation loop region around the amino acid residue 172, which is unexpected because type I inhibitor binding is suggested to be independent of the activation loop structural states, *i.e.* whether DFG-in or DFG-out states are populated.[189] Neither before nor after binding a profound effect of type I inhibitors to the activation loop structure was expected based on crystal structure studies. This again highlights the strength of EPR measurements covering the whole conformational space inherent to the activation loop.

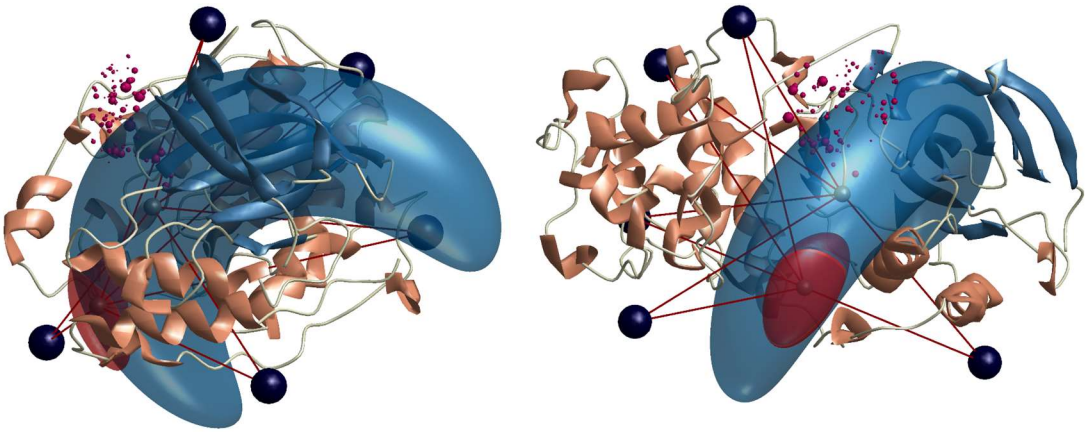

Figure 59: Multilateration result for p38α in the presence of type I inhibitors (exemplary data for skepinone-L), PDB structure 3QUE. The multilateration result from two different perspectives for p38α in its apo state is shown as a blue volume, the result in presence of skepinone-L is shown as a red volume.

In addition to this, the localization of the loop spin label is far off the simulated position for the crystal structure obtained in presence of type I inhibitors as shown in Figure 59. This was also found during the interpretation of the simulated distance distributions that showed only partial overlapping between experiments and simulations. Taken together, this implies that the activation loop structure differs between the crystal structure proposition and the results obtained with DEER spectroscopy. This discrepancy will be further discussed at the end of this chapter.

The analysis of distance constraints for type I inhibitors led to the hypothesis that the adopted structure in presence of type I inhibitors might already be present in the structural ensemble for p38α apo.

This was supported by the remarkably high conservation of specific parts in the bimodal distance distributions for p38α. The multilateration also shows this, as the probability volume with inhibitors has a significant overlap with the volume obtained for the apo protein, thus leading to the conclusion that the adopted conformation might already be present in apo p38α. This again hints to a conformational selection process when the inhibitor is bound to the kinase.

Restrained datasets for the multilateration in p38α apo

Following the supposition that type I inhibitors follow a conformational selection mechanism, the distance constraints obtained for apo p38α are based on a mixture of two conformational substates (DFG-in and DFG-out) and one of them is selectively stabilized upon inhibitor binding. Notably, with the method presented here, it is not distinguishable if the activation loop structural changes occur after binding of the type I inhibitor or are selectively stabilized during binding. In both cases, the distance regimes that were not selected upon inhibitor binding could include structural substates already present in the apo protein. These areas were thus selectively isolated for a multilateration with increased precision. For this, the superposition of distance constraints for apo p38α and datasets in presence of SB203580 were taken to selectively remove all the areas that are covered in the inhibitor measurements from the apo dataset (illustrated in Figure 60). This reduced dataset was then processed similar to the previous results.

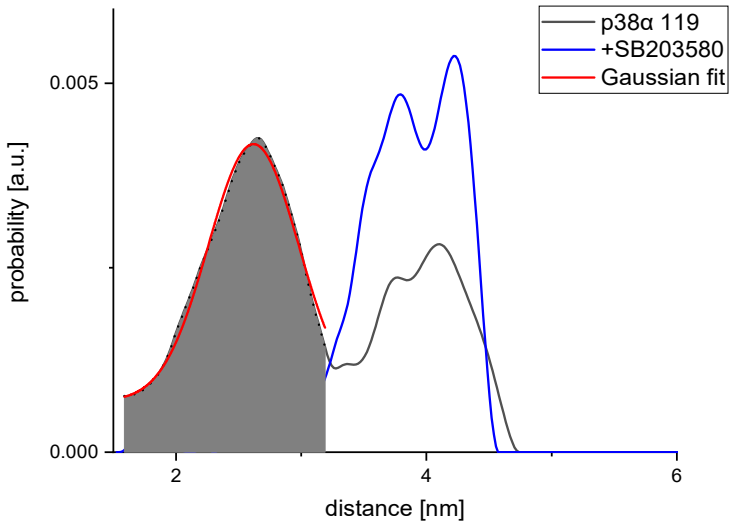

Figure 60: Exemplary dataset for the restriction of distance constraints. The dataset obtained in presence of SB203580 (blue) was used to remove populated distance regimes from the p38α 119 apo dataset (black curve), resulting in a reduced distance distribution (red curve, grey area).

After reducing datasets for all five double mutant constructs, an additional multilateration analysis was carried out (see Figure 61). This showed a significantly reduced probability volume for apo p38α, located in the center of the original volume with the full dataset. Still, the probability volume obtained is larger than for the datasets obtained in the presence of inhibitors. A clear separation of the label location probability for this and the dataset in presence of inhibitor shows that the structural substates covered differ significantly from each other. It can be suggested that the apo protein consists of two different substates that are clearly separated from each other. This is in line for the expectations that apo p38α adopts an equilibrium between DFG-in and DFG-out states. The conformational space adopted in apo p38α can thus be described with the superposition of the red and yellow probability volumes in Figure 61.

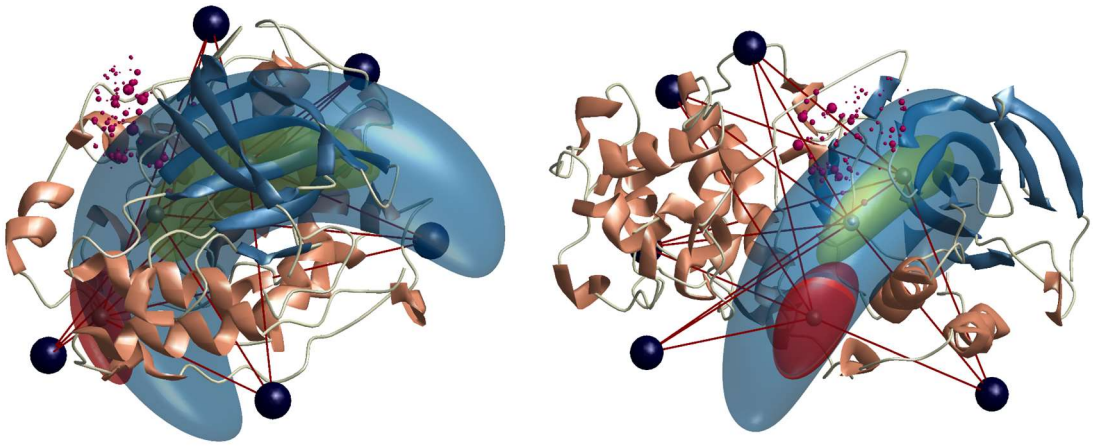

Figure 61: Multilateration result for p38α, PDB structure 3QUE. The multilateration result from two different perspectives for p38α in its apo state (blue volume), with skepinone-L (red) and with the reduced distance constraints (yellow volume, see text) is shown.

While this method of reducing experimental datasets can possibly be used to increase the location precision for the apo measurements, there are some caveats that should be considered. The removal of distance contributions obtained with type I inhibitors presumes are clear separation of distance areas from apo datasets. This assumption is not necessarily correct and could lead to artificial narrowing of the probability volume for the restricted dataset by removing inherent distance constraints overlapping with the type I dataset. This limitation cannot be circumvented using the methods proposed here, thus the restriction of datasets should be considered cautiously. A possible improvement could be achieved with TRIER[226] experiments revealing the correlation of multimodal peaks in the distance constraints. This could help to pin-point the individual loop states with more precision.

Notably, both approaches to estimate the activation loop label position in apo p38α lead to the same conclusions about the structural changes occurring upon inhibitor

binding. The following multilaterations are thus carried out with the full and thus overestimated apo p38α dataset.

Multilateration in presence of type II inhibitors

Distance measurements in presence of type II inhibitors showed a narrowing of the obtained distance distributions, although to a lesser degree than for type I inhibitors. In the following multilateration, a slightly larger probability volume for type II inhibitors is thus expected. Therefore, distance measurements obtained for these inhibitors were processed similar than already shown above. As there were significant deviations in the distance constraints for different type II inhibitors, in this case the multilateration was carried out for all molecules. Despite the apparent deviations, the probability volumes obtained have a high positional agreement and only differ in their dispersion (see Figure A. 37). The analysis is consequently carried out focusing on the results obtained for sorafenib as a representative dataset. As already predicted by analyzing the distance constraints, the presence of type II inhibitors also restricts the movement in the activation loop region (visualized in Figure 62). The probability volume obtained is significantly smaller than for apo p38α, yet not as localized as for type I inhibitors. This implies a higher translational freedom for the activation loop with type II inhibitors in comparison to the case in presence of type I inhibitors. Still, the activation loop seems to be far more constricted in the presence of type II inhibitors than for apo p38α. Analysis of the distance constraints lead to the hypothesis that the structure adopted with type II inhibitors could be outside the ensemble present in the apo protein. This could also be seen in the separation of distance constraints between samples with or without inhibitor, in addition to the shape of the distance constraints which was not conserved. The multilateration further strengthens this proposition as the probability volume obtained has only minor overlap with the volume obtained for apo p38α, explainable with an induced-fit mechanism adopted.

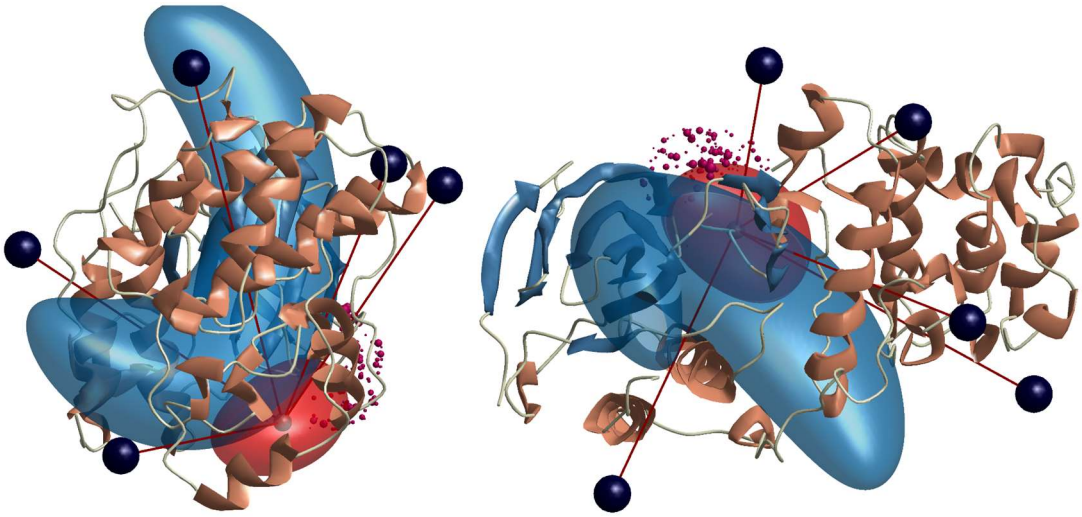

Figure 62: Multilateration result for p38α in the presence of type II inhibitors from two different perspectives, PDB structure 3GCU. The multilateration result for p38α in its apo state is shown as a blue volume, the result in presence of sorafenib is shown as a red volume.

Considering the results obtained, using multilateration techniques the loop region could be localized for apo p38α as well as with type I and II inhibitors. Data analysis using Gaussian distributions was unproblematic especially for dataset in presence of inhibitors due to their unimodal nature. For apo distributions, the usage of Gaussians leads to artificial enlargement of the probability volume obtained, possibly hindering a more concise conclusion for the structural ensemble.

In summary, pulsed distance determination conducted using doubly spin labeled p38α constructs enabled the analysis structural aspects of the biologically crucial activation loop in this kinase. After a careful evaluation of suitable labeling positions, DEER measurements were conducted for apo p38α as well as an inhibitor assay using three type I and four type II inhibitors.

Large deviations were found between the loop positions suggested from crystal structures and the ones found in the experiments presented here. This is not only caused by the intrinsic limitation of crystallographic studies to a single unambiguous structure. The obvious disparity between the observed structures might be due to the different sample preparations. While EPR distance measurements are carried out in a glassy buffered solution that has been rapidly frozen (thus expected to retain most of the conformational ensemble present at room temperature), crystallization is a process involving more artificial steps (resulting in prolonged time consumption). In addition to this, crystallization often requires the presence of helper molecules like beta-octyl glucoside which can disturb the structure of the protein of interest.[227]

For apo p38α, broad distance distributions that are often bi- or multimodal were detected. This result is in line with EPR mobility measurements carried out in chapter 5.2. However, both type I as well as type II inhibitors led to significant shifts in this conformational equilibrium. Type II inhibitors are found in an exclusively populated DFG-out state in crystal structures.[12] While this state is expected to be already in the apo form, the results presented here lead towards the assumption of the "DFG-out" conformation found in crystal structures is the result of an induced-fit mechanism of inhibitor binding. This is supported by the distance constraints obtained with type II inhibitors that deviate significantly from the distributions for apo p38α in terms of the center distances as well as the distribution shape. This is further embraced by multilateration results, suggesting the probability volume of the spin label attached to the activation loop is in a distinct and separate location when type II inhibitors are present. The structural flexibility of the loop region is reduced due to these inhibitors, shown in both narrowing of the distance distributions and the diminished probability volume obtained in multilateration. The four different inhibitors lead to non-equal distance distributions suggesting a certain range of mechanistic disparity, yet the multilaterated positions only differed in their dispersion. Thus, type II inhibitors result in distinct and reproducible conformational changes.

Type I inhibitors exhibit much more similarity. The distance constraints obtained as well as the multilateration results did not significantly differ for any or the three inhibitors tested, suggesting a high mechanistic parity between type I inhibitors. The broad distance distributions obtained for p38α apo state were narrowed down to remarkably narrow distributions, showing a high ordering for the activation loop region

in presence of these inhibitors. While type I inhibitors are suggested to bind both the DFG-in and DFG-out structure without a distinct structural impact on the activation loop,[189] the distance distributions as well as multilateration clearly show a high degree of ordering and rigidity around the activation loop spin label. As distance measurements are collected after incubation time, this does not preclude the unspecific binding of type I inhibitors to the DFG-in or DFG-out structure. This observation can be explained with a conformational selection mechanism, leading to a structural change in the kinase appearing only after the inhibitor is already bound. This is supported by the distance constraints obtained, which not only overlap with parts of the distributions already present in apo p38α but also maintain the shape of these modes. Multilateration lead to an unexpectedly small probability volume that has a high overlap with the one obtained for the apo form, further supporting a conformational selection mechanism.

The results shown in this chapter highlight the broad applicability of EPR in the analysis of broad conformational equilibria found in the activation loop region in p38α. Using EPR distance determinations, deeper insights into the structural effects of inhibitors on the kinase structure could be gained that help understanding inhibition mechanisms.

6. Summary

Two biologically relevant examples of molecular disorder were structurally investigated using a combination of several experimental and simulation methods. While the analysis of ASYN-based peptide fragments implicated complete molecular disordered ensembles, the activation loop in the protein kinase p38α introduced additional boundary constraints by a rigid protein structure around the activation loop.

In order to assess structural features in the intrinsically disordered protein ASYN, a model system consisting of specifically designed peptide fragments was developed. After selection of suitable peptide fragments, their applicability to represent the full-length protein was successfully assessed with multiple experimental techniques and solvent environments. The choice of suitable spin labels as well as the in-depth control of experimental parameters for EPR distance measurements was shown. With this, a suitable platform for a direct comparison of experimental restraints with simulated datasets obtained from MD simulations was created. Two peptide fragments bearing a disease-linked point mutation were objected to further structural analysis. While the introduction of the A30P mutation did not lead to significant structural changes in aqueous solutions, profound variations were found upon helix formation. In this case the potential of a combinatorial approach was shown by the possibility to not only detect these changes in experimental distance constraints but additionally elucidate these based on the simulated molecular structuring. In-depth knowledge about the helicity around the mutation point was obtained, highlighting helix breaking only in the direct vicinity of the A30P mutation. This could be used in further studies to assess the biological impact of the altered tendency in helix formation upon interaction with biological systems, emphasizing the great potential for this combined approach.

For the kinase p38α, intrinsic disorder was assessed in another approach. While the activation loop that was studied is structurally disordered, its attachment to the rigid protein structure allows for a different analysis. In this chapter, the focus was not to elucidate the discrete structure of this region but changes occurring upon interaction with binding partners such as small-molecule inhibitors. With the attachment of a single spin label in the activation loop, dynamic information in the close vicinity of the label and thus the loop region could be obtained. Using EPR mobility measurements and the discrete interpretation of datasets, a dynamic equilibrium inherent to the apo p38α was revealed. Upon addition of inhibitor molecules this equilibrium was shifted and followed quantitatively. The experimental approach allowed temperature control in a biologically relevant range that could also be utilized for the thermodynamic analysis of equilibrium states.

Using EPR distance determination, these insights could be augmented with structural constraints. EPR spectroscopy supported the findings of an equilibrium between different activation loop states that is altered in the presence of inhibitors. These structural changes could be precisely followed, revealing distinct differences in inhibitors targeting behavior to the activation loop states. While type II inhibitors led to a restructuring upon binding to the kinase in an induced-fit like mechanism, distance constraints obtained in the presence of type I inhibitors are mainly populated by regions preoccupied already in the apo p38α. With this, binding exhibits a conformational selection type of mechanism for type I inhibitors. In addition to the analysis of distance constraints, multilateration of spin labels proved to be a valuable tool to visualize the large amount of EPR data into a three-dimensional localization of the loop-attached spin label. Visualization of the structural impact induced by the inhibitors was possible, facilitating the analysis of the underlying mechanics. The insights obtained are helpful for a structure-based design of future compounds and could facilitate the development of specific inhibitors.

7. Zusammenfassung

Zwei biologisch relevante Beispiele für molekulare Unordnung wurden mittels einer Kombination mehrerer experimenteller und Simulations-Methoden untersucht. Die Analyse von alpha-synuclein (ASYN) basierter Peptidfragmente war hierbei beispielhaft für vollständige molekulare Unordnung, während die Aktivierungsschleife in der Proteinkinase p38α zusätzliche Randbedingungen mittels einer starren Proteinstruktur in der Umgebung der Aktivierungsschleife bereitstellte.

Um die strukturellen Eigenschaften des intrinsisch ungeordneten Proteins ASYN zu untersuchen, wurde ein Modellsystem basierend auf speziell entworfener Peptidfragmente entwickelt. Im Anschluss an die Auswahl geeigneter Fragmente, wurde ihre Eignung als Modellsystem für das Volllängenprotein erfolgreich mittels mehrerer experimenteller Techniken und Lösungsmittelumgebungen untersucht. Die Wahl passender Spinmarker und die präzise Kontrollierbarkeit der experimentellen Parameter für Elektronenspinresonanz (ESR) Abstandsmessungen wurde gezeigt. Damit wurde eine geeignete Plattform für den direkten Vergleich experimenteller und simulierter Daten geschaffen. So wurden zwei Peptidfragmente, die eine Krankheitsbildverknüpfte Punktmutation enthalten, für weitere Strukturuntersuchungen ausgewählt. Obwohl die Einführung der A30P Mutation nicht zu signifikanten Strukturunterschieden in wässriger Lösung geführt hat, konnten deutliche Unterschiede bei der Helixbildung beobachtet werden. Hier konnte das Potential eines kombinatorischen Vorgehens in der Möglichkeit gezeigt werden, nicht nur Unterschiede in den experimentellen Abstandsverteilungen zu erkennen, sondern diese auf basierend auf simulierten molekularen Strukturen zu erfassen. Damit wurden tiefergehende Einblicke in die Helizität in der Umgebung der Punktmutation ermöglicht, die das Brechen der Helix ausschließlich in der direkten Umgebung der A30P Mutation zeigten. Dies könnte in weiteren Studien verwendet werden, um den biologischen Einfluss der veränderten Helixbildungstendenz bei der Interaktion mit biologischen Systemen zu untersuchen und hebt das große Potential dieses kombinatorischen Vorgehens hervor.

Im Falle der Kinase p38α wurde intrinsische Unordnung auf eine andere Art untersucht. Obwohl die untersuchte Aktivierungsschleife strukturell ungeordnet ist, erlaubt ihre Verbindung zur starren Proteinstruktur eine andere Herangehensweise. In diesem Kapitel lag der Fokus nicht auf der Aufklärung einzelner Strukturen dieser Region, sondern bei Unterschieden, die bei der Wechselwirkung mit Bindungspartnern

wie Inhibitoren auftreten. Durch das Anbringen eines einzelnen Spinmarkers in der Aktivierungsschleife konnten dynamische Informationen über die direkte Umgebung des Markers und damit der Aktivierungsschleife erhalten werden. Mittels ESR Mobilitätsmessungen und der Interpretation der Daten wurde ein dynamisches Equilibrium in p38α gezeigt. Bei der Zugabe von Inhibitor Molekülen wurde dieses Gleichgewicht und seine Verschiebung quantitativ verfolgt. Der experimentelle Ansatz ermöglichte Temperaturkontrolle in einem biologisch relevanten Bereich, was für die thermodynamische Analyse von Gleichgewichtszuständen genutzt werden konnte.

Mittels ESR Abstandsmessungen konnten diese Kenntnisse mit strukturellen Informationen erweitert werden. ESR Spektroskopie unterstützte den Nachweis eines Gleichgewichts zwischen verschiedener Aktivierungsschleifenzustände, das in der Gegenwart von Inhibitoren verändert wird. Diese strukturellen Änderungen konnten präzise verfolgt werden, um spezifische Unterschiede bei Inhibitoren und ihrem Einfluss auf die Aktivierungsschleifenzustände aufzuzeigen. Während Typ II Inhibitoren zu einer Strukturänderung bei der Bindung an die Kinase mittels eines *induced-fit* ähnlichem Mechanismus führten, sind die erhaltenen Abstandsverteilungen in der Gegenwart von Typ I Inhibitoren hauptsächlich mit Regionen besetzt, die schon in Apo p38α besetzt waren. Damit zeigt die Bindung einen *conformational selection* Mechanismus. Zusätzlich zur Analyse der Abstandsverteilungen, zeigte sich die Multilateration der Spinmarker als wertvolles Werkzeug zur dreidimensionalen Darstellung des Aktivierungsschleifengebundenen Spinmarkers anhand großen Anzahl an ESR Daten. Damit konnte der strukturelle Einfluss der Inhibitoren bildhaft dargestellt werden, was die Analyse der zugrundeliegenden Mechaniken erleichterte. Diese Erkenntnisse sind hilfreich für ein strukturbasiertes Design zukünftiger Stoffe und könnte die Entwicklung spezifischer Inhibitoren vereinfachen.

8. Experimental details

8.1. Methods, materials and data analysis

All chemicals, if not otherwise stated, were purchased by Sigma Aldrich Co. LLC. Milli-Q water was generated by using a Milli-Q Academic Ultrapure Water System (Merck KGaA, Darmstadt, Germany).

TRIS buffer was prepared to a final concentration of 20 mM TRIS, 200 mM NaCl and 5 % glycerol (v/v), pH 7.4. Deuterated buffer was obtained by solvent exchange after evaporation of water under reduced pressure.

8.1.1. Studies conducted in chapter 4

Circular dichroism

CD measurements were performed on a Jasco J-815 spectropolarimeter (Jasco Analytical Instruments) at 20° C. Sample volume was 100 µL and quartz glass cuvettes with a path length of 0.5 mm (Hellma, Forest Hills, NY) were used. Spectra were recorded over a range of 170 / 180 nm (depending on the sample absorption characteristics) to 260 nm using a resolution of 0.5 nm, a bandwidth of 1 nm and 50-100 nm/ min scan speed. CD signals were discarded in wavelengths regions were high absorption led to photomultiplier voltages above approx. 500 V. The typical sample concentration was set to 0.2 mg / mL or 50 µM.

Measurements in the presence of LUVs were conducted with 4 mg / mL lipid concentration and after incubation for 30 minutes. All measurements were averaged over at least 10 scans, depending on the signal-to-noise ratio for each sample.

Analysis of CD spectra

This was done *via* a direct interpretation of the resulting CD spectra by eye. In principal, a quantitative analysis of CD signals to dissect their secondary structure contents is possible. This involves a very precise knowledge of several measurement parameters, including the optical path length and the compound concentration. In this study, the available peptide amounts were limited as EPR distance measurements do not rely on large samples volumes. Therefore, CD measurements were carried out with small sample volumes and short optical path cuvettes. Due to the absence of aromatic systems in many of the peptides, the determination of compound concentration could not be carried out optically and was done by weighting of dried stock peptides. This leads to a significant error in concentration in the stock solutions that is also largely affected by the typical hydrophilicity observed for freeze-dried peptide samples.

Additionally, cuvettes with short path lengths suffer from significant uncertainties due to the mechanic flexibilities. For CD signals, the data is often converted to the mean residue ellipticity (MRE), normalizing CD signals to the number of residues in addition to the sample concentration. This leads to comparable CD data even for samples with large size differences. This was calculated for measurements in aqueous solution and resulted in significant differences throughout the peptides (see Figure 7 bottom). These uncertainties are the sum of experimental limitations as explained above. Therefore, a quantitative calculation of secondary structure elements for CD datasets was omitted in most cases and the datasets were typically not converted into units of MRE in the following. In cases where it is applicable, standard spectra normalization was used to facilitate spectral shape comparisons.

Preparation of LUVs

Dried anionic POPG (1-palmitoyl-2-oleoyl-sn-glycero-3-phospho-(1'-rac-glycerol), Avanti Polar Lipids) was reconstituted with 300 µL Milli-Q to a final concentration of 40 mM. LUVs were prepared by repetitive extrusion using a handheld extruder (Avanti Polar Lipids) and polycarbonate films with 100 nm pores. Resulting LUVs were approx. 100 nm in diameter as observed *via* dynamic light scattering. Total lipid concentration as determined according to Chen *et al*.[228]

Site-directed Spin labeling

Peptide spin labeling using MTSSL was conducted by mixing the peptide solution (approx. 500 µM) with 6 equivalents of spin label in DMSO (stock solution, 10 mM) and incubation overnight. Isolation of the labeled peptide was conducted using HPLC chromatography and ESI-MS analysis.

Pulsed EPR experiments

Pulsed experiments were performed on a Bruker Elexsys E580 Q-band spectrometer using a Bruker EN 5107D2 resonator equipped with a 15 W solid state microware amplifier and a helium gas flow system (CF935, Oxford Instruments). The sample volume was 10 µL, samples were snap frozen in liquid nitrogen by dipping the filled sample tube into LN_2 and afterwards directly inserted into the resonator. Freezing with isopentane was carried out accordingly after the liquid isopentane was cooled using liquid nitrogen to around -160 °C. The resonator temperature was fixed to 50 K.

Distance measurements were carried out using a standard 4-pulse DEER experiment using the pulse sequence

$\frac{\pi}{2_{obs}} - \tau_1 - \pi_{obs} - t - \pi_{pump} - (\tau_1 + \tau_2 - t) - \pi_{obs} - \tau_2 -$echo.[95] The shot repetition time was optimized to prevent saturation of longitudinal relaxation of the nitroxide labels. Pump and observer frequencies were optimized for every sample and range between 20 and 24 ns for the pump and 24 to 40 ns for the observer pulses. The

magnetic field was set to the maximum of the nitroxide spectrum and the observer pulse frequency was set to about 50.4 MHz lower than the pump pulse frequency. Nuclear modulation averaging with 8 steps was used to suppress nuclear modulation artefacts. Accumulation times largely depended on the sample quality and solvent used and typically ranged between 4 to 20 hours. The dipolar evolution time was optimized for each sample to yield reliable distance information while retaining a high signal-to-noise ratio.

DEER distance distribution analysis

The raw DEER data was processed using Matlab 2017a and DeerAnalysis2016.[222] The zero time and the background start was determined using the built-in optimization function, typically the last 10% of the DEER curve were cut manually to remove artefacts in the data trace. The distance distribution was extracted using a three-dimensional background and Tikhonov-regularization. While the α parameter was typically determined automatically using the L curve criterion, in some cases a slightly larger α parameter was chosen to prevent over sharpening of the distance distribution.

Molecular dynamics simulations (Kindly provided by Christoph Globisch)

The α-synuclein fragments P3/P4/P5 have been simulated in their native sequence without explicitly introducing the TOAC label but extended by glycine residues as present in the TOAC labeled peptides (P5 fragment: native AG…GV, labeled (T) GTG… GTG-NH2, simulated GAG… GVG-NH2). The motivation was to stay as close as possible to the native fragment but be at the same time still be close to the experiment. To report the right distance between the spin labels a virtual side for the NO oxygen atom was calculated based on the positions of the backbone atoms of the TOAC replaced amino acid. The position of the virtual point was extracted from a quantum mechanics optimized TOAC structure, where the geometry optimization was performed with GAMES US1 applying initially the semi empirical method AM12 and subsequently by UHF with the 6-31G(d,p) basis set. A projection of the NO oxygen position with respect to the N, CA, CO backbone atoms was extracted from the optimized TOAC structure and then projected for all α-synuclein conformers.

Force fields

All molecular dynamics simulations were obtained by GROMACS version 2016.2[229,230] using the following force fields: For the methanol systems the GROMOS96 54A7 force field[231] and for the water solvated systems we initially also tried GROMOS96 54A7, which was unfortunately providing too compact ensembles, and later on moved to CHARMM36m[232,233] that was optimized for both regular and intrinsically disordered proteins.

Methanol

The structures solvated in methanol have been started from helical and extended conformations in their neutral form. We report only the helical start as the extended one folded into helix after 30-60 ns. The simulation box was set to dodecahedron and defined in such a way that the minimum distance of the structure and the box was at least 2.8 nm and subsequently solvated with methanol.

Following settings have been applied: The Leap frog integrator was utilized together with all bonds being constrained by the LINCS algorithm[234] in order to enable a time-step of 2 fs. Coulomb interactions were calculated by particle mesh Ewald (PME) [235] method with the same cutoff of 1.4 nm as used for Lennard Jones interactions. The neighbor list was updated every 10 steps. Initially all systems were energy minimized with steepest-descent algorithm for 50000 steps. In the next step two consecutive equilibration simulations followed (100 ps each) in a canonical (NVT) and later on isobaric-isothermal (NPT) ensemble were carried out where heavy atoms have been position restrained. The following actual production without position restraints was 2 μs long. The temperature was maintained at 300 K by using the Velocity-rescaling algorithm [236] with a coupling time of 0.1 ps. The bulk water systems were simulated in an isobaric-isothermal ensemble where the pressure was set to 1 atm using isotropic Parrinello-Rahman pressure coupling [237] with a pressure relaxation time of 1 ps for the system.

Water

The systems in water have been prepared similarly but with reduced minimum box distance for the extended structure of 0.8 nm, which cannot expand further. The helical systems were simulated with similar box size. The box was solvated with water and neutralized with sodium chloride.

In case of the GROMOS96 54A7 force field the SPC/E water model[238] was used together with the same settings and simulation scheme as for the methanol system. For the CHARMM36m force field the procedure was similar, just the tip3p water model was used together with a modified cutoff for short-ranged electrostatic and Lenard Jones interactions of 1.2 nm, where a switching function was applied to smoothly approach the cutoff between 1.0 and 1.2 nm.

All peptides have been started from two different conformations, fully extended and helical, resulting in production simulations of following length: For ASYN-P short two 5 μs long simulations. For the longer peptides ASYN-P WT and DM we applied a modified scheme with 2 μs initial simulation length, either extended by further 2 μs or continued for 2 μs with new velocities. Resulting in together 12 μs simulation time for ASYN-P WT and DM respectively.

Cluster analysis

For the P4 peptide in methanol a cluster analysis was performed using the gromos clustering method[239] with a cutoff of 0.45 nm for the root mean square deviation (RMSD) of the α-carbon atoms. The resulting clusters were further analyzed for their label distance distributions in order to describe their contribution to the general picture. Whereas the P5T fragment in water was analyzed for the conformational space covered by a narrow window of inter label distances. The disordered character of this fragment in water is allowing for several conformations describing a single inter label distance. Initially the conformations with an inter label distance between 2.7 and 2.8 nm have been selected from the concatenated trajectories with a helical and extended start and subsequently clustered with the gromos method and a RMSD cutoff of 0.45 nm.

8.1.2. Studies conducted in chapter 5.2

Expression and purification of p38α (carried out by Jörn Weisner)

N-terminally His6-tagged p38α constructs containing a PreScission Protease cleavage site and the mutations required for mono-labeling (C119S/C162S/F327L/A172C) were generated *via* site-directed mutagenesis and cloned into a pOPINF vector. Human p38α MAPK mutant constructs were subsequently transformed into chemically competent BL21 (DE3) *E. coli*, expressed and purified as described previously.[204] Briefly, overexpression was performed at 18 °C overnight (20 hours) while shaking at 160 rpm. Afterwards, the target proteins were purified by Ni-affinity, anion exchange, and size exclusion chromatography. The His6-tag was removed by addition of PreScission Protease prior to anion exchange chromatography. Finally, purified proteins were concentrated to approximately 20 mg/mL, snap frozen in liquid nitrogen and stored at -80 °C until further use.

Site-directed spin labeling of p38α

Spin labeling of p38α: To a 50 μM solution of p38α in labeling buffer (Tris 20 mM, 200 mM NaCl, 5% v/v glycerol, pH 7.4) three equivalents of (1-oxyl-2,2,5,5-tetramethylpyrroline-3-methyl) methanethiosulfonate, (SCBT, 25 mM in DMSO) were added and incubated over-night at 4 °C while shaking gently. The crude product was isolated using Vivaspin 4 centrifugal filters (10 kDa MWCO, Sartorius) for 6-8 times at 4 °C until no free spin label could be detected using cwEPR spectroscopy. The residue was collected in buffer to yield a final con-centration of approx. 300 μM and stored at -80 °C. Labeling efficiency was evaluated using mass spectrometry.

HTRF-based activity measurements (carried out by Jörn Weisner)

Prior to activity measurements, p38α kinase constructs (wild-type, mutant/unlabeled, mutant/labelled) were activated with constitutively active MKK6S207E/T211E (Thermo Scientific, Lot# 877061F) in activation buffer (50 mM Tris, 10 mM MgCl2, 1 mM ATP, 1 mM DTT, 0.001 % Tween 20, pH 7.4) at 37 °C for 90 min with shaking at 400 rpm. The reaction mixtures were subsequently dialyzed overnight at 4 °C against storage buffer (20 mM HEPES, 50 mM NaCl, 5 % glycerol, pH 7.1), concentrated to ~0.2 mg/mL and stored at -80 °C for further use.

Activity-based measurements were carried out using the HTRF® KinEASE™ assay from Cisbio according to the manufacturer's instructions. For determination of ATP Km values, 0.04/3.5/20 ng of activated p38α MAPK constructs (wild-type, mutant/unlabeled, and mutant/labelled, respectively) per well were incubated with varying concentrations of ATP (0.4-900 μM) and 1 μM of GST-ATF2 protein substrate in reaction buffer (50 mM HEPES, 0.1 mM Na3VO4, 0.02 % NaN3, 0.01 % (w/v) BSA, 10 mM MgCl2, 1 mM MnCl2, 1 mM DTT, 0.01 % Triton X-100, pH 7.0) in microtiter plates (Greiner Bio-One, 384 well,

black, flat bottom) for 10/10/20 min. Afterwards, the reaction was stopped by addition of detection solution (50 mM HEPES, 0.1 % (w/v) BSA, 800 mM KF, 20 mM EDTA, 0.666 nM anti-phospho-ATF2-Eu(K) antibody, 100 nM anti-GST-d2 antibody, pH 7.0) and incubation for 60 min at room temperature. Finally, fluorescence was detected at emission wavelengths of 620 nm and 665 nm 60 µs after excitation at 317 nm using an EnVision 2104 plate reader (Perkin Elmer). The acceptor/donor ratios (fl665 nm/fl620 nm) were calculated, plotted versus the ATP concentrations and data were fit to the Michaelis-Menten equation using Origin (OriginLab, Northampton, MA).

Table 2: Determination of ATP Km values for p38α constructs (wild-type, mutant/unlabeled, mutant/labelled) given as mean ± SD (n = 3).

construct	ATP K_m / µM
p38α wild-type	11.0 ± 2.1
p38α mutant/unlabeled	52.3 ± 8.9
p38α mutant/labelled	42.4 ± 7.3

Continuous wave EPR measurements

Spectra were collected at room temperature (293 K) using a Bruker EMX Nano X-Band spectrometer. An aliquot (30 µL) of the protein at concentrations ranging from 50-100 µM was placed in quartz capillaries with an inner diameter of 1 mm. In all cases, the experimental parameters were optimized to yield a high signal-to-noise ratio without distorting the spectral line shape. Quantitative spin counting was carried out using the built-in features of the Bruker Xenon software in addition to the use of spin label stock solutions as a control reference. Spectra normalization was performed by dividing the spectra by the area defined by the double integral.

Temperature dependent measurements were collected using a Magnettech MS 5000 X-Band spectrometer equipped with a TC H04 temperature controller. The temperature was varied between 5°C and 32.5°C and spectra were collected using optimized settings as described above.

Spectral simulations

EPR spectra were analyzed using Matlab R2016a (The MathWorks) using the EasySpin toolbox and the chili function (5.0.16).[72] While varying simulation parameters, the least-square fits were performed. For all simulations, $g = [g_x\ g_y\ g_z] = [2.00906\ 2.00687\ 2.003]$ were chosen and the data was frequency corrected manually to account for uncertainties in the magnetic field measurement.[240]

Spectral simulations of inhibitor dependent measurements

The spectral simulations are based on a two-component model of two spin ½ systems with a nitrogen nucleus. Both components were simulated using an axial hyperfine tensor, isotropic rotation, an orienting potential [199] and a fixed linewidth using an

iterative approach. Using the spectrum of apo p38α with a high content of component S_a and a small portion of component S_B , spectral parameters for S_a including the weighing factor *a* were changed while keeping all parameters for S_B fixed. This optimized system was then used as a fixed component while varying the parameters for B in a spectrum with a high content of the inhibitor-induced conformation. The parameters of the spectral simulation for both components (rotational correlation time, A- and g-tensors and coefficients of the orienting potentials) are given in Table S3.

The spectral fits are deviating from the experimental data beyond the level of noise. Therefore, they contain a significant error. The estimation of this error was done by gradually changing the weighting factors of both components until the deviation of the simulation and experiment was significantly degraded (rmsd increased by 3% from approximately 0.048) . The error estimation was also accounted for in the temperature dependent measurements using error propagation.

Table 3: Parameters used for spectral simulations.

	t_{rot} [ns][a]	$A_{xx}=A_{yy}$ [MHz]	A_{zz} [MHz]	linewidth [mT]	g= [g_x g_y g_z]	Orienting potential coefficients $\lambda_{2,0}, \lambda_{2,2}, \lambda_{4,0}, \lambda_{4,2}, \lambda_{4,4}$ [kT]
S_A	5.5	13	101.38	0.11	[2.00906 2.00687 2.003]	1.04, 1.46, 0.90, -3.94, -2.43
S_B	0.97	13	111.01	0.11	[2.00906 2.00687 2.003]	0.14, 1.37, -3.96, 0, 0

Spectral simulations of temperature dependent measurements

In order to facilitate data analysis of a large series of experimental data by drastically reducing the computational effort, a simplified simulation approach was applied. Allowing for anisotropic rotation and without an orienting potential, describing the experiment with a slightly reduced quality (see Figure 33) is feasible. However, the spectral component weights required for data interpretation obtained by the simplified simulation approach are similar to those obtained by the full model. Thus, the simplified simulation approach was used for the spectral analysis of the temperature dependent datasets. In order to account for viscosity changes of the solvent for different temperatures, the effective changes on the spin label's rotational correlation time was estimated according to Cheng (2008).[241] Therefore, a change of $\Delta \log T_{corr} = 0.2$ was allowed during spectral simulations.

Table 4: Parameters used for temperature series.

	t_{rot} [ns][a]	$A_{xx}=A_{yy}$ [MHz]	A_{zz} [MHz]	linewidth [mT]	g= [g_x g_y g_z]
S_A	see Table S4-S11	13	100.13	0.11	[2.00906 2.00687 2.003]
S_B	see Table S4-S11	15.67	99.56	0.11	[2.00906 2.00687 2.003]

[a] Anisotropic rotational diffusion was assumed for S_B while simulations for S_A are based on isotropic rotational diffusion.

8.1.3. Studies conducted in chapter 5.3

Expression and purification of p38α (carried out by Jörn Weisner)

N-terminally His6-tagged p38α constructs containing a PreScission Protease cleavage site and the mutations required for double-labeling were generated *via* site-directed mutagenesis and cloned into a pOPINF vector. Human p38α MAPK mutant constructs were subsequently transformed into chemically competent BL21 (DE3) *E. coli*, expressed and purified as described previously.[204] Briefly, overexpression was performed at 18 °C overnight (20 hours) while shaking at 160 rpm. Afterwards, the target proteins were purified by Ni-affinity, anion exchange, and size exclusion chromatography. The His6-tag was removed by addition of PreScission Protease prior to anion exchange chromatography. Finally, purified proteins were concentrated to approximately 20 mg/mL, snap frozen in liquid nitrogen and stored at -80 °C until further use.

Spin labeling of p38α

Spin labeling of p38α: To a 50 μM solution of p38α in labeling buffer (Tris 20 mM, 200 mM NaCl, 5% v/v glycerol, pH 7.4) three equivalents of (1-oxyl-2,2,5,5-tetramethylpyrroline-3-methyl) methanethiosulfonate, (SCBT, 25 mM in DMSO) were added and incubated over-night at 4 °C while shaking gently. The crude product was isolated using Vivaspin 4 centrifugal filters (10 kDa MWCO, Sartorius) for 6-8 times at 4 °C until only minor fractions of free spin label (less than 1 % of the expected protein concentration) could be detected using cwEPR spectroscopy. The residue was collected in buffer to yield a final concentration of approx. 300 μM and stored at -80 °C.

Pulsed EPR Experiments

Pulsed experiments were performed either on a Bruker Elexsys E580 Q-band spectrometer using a Bruker EN 5107D2 resonator equipped with a 15 W solid state microwave amplifier and a helium gas flow system (CF935, Oxford Instruments) or a QT-II resonator equipped with a 150 W TWT and a cryogen-free system. The sample volume was 10 μL for the EN 5107D2 resonator and 60 μL for the QT-II resonator. Samples were snap frozen in liquid nitrogen and inserted into the resonator. The temperature was fixed to 50 K.

Distance measurements were carried out using a two dimensional 4-pulse DEER experiment.[242] The shot repetition time was optimized to prevent saturation of longitudinal relaxation of the nitroxide labels. Pump and observer pulse lengths were optimized for every sample and range between 20 and 28 ns for the pump and 24 to 30 ns for the observer pulses. The magnetic field was set to the maximum of the nitroxide spectrum and the observer pulse frequency was set to 50.4 MHz lower than the pump pulse frequency. Nuclear modulation averaging was used to suppress nuclear

modulation artefacts. Accumulation times largely depended on the resonator used and the sample quality and typically ranged between 4 to 20 hours. The dipolar evolution time was optimized for each sample to yield reliable distance information while retaining a high signal-to-noise ratio.

DEER distance distribution analysis

The two dimensional raw DEER data was phase corrected for every slice, averaged and then further processed using Matlab 2017a and DeerAnalysis2016. The zero time and the background start was determined using the built-in optimization function, the end of the DEER curve was cut manually to remove artefacts in the trace. The distance distribution was extracted using a three-dimensional background and Tikhonov-regularization. While the α parameter was typically determined automatically using the L curve criterion, in some cases a slightly larger α parameter was chosen to prevent over sharpening of the distance distribution.

Multilateration

3D modelling of the spin label distribution was carried out using the MMM 2017.2 package.[66] The distance constraints from the preceding analysis were approximated using a single Gaussian distribution profile and the parameters used as an input file for MMM. The crystal structures mentioned in the text were specifically chosen to include coordinates for the label position 172 and thus allow for a label position prediction. Each trilateration was carried out using five different distances to improve the reliability of the probability volume. For the visualization a probability volume showing 50 percent of the total probability was chosen which is a standard value used in crystallographic studies.[66]

9. Appendix

9.1. Appendix for chapter 4

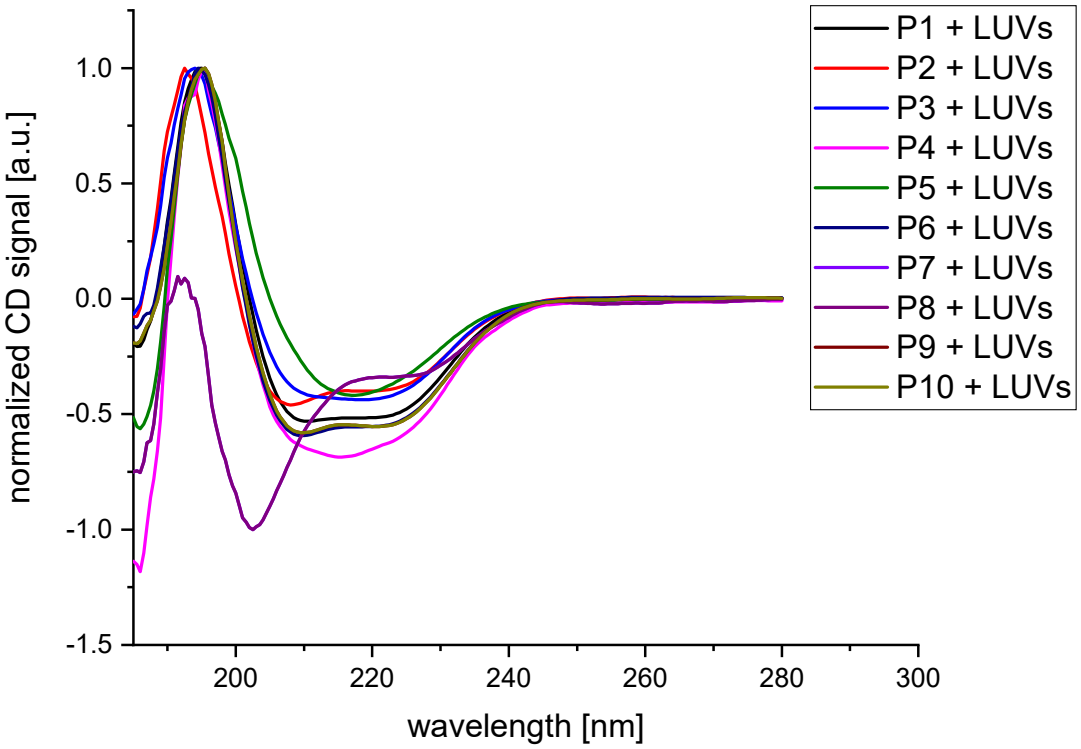

Figure A. 1: CD spectra obtained for all ten peptides upon incubation with 100 nm diameter LUVs (POPG, see chapter 8.1.1 for details. All peptides, with the exception of P8, show distinct tendency towards helical structuring.

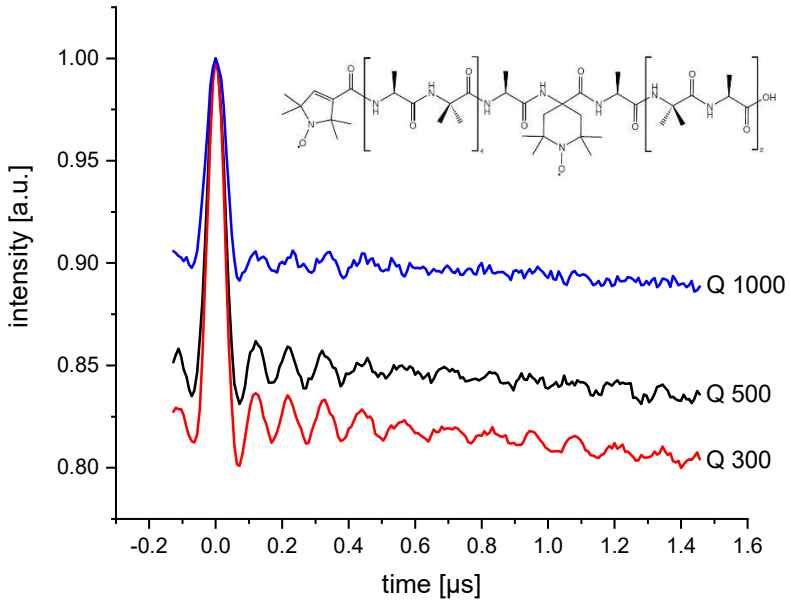

Figure A. 2: Effect of the resonator coupling to the data quality. Three different coupling states (as depicted by the quality factors Q) were adjusted to measure the distance distribution in a model compound bearing two nitroxide moieties in deuterated methanol (shown at the top). Due to bandwidth changes, the pulse lengths varied in all experiments, leading to significant changes in the modulation depths. Pulse lengths were set to 20/30, 18/32 and 12/44 for the pump/observer pulses in the order of Q 300, 500 and 1000. The frequency offset between pulsed was optimized in each case, leading to 44 to 50 MHz offset. The expected distance of the model compound is 2 nm. For the given experimental setup, a low Q factor results in maximum modulation depths while retaining a low noise ration. While for shorter pump pulses a higher excitation and subsequently increased modulation depth is expected, the limited resonator bandwidth restricts the maximum achievable frequency offset. This leads to frequency overlap between pump and observer pulses that diminishes the modulation depth.

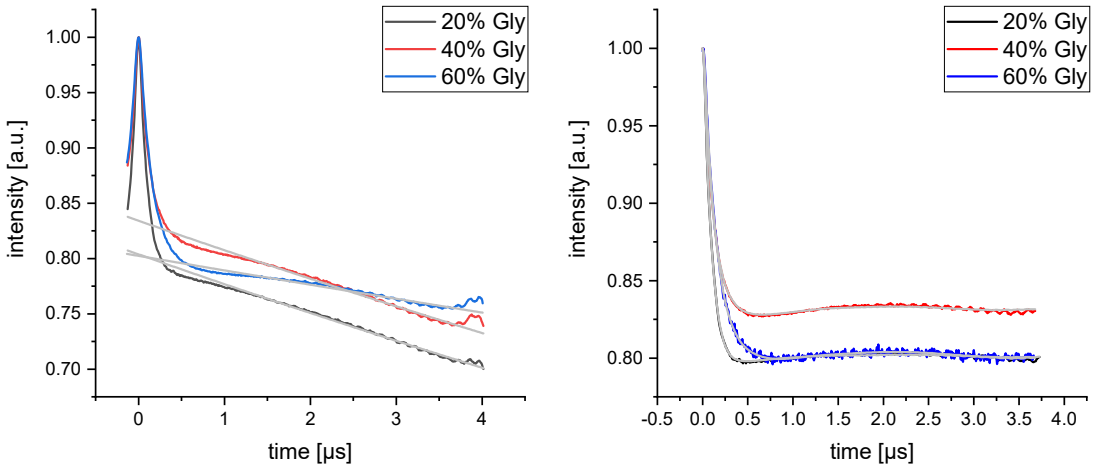

Figure A. 3: Left: Raw data traces obtained for ASYN-P short with varying amounts of glycerol with the corresponding background fits (grey). Right: Form factors resulted after background correction and the corresponding fits from Tikhonov regularization (grey).

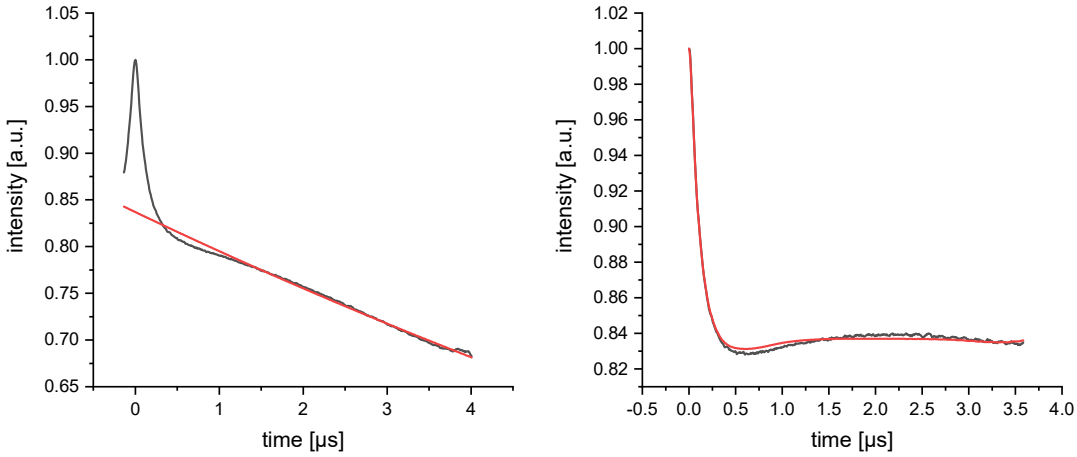

Figure A. 4: Left: Raw data trace (black) obtained for ASYN-P short after freezing with cold isopentane with the corresponding background fit (red). Right: Form factor after background correction (black) and the corresponding fit from Tikhonov regularization (red).

9.2. Appendix for chapter 5.2

Concentration dependencies of inhibitor assays

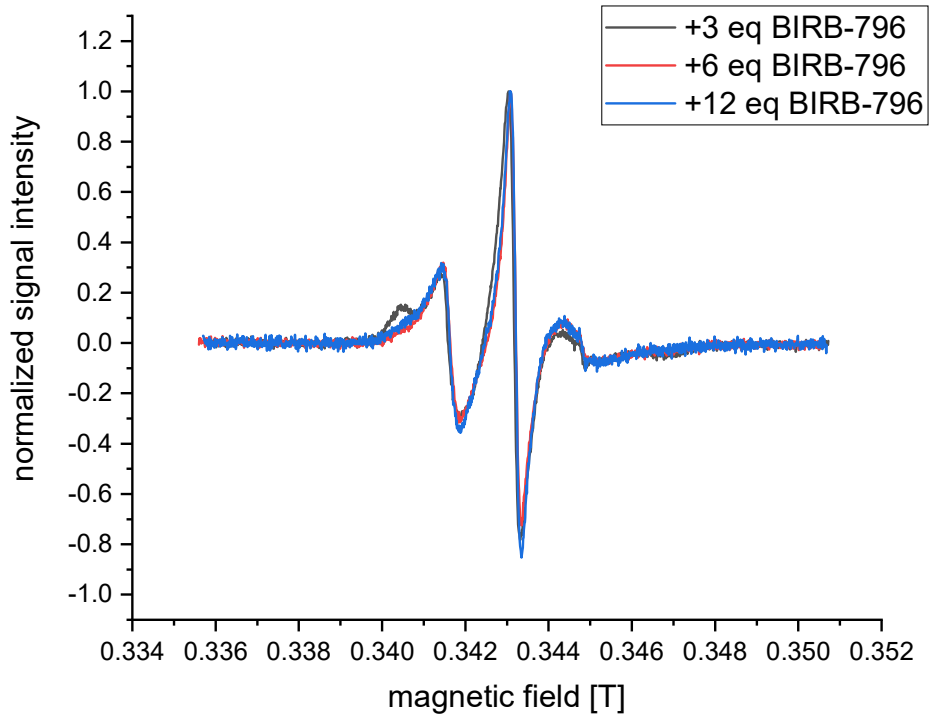

Figure A. 5: Normalized EPR spectrum of p38α and after the addition of 3, 6 or 12 molar equivalents of BIRB-796. A significant change in the spectra is observable, especially between 3 and 6 equivalents.

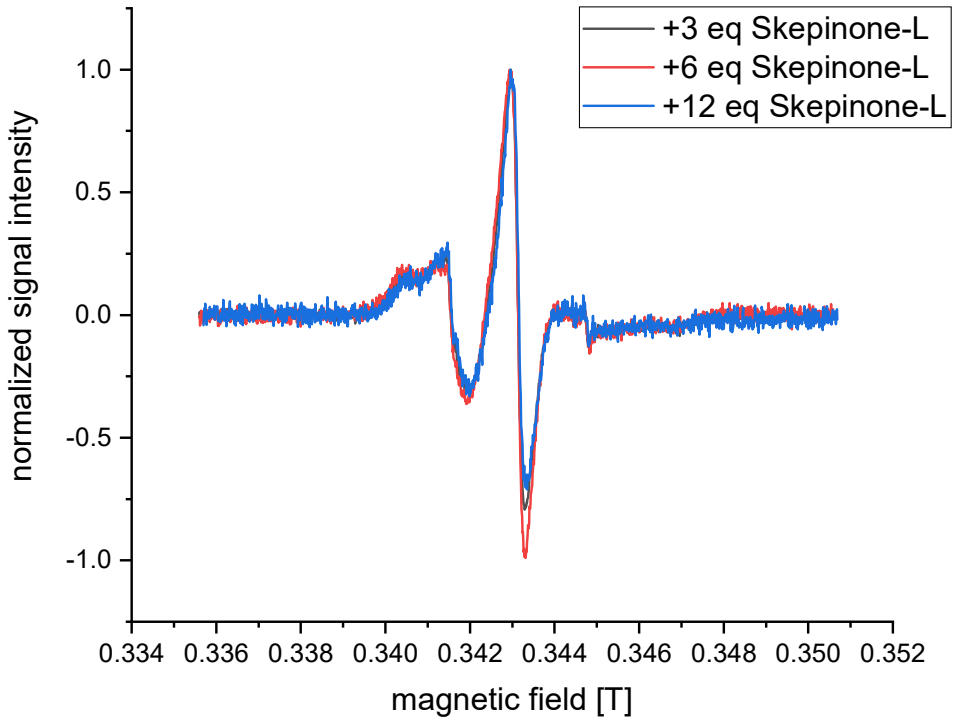

Figure A. 6: Normalized EPR spectrum of p38α and after the addition of 3, 6 or 12 molar equivalents of Skepinone-L.

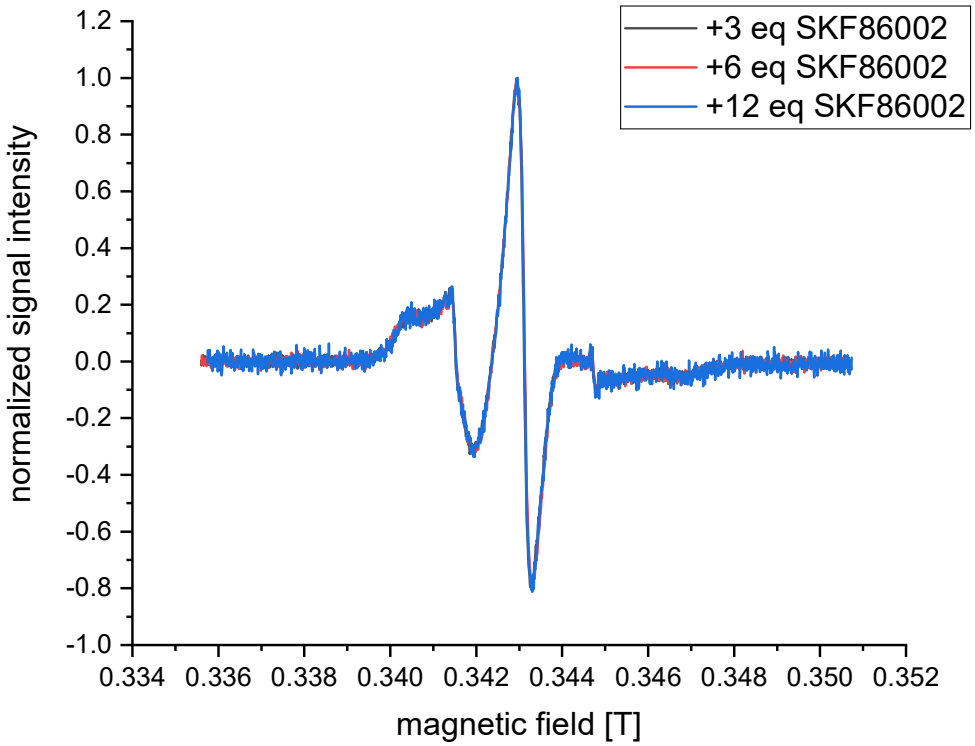

Figure A. 7: Normalized EPR spectrum of p38α and after the addition of 3, 6 or 12 molar equivalents of SKF-86002.

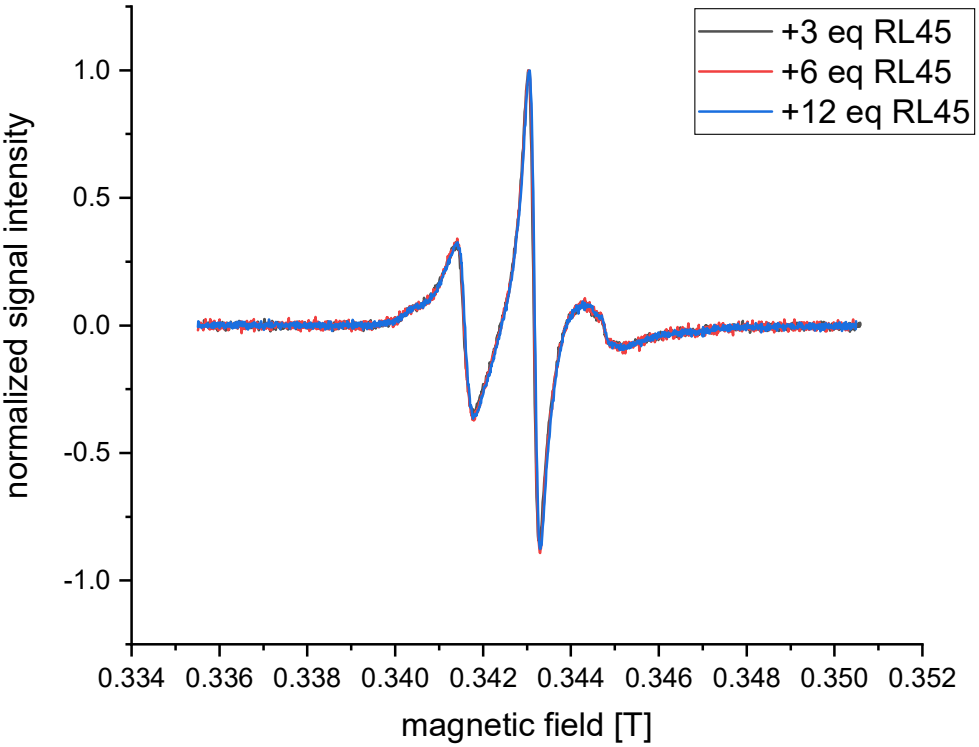

Figure A. 8: Normalized EPR spectrum of p38α and after the addition of 3, 6 or 12 molar equivalents of RL45.

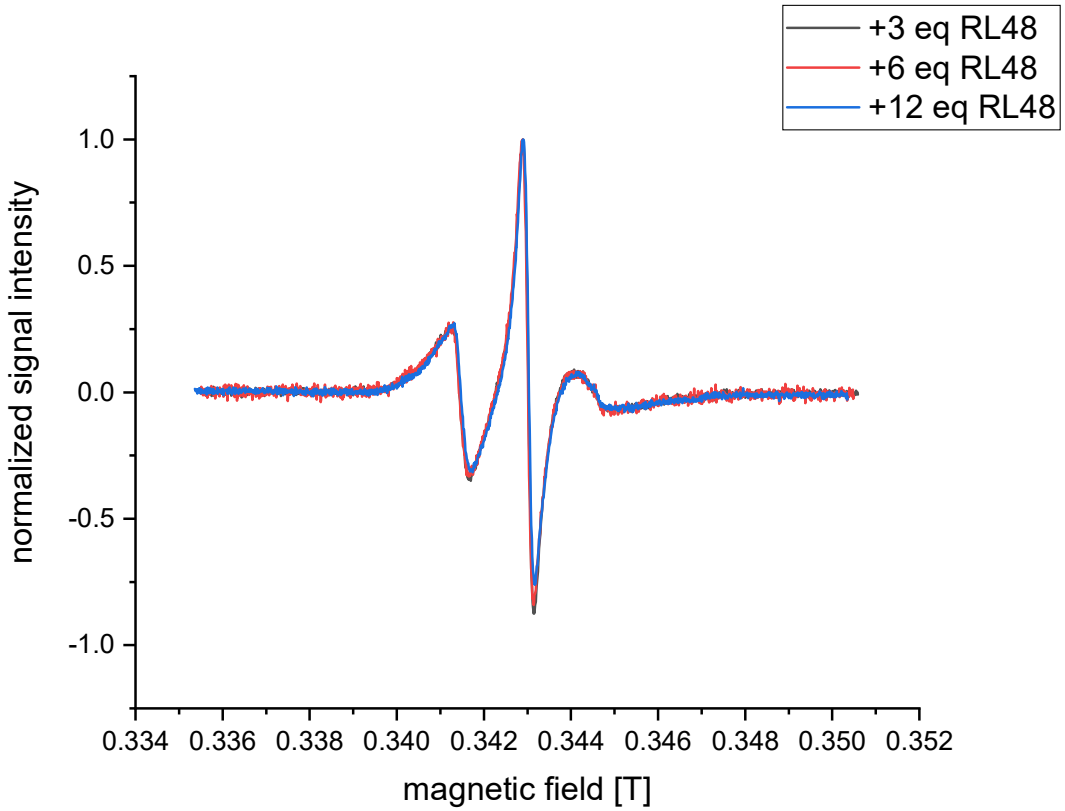

Figure A. 9: Normalized EPR spectrum of p38α and after the addition of 3, 6 or 12 molar equivalents of RL48.

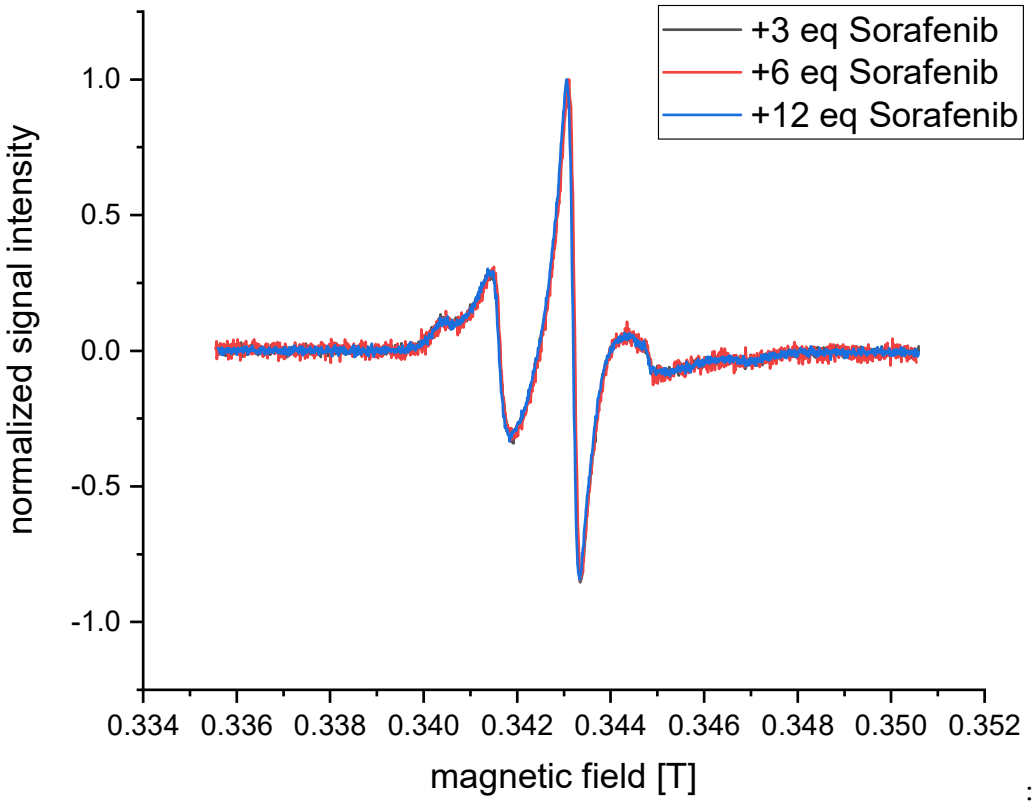

Figure A. 10: Normalized EPR spectrum of p38α and after the addition of 3, 6 or 12 molar equivalents of Sorafenib.

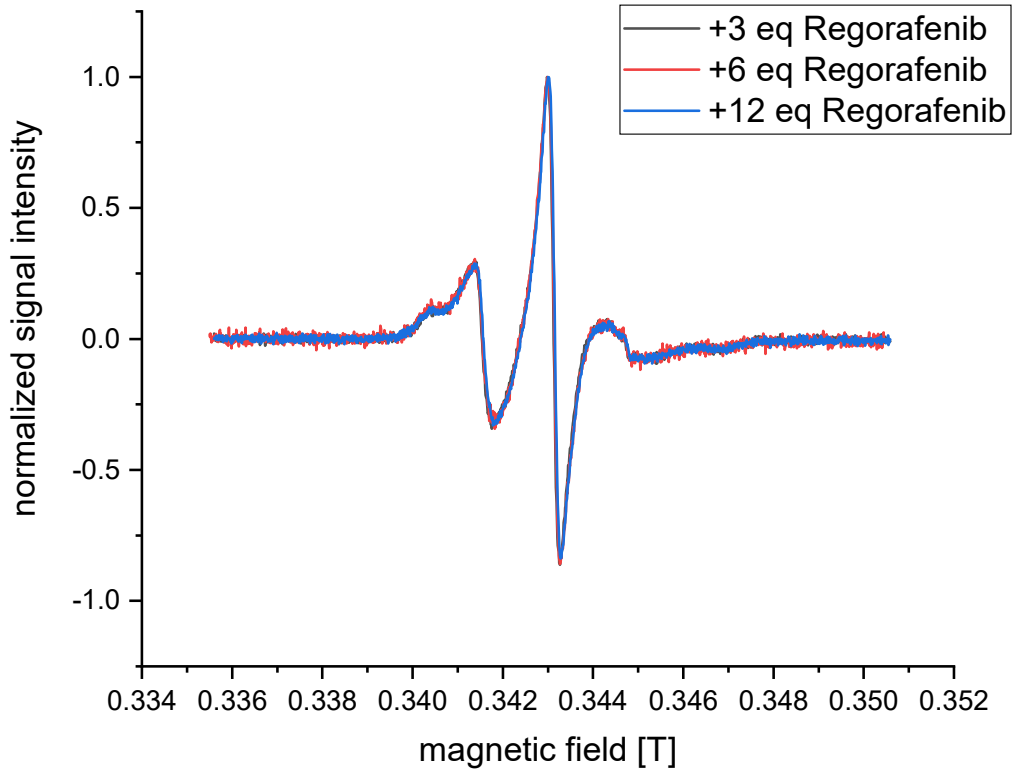

Figure A. 11: Normalized EPR spectrum of p38α and after the addition of 3, 6 or 12 molar equivalents of Regorafenib.

Temperature dependent EPR spectra and Van 't Hoff plots

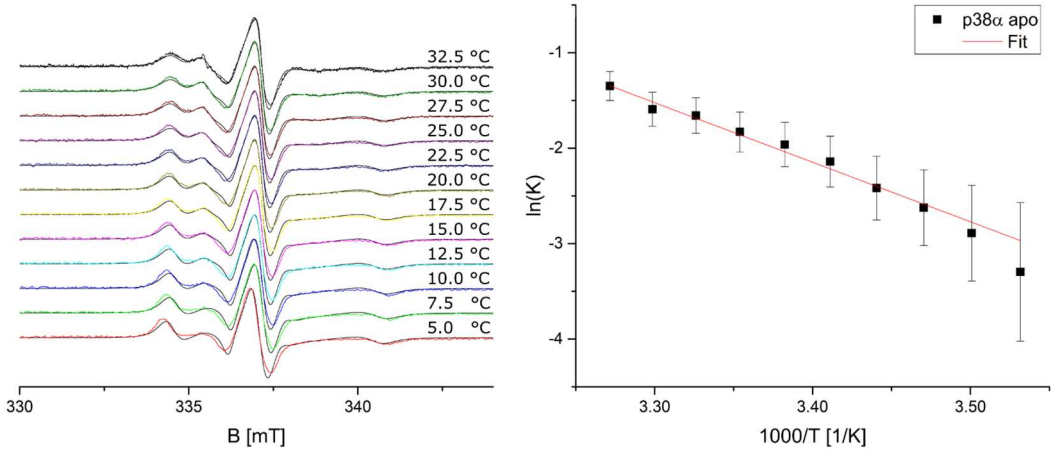

Figure A. 12: Left: Temperature dependent EPR Spectra of p38α (88 µM) with corresponding spectral simulations (black). Right: Van 't Hoff plots for the reaction constant in dependency of the inverse temperature.

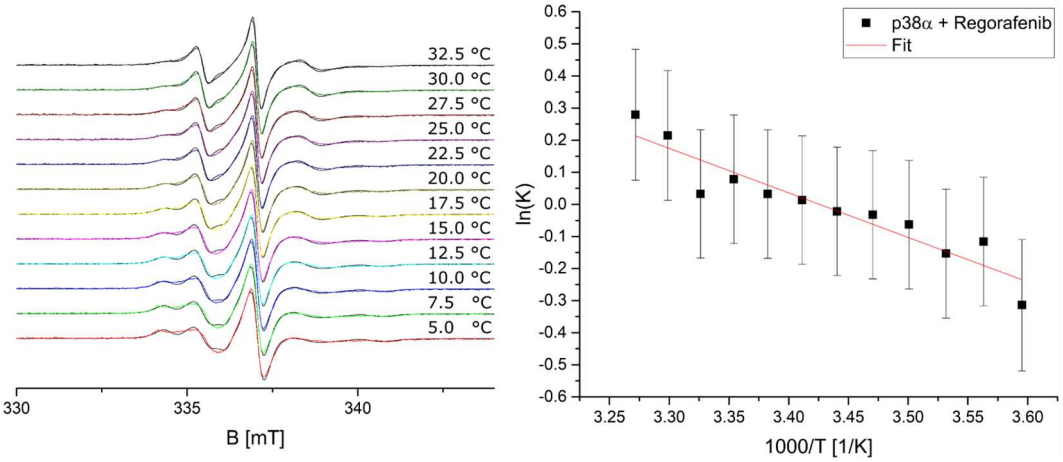

Figure A. 13: Left: Temperature dependent EPR Spectra of p38α (88 µM) after addition of 6 molar equivalents of Regorafenib with corresponding spectral simulations (black). Right: Van 't Hoff plots for the reaction constant in dependency of the inverse temperature.

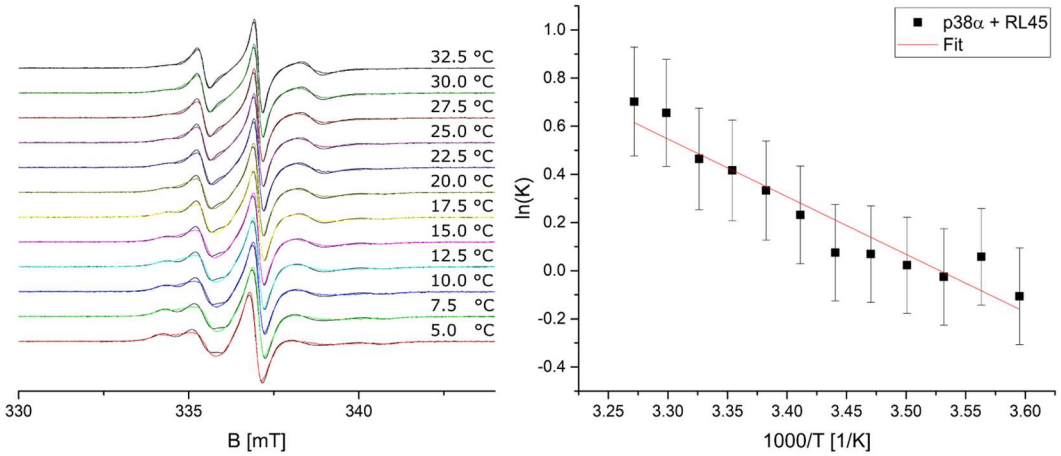

Figure A. 14: Left: Temperature dependent EPR Spectra of p38α (88 µM) after addition of 6 molar equivalents of RL45 with corresponding spectral simulations (black). Right: Van 't Hoff plots for the reaction constant in dependency of the inverse temperature.

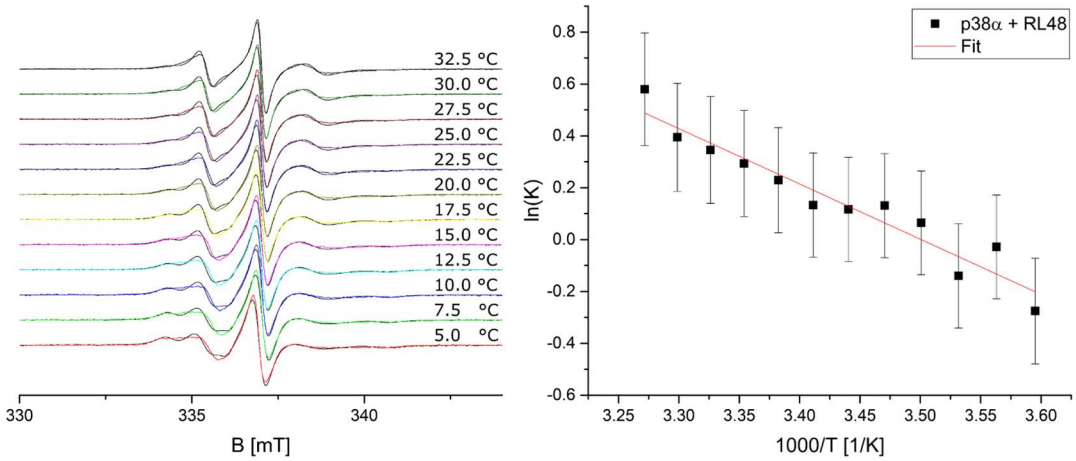

Figure A. 15: Left: Temperature dependent EPR Spectra of p38α (88 µM) after addition of 6 molar equivalents of RL48 with corresponding spectral simulations (black). Right: Van 't Hoff plots for the reaction constant in dependency of the inverse temperature.

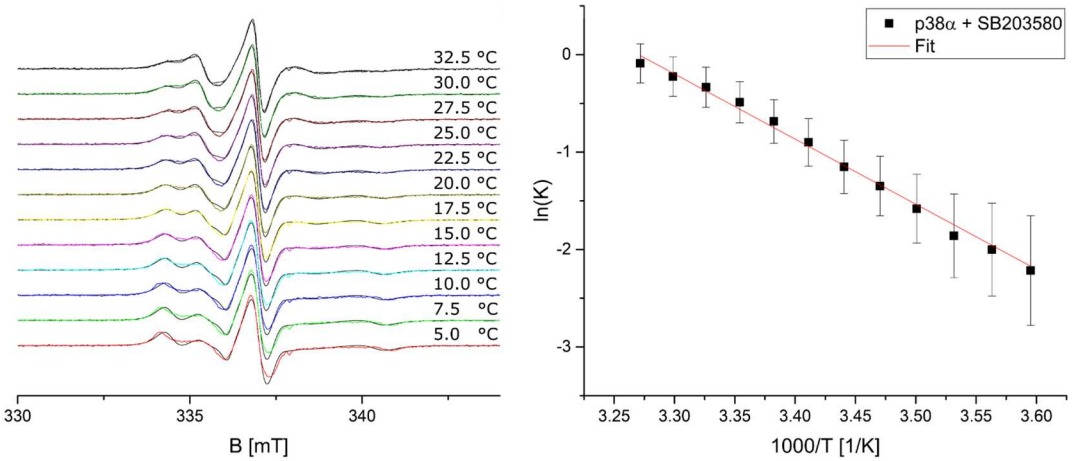

Figure A. 16: Left: Temperature dependent EPR Spectra of p38α (88 µM) after addition of 6 molar equivalents of SB203580 with corresponding spectral simulations (black). Right: Van 't Hoff plots for the reaction constant in dependency of the inverse temperature.

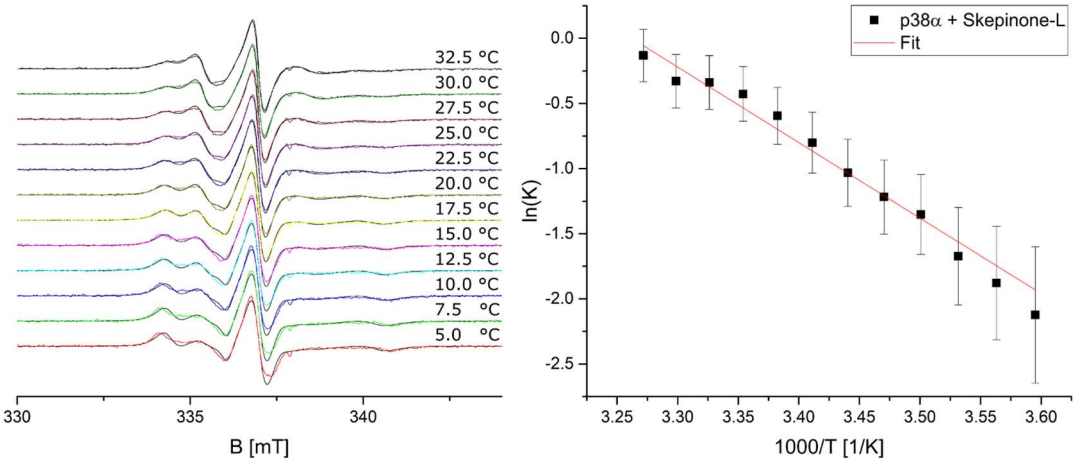

Figure A. 17: Left: Temperature dependent EPR Spectra of p38α (88 µM) after addition of 6 molar equivalents of Skepinone-L with corresponding spectral simulations (black). Right: Van 't Hoff plots for the reaction constant in dependency of the inverse temperature.

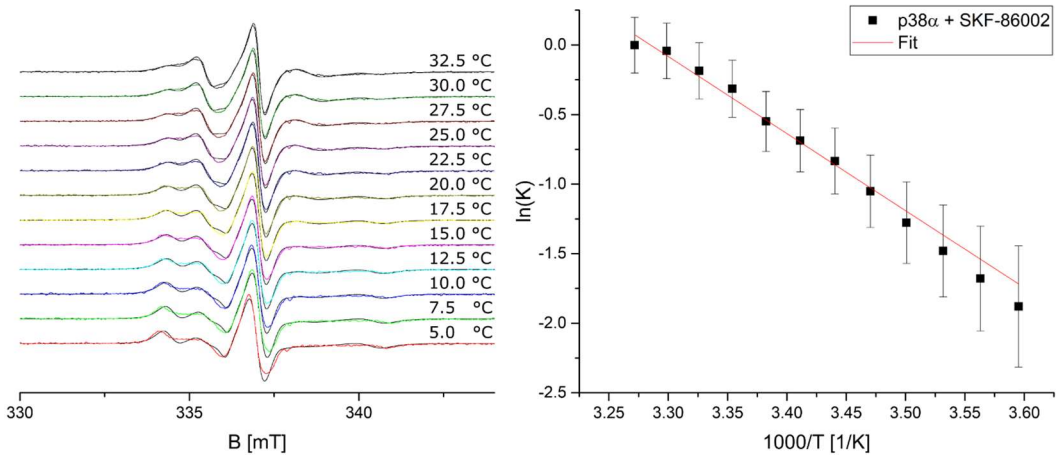

Figure A. 18: Left: Temperature dependent EPR Spectra of p38α (88 µM) after addition of 6 molar equivalents of SKF-86002 with corresponding spectral simulations (black). Right: Van 't Hoff plots for the reaction constant in dependency of the inverse temperature.

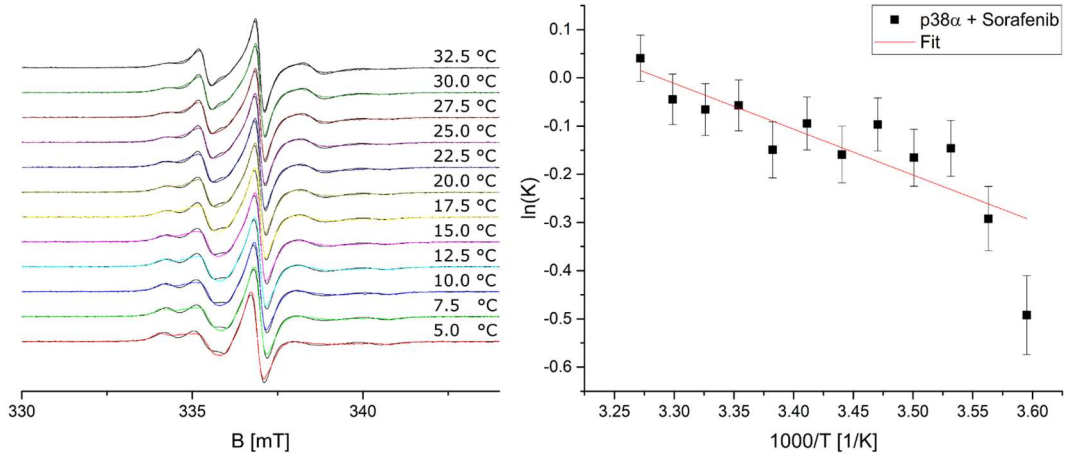

Figure A. 19: Left: Temperature dependent EPR Spectra of p38α (88 µM) after addition of 6 molar equivalents of Sorafenib with corresponding spectral simulations (black). Right: Van 't Hoff plots for the reaction constant in dependency of the inverse temperature.

Simulation parameters for temperature-dependent measurements

Shown below are the experimental parameters used for the temperature-dependent measurements. All the rotational correlation times have been divided by 1 second and are shown as the negative common logarithm.

Table A. 1: Rotational correlation times used for simulation of p38α without inhibitor.

Temperature	$-\log(t_{rot})$, S_A	$-\log(t_{rot,1})$, S_B	$-\log(t_{rot,2})$, S_B	$-\log(t_{rot,3})$, S_B
5.0 °C	-7.9540	-7.362	-9.1121	-8.4947
7.5 °C	-7.9964	-7.113	-9.3534	-8.4462
10.0 °C	-7.9967	-7.113	-9.0381	-8.845
12.5 °C	-7.9933	-7.3452	-9.0381	-8.845
15 °C	-8.0082	-7.113	-9.0381	-8.845
17.5 °C	-8.0220	-7.363	-9.0381	-8.845
20.0 °C	-8.0104	-7.113	-9.0381	-8.8316
22.5 °C	-8.0305	-7.4526	-9.0381	-8.8141
25.0 °C	-8.0613	-7.113	-9.0381	-8.845
27.5 °C	-8.0569	-7.2528	-9.0381	-8.845
30.0 °C	-8.0707	-7.5045	-9.0381	-8.845
32.5 °C	-8.0714	-7.113	-9.0381	-8.8033

Table A. 2: Rotational correlation times used for simulation of p38α after addition of 6 molar equivalents of SB203580.

Temperature	$-\log(t_{rot})$, S_A	$-\log(t_{rot,1})$, S_B	$-\log(t_{rot,2})$, S_B	$-\log(t_{rot,3})$, S_B
5.0 °C	-7.9714	-7.1593	-9.0381	-8.7598
7.5 °C	-7.9796	-7.113	-9.0381	-8.7804
10.0 °C	-8.0197	-7.4597	-9.0381	-8.7221
12.5 °C	-8.0170	-7.113	-9.0381	-8.7662
15 °C	-8.0502	-7.113	-9.0381	-8.7297
17.5 °C	-8.0750	-7.113	-9.0381	-8.7394
20.0 °C	-8.0526	-7.2931	-9.0381	-8.7335
22.5 °C	-8.0601	-7.1293	-9.0386	-8.7308
25.0 °C	-8.0639	-7.113	-9.0381	-8.7402
27.5 °C	-8.0776	-7.1284	-9.0399	-8.7631
30.0 °C	-8.0772	-7.3789	-9.0384	-8.8098
32.5 °C	-8.0823	-7.283	-9.0683	-8.7726

Table A. 3: Rotational correlation times used for simulation of p38α after addition of 6 molar equivalents of Skepinone-L.

Temperature	$-\log(t_{rot})$, S_A	$-\log(t_{rot,1})$, S_B	$-\log(t_{rot,2})$, S_B	$-\log(t_{rot,3})$, S_B
5.0 °C	-7.9556	-7.113	-9.0383	-8.716
7.5 °C	-7.9860	-7.113	-9.0381	-8.7024
10.0 °C	-8.0042	-7.113	-9.0381	-8.7775
12.5 °C	-7.9981	-7.113	-9.0381	-8.7453
15 °C	-8.0251	-7.492	-9.0381	-8.6938
17.5 °C	-8.0445	-7.1546	-9.0381	-8.7672
20.0 °C	-8.0292	-7.1464	-9.0381	-8.7637
22.5 °C	-8.0367	-7.4262	-9.0381	-8.7125
25.0 °C	-8.0413	-7.2034	-9.0489	-8.7435
27.5 °C	-8.0587	-7.113	-9.0755	-8.7517
30.0 °C	-8.0823	-7.113	-9.1209	-8.7545
32.5 °C	-8.0748	-7.113	-9.0934	-8.7785

Table A. 4: Rotational correlation times used for simulation of p38α after addition of 6 molar equivalents of SKF-86002.

Temperature	$-\log(t_{rot})$, S_A	$-\log(t_{rot,1})$, S_B	$-\log(t_{rot,2})$, S_B	$-\log(t_{rot,3})$, S_B
5.0 °C	-7.9518	-7.1667	-9.0381	-8.6949
7.5 °C	-7.9571	-7.113	-9.0381	-8.7794
10.0 °C	-7.9920	-7.113	-9.0381	-8.6857
12.5 °C	-8.0197	-7.1135	-9.0381	-8.7362
15 °C	-8.0212	-7.1556	-9.0381	-8.7104
17.5 °C	-8.0178	-7.113	-9.0381	-8.7316
20.0 °C	-8.0393	-7.2531	-9.0381	-8.7211
22.5 °C	-8.0696	-7.4924	-9.0381	-8.7114
25.0 °C	-8.0713	-7.3278	-9.0392	-8.7385
27.5 °C	-8.0596	-7.113	-9.0637	-8.7533
30.0 °C	-8.0639	-7.113	-9.0685	-8.7689
32.5 °C	-8.0823	-7.113	-9.1079	-8.7686

Table A. 5: Rotational correlation times used for simulation of p38α after addition of 6 molar equivalents of RL45.

Temperature	-log(t_{rot}), S_A	-log($t_{rot,1}$), S_B	-log($t_{rot,2}$), S_B	-log($t_{rot,3}$), S_B
5.0 °C	-7.9671	-7.113	-9.0381	-8.6921
7.5 °C	-7.9541	-7.113	-9.0463	-8.7001
10.0 °C	-8.0161	-7.2917	-9.1017	-8.6954
12.5 °C	-8.0449	-7.3314	-9.1356	-8.6953
15 °C	-8.0479	-7.113	-9.1687	-8.7131
17.5 °C	-8.0816	-7.113	-9.2026	-8.724
20.0 °C	-8.0823	-7.113	-9.2098	-8.7357
22.5 °C	-8.0823	-7.113	-9.2386	-8.7391
25.0 °C	-8.0823	-7.113	-9.2599	-8.7549
27.5 °C	-8.0823	-7.113	-9.2739	-8.7976
30.0 °C	-8.0823	-7.113	-9.2948	-8.7747
32.5 °C	-8.0823	-7.113	-9.3208	-8.7913

Table A. 6: Rotational correlation times used for simulation of p38α after addition of 6 molar equivalents of RL48.

Temperature	-log(t_{rot}), S_A	-log($t_{rot,1}$), S_B	-log($t_{rot,2}$), S_B	-log($t_{rot,3}$), S_B
5.0 °C	-7.9828	-7.113	-9.056	-8.6689
7.5 °C	-7.9634	-7.113	-9.0383	-8.6824
10.0 °C	-8.0030	-7.113	-9.0874	-8.7154
12.5 °C	-8.0113	-7.113	-9.091	-8.714
15 °C	-8.0083	-7.1863	-9.1071	-8.7103
17.5 °C	-8.0499	-7.113	-9.1544	-8.7272
20.0 °C	-8.0549	-7.113	-9.1849	-8.7418
22.5 °C	-8.0793	-7.113	-9.2099	-8.7387
25.0 °C	-8.0823	-7.3149	-9.2238	-8.7449
27.5 °C	-8.0823	-7.4481	-9.2368	-8.7505
30.0 °C	-8.0823	-7.3819	-9.2642	-8.7328
32.5 °C	-8.0622	-7.3795	-9.2721	-8.7454

Table A. 7: Rotational correlation times used for simulation of p38α after addition of 6 molar equivalents of Sorafenib.

Temperature	-log(t_{rot}), S_A	-log($t_{rot,1}$), S_B	-log($t_{rot,2}$), S_B	-log($t_{rot,3}$), S_B
5.0 °C	-7.9665	-7.304	-9.0381	-8.6944
7.5 °C	-7.9447	-7.1915	-9.0381	-8.7217
10.0 °C	-7.9434	-7.1477	-9.039	-8.7277
12.5 °C	-7.9743	-7.299	-9.0761	-8.7321
15 °C	-7.9909	-7.113	-9.0992	-8.7337
17.5 °C	-8.0139	-7.113	-9.141	-8.7453
20.0 °C	-8.0233	-7.161	-9.1593	-8.7474
22.5 °C	-8.0497	-7.3626	-9.194	-8.7438
25.0 °C	-8.0656	-7.113	-9.2071	-8.7946
27.5 °C	-8.0823	-7.113	-9.2441	-8.779
30.0 °C	-8.0823	-7.4506	-9.2646	-8.7739
32.5 °C	-8.0823	-7.1144	-9.2858	-8.8078

Table A. 8: Rotational correlation times used for simulation of p38α after addition of 6 molar equivalents of Regorafenib.

Temperature	-log(t_{rot}), S_A	-log($t_{rot,1}$), S_B	-log($t_{rot,2}$), S_B	-log($t_{rot,3}$), S_B
5.0 °C	-7.9544	-7.304	-9.0381	-8.6806
7.5 °C	-7.9514	-7.113	-9.0381	-8.7059
10.0 °C	-7.9709	-7.113	-9.0696	-8.7213
12.5 °C	-7.9852	-7.2439	-9.0987	-8.7141
15 °C	-7.9976	-7.113	-9.1236	-8.7212
17.5 °C	-8.0411	-7.113	-9.1588	-8.738
20.0 °C	-8.0369	-7.113	-9.1741	-8.7413
22.5 °C	-8.0622	-7.3781	-9.2057	-8.7468
25.0 °C	-8.0823	-7.113	-9.2322	-8.764
27.5 °C	-8.0823	-7.113	-9.2597	-8.7691
30.0 °C	-8.0823	-7.113	-9.2721	-8.7917
32.5 °C	-8.0823	-7.2632	-9.2867	-8.7962

9.3. Appendix for chapter 5.3

DEER data obtained for p38α double mutants in absence and presence of inhibitors

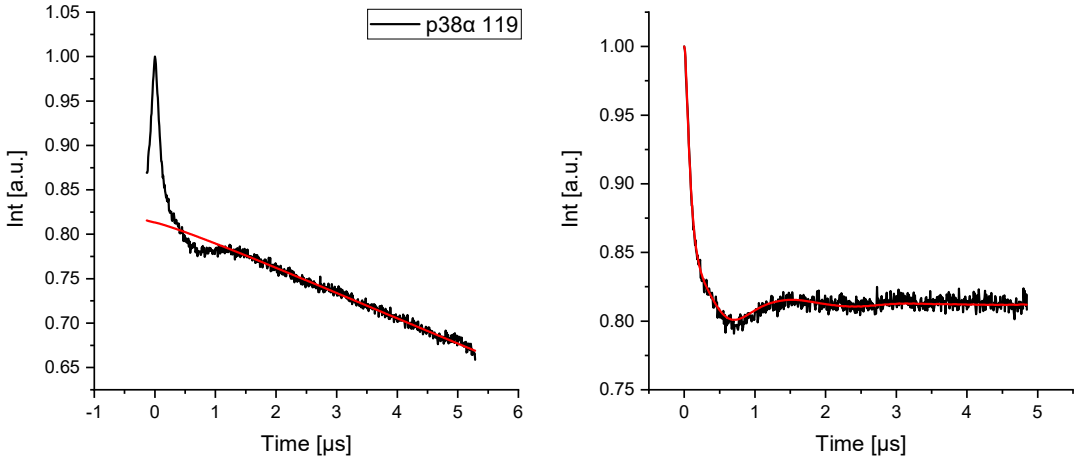

Figure A. 20: Left: Raw DEER data trace obtained for p38α 119 (black) and the corresponding background fit (red). Right: Form factor (black) and the fit obtained by Tikhonov regularization (red). Artifacts at the end of the traces were cut manually in all DEER measurements.

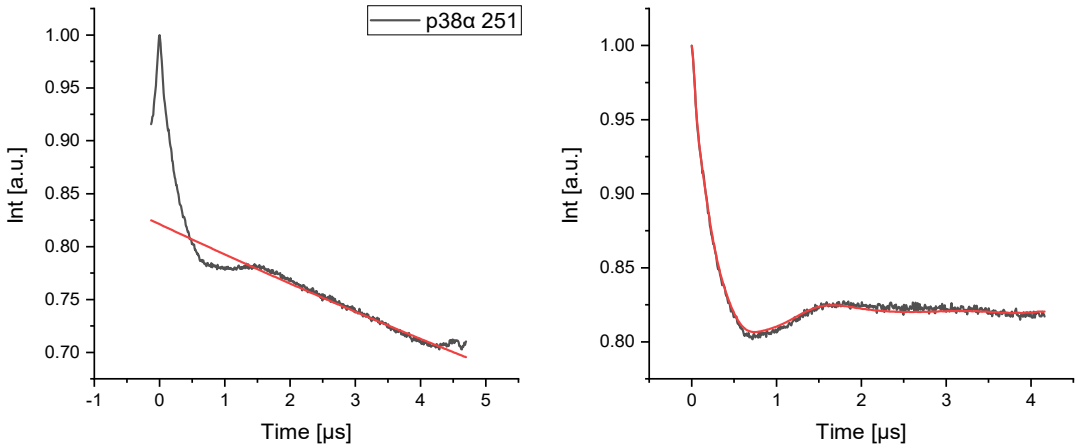

Figure A. 21: Left: Raw DEER data trace obtained for p38α 251 (black) and the corresponding background fit (red). Right: Form factor (black) and the fit obtained by Tikhonov regularization (red)

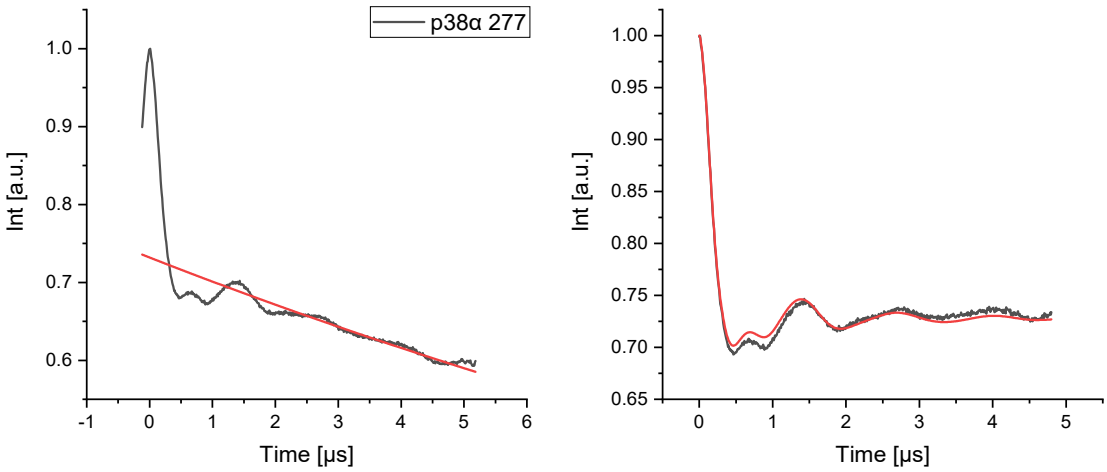

Figure A. 22: Left: Raw DEER data trace obtained for p38α 277 (black) and the corresponding background fit (red). Right: Form factor (black) and the fit obtained by Tikhonov regularization (red)

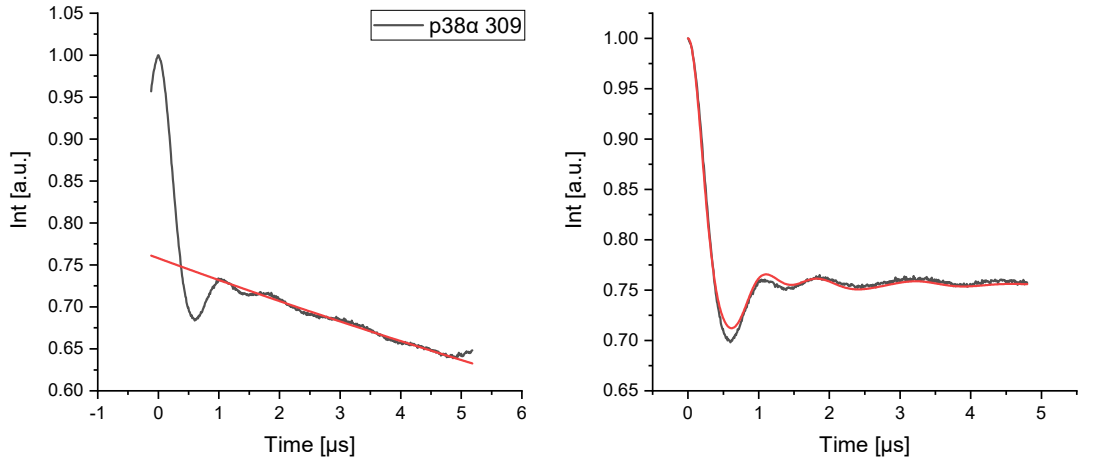

Figure A. 23: Left: Raw DEER data trace obtained for p38α 309 (black) and the corresponding background fit (red). Right: Form factor (black) and the fit obtained by Tikhonov regularization (red)

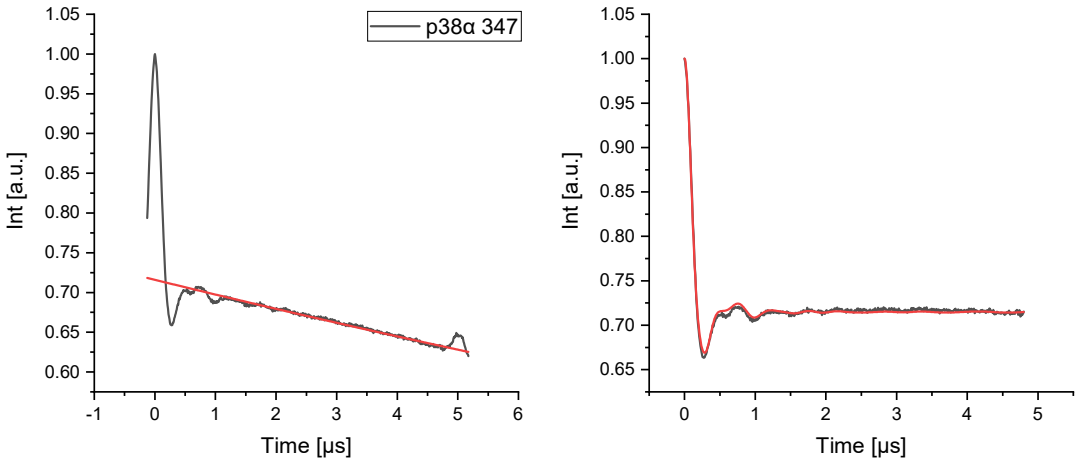

Figure A. 24: Left: Raw DEER data trace obtained for p38α 347 (black) and the corresponding background fit (red). Right: Form factor (black) and the fit obtained by Tikhonov regularization (red)

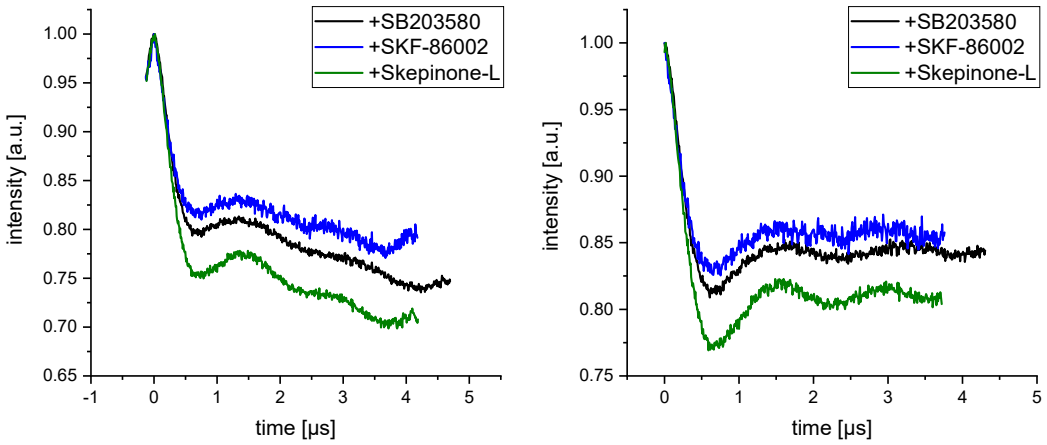

Figure A. 25: Measurements with p38α 119 in the presence of inhibitors. Left: Raw DEER data traces obtained for p38α 119 with the three type I inhibitors. Right: Form factors obtained for the DEER traces.

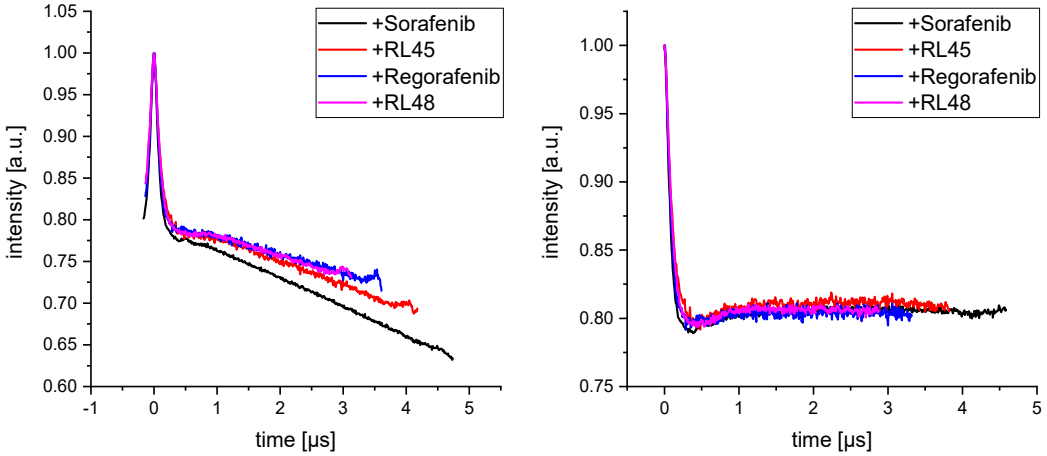

Figure A. 26: Measurements with p38α 119 in the presence of inhibitors . Left: Raw DEER data traces obtained for p38α 119 with the four type II inhibitors. Right: Form factors obtained for the DEER traces.

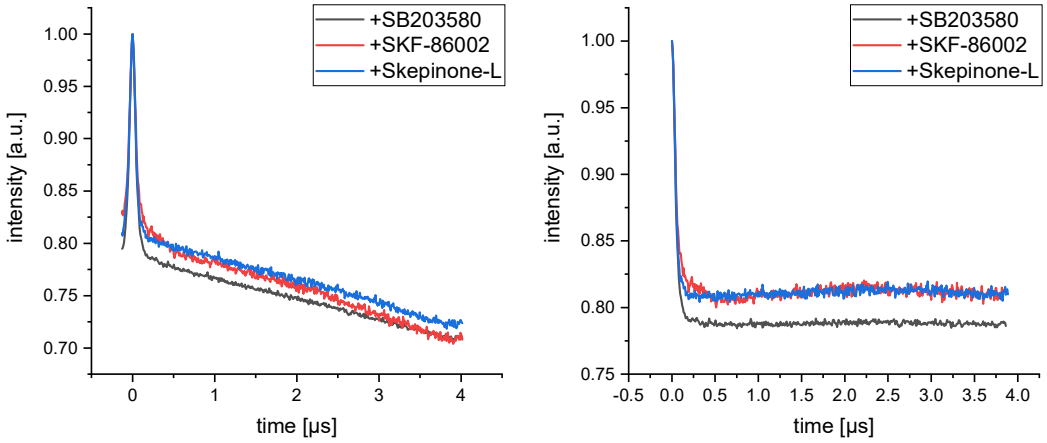

Figure A. 27: Measurements with p38α 251 in the presence of inhibitors . Left: Raw DEER data traces obtained for p38α 251 with the three type I inhibitors. Right: Form factors obtained for the DEER traces.

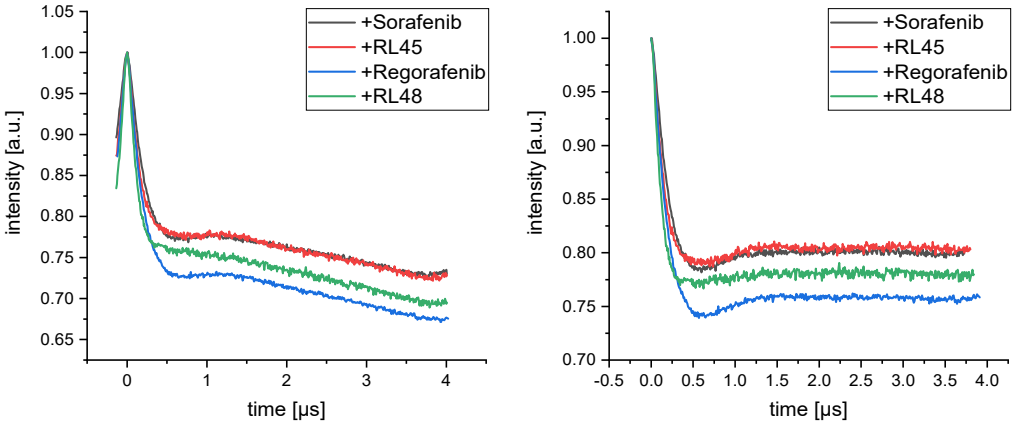

Figure A. 28: Measurements with p38α 251 in the presence of inhibitors . Left: Raw DEER data traces obtained for p38α 251 with the four type II inhibitors. Right: Form factors obtained for the DEER traces.

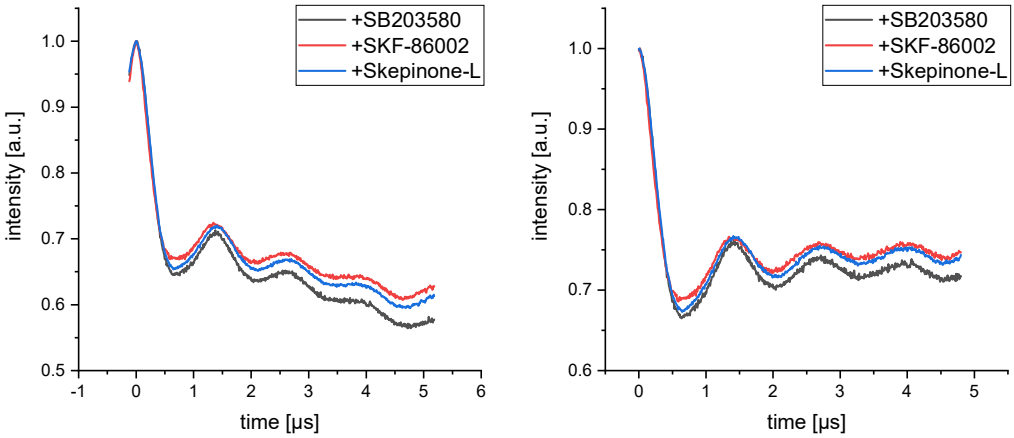

Figure A. 29 Measurements with p38α 277 in the presence of inhibitors . Left: Raw DEER data traces obtained for p38α 277 with the three type I inhibitors. Right: Form factors obtained for the DEER traces.

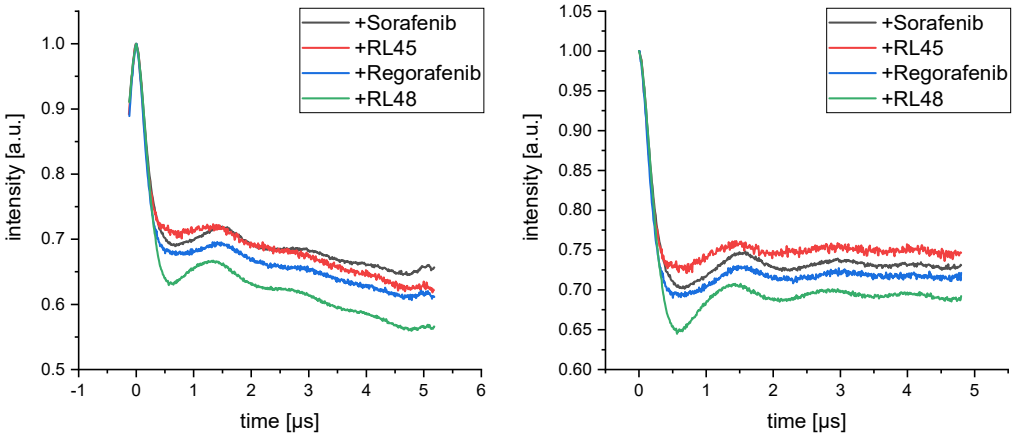

Figure A. 30: Measurements with p38α 277 in the presence of inhibitors . Left: Raw DEER data traces obtained for p38α 277 with the four type II inhibitors. Right: Form factors obtained for the DEER traces

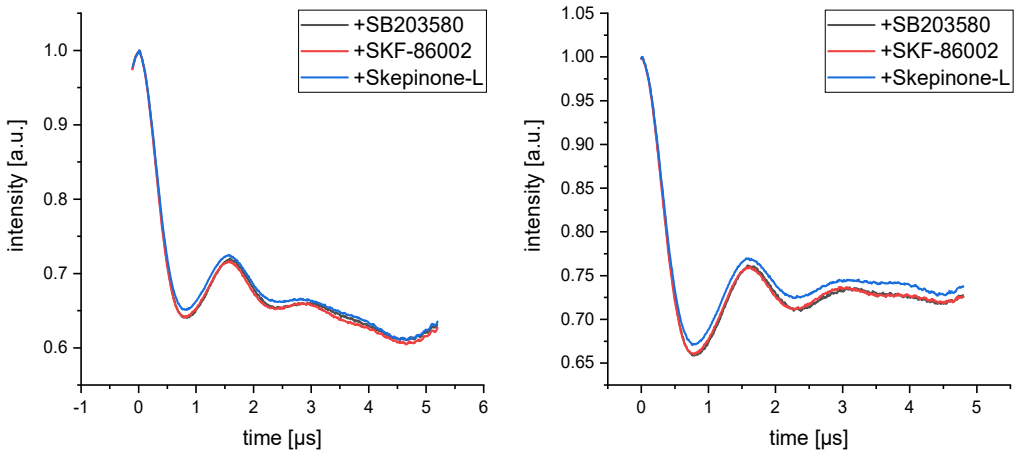

Figure A. 31: Measurements with p38α 309 in the presence of inhibitors . Left: Raw DEER data traces obtained for p38α 309 with the three type I inhibitors. Right: Form factors obtained for the DEER traces.

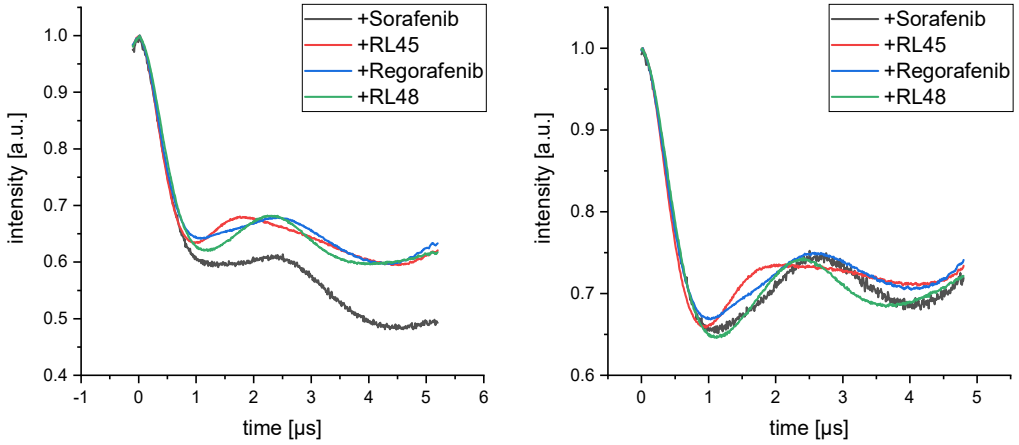

Figure A. 32: Measurements with p38α 309 in the presence of inhibitors . Left: Raw DEER data traces obtained for p38α 309 with the four type II inhibitors. Right: Form factors obtained for the DEER traces.

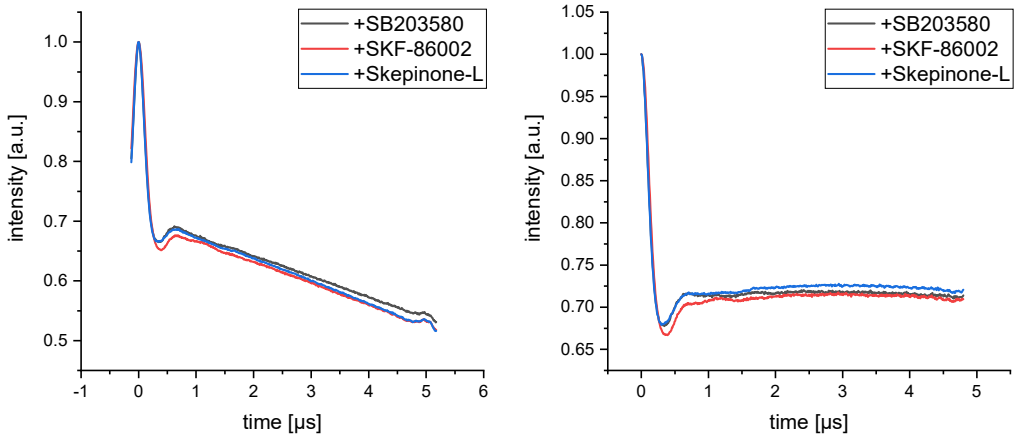

Figure A. 33: Measurements with p38α 347 in the presence of inhibitors . Left: Raw DEER data traces obtained for p38α 347 with the three type I inhibitors. Right: Form factors obtained for the DEER traces.

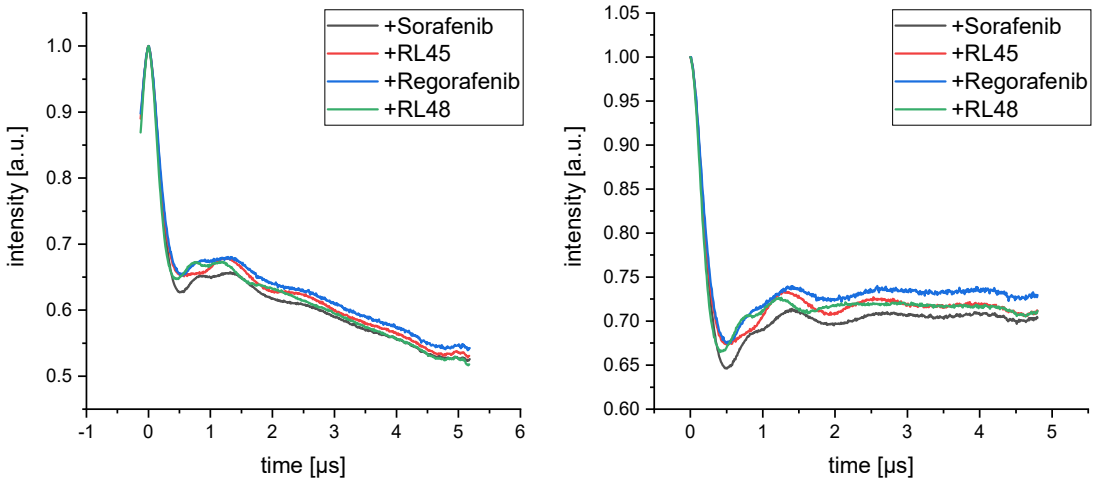

Figure A. 34: Measurements with p38α 347 in the presence of inhibitors . Left: Raw DEER data traces obtained for p38α 347 with the four type II inhibitors. Right: Form factors obtained for the DEER traces.

Distance distributions obtained for p38α

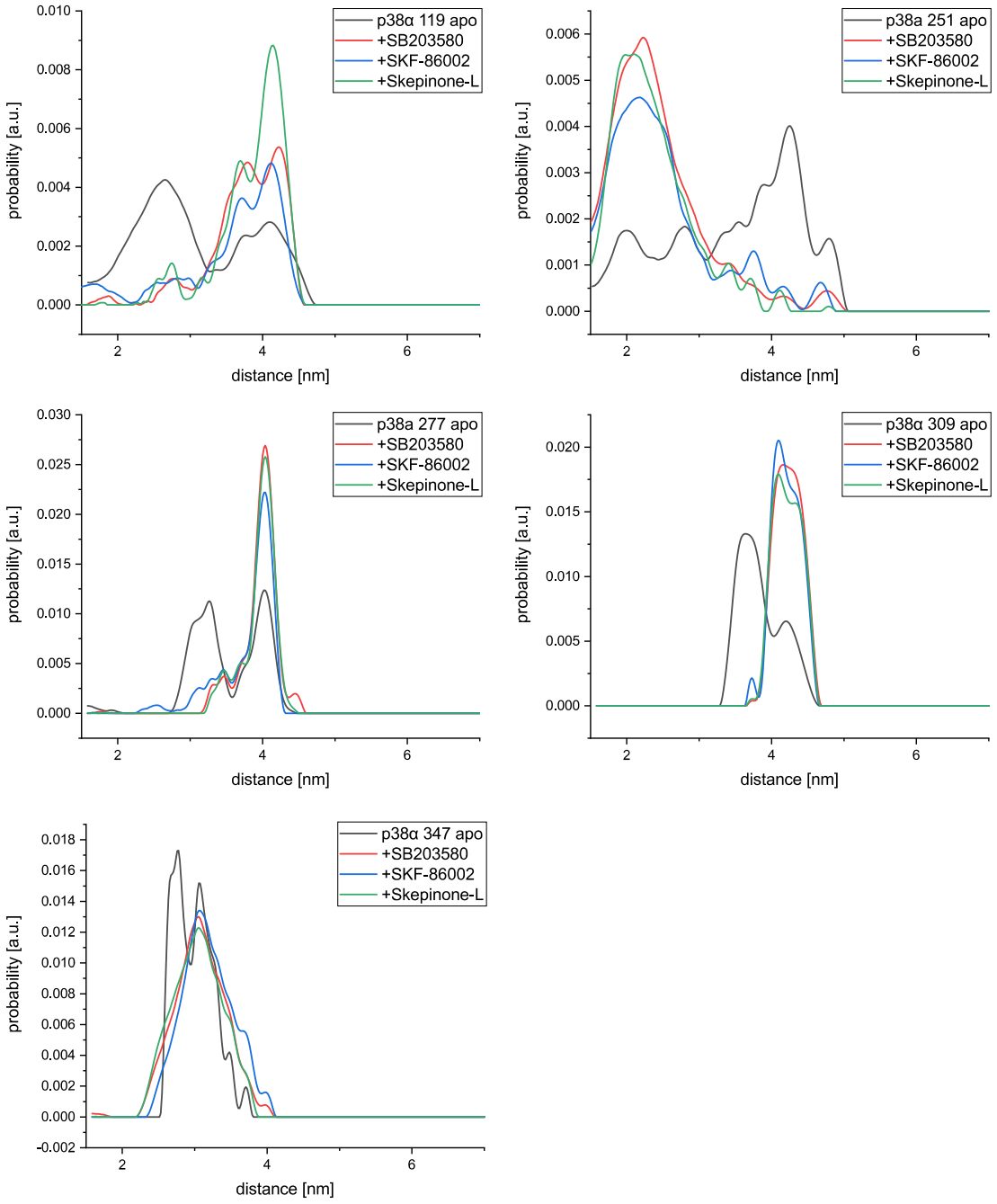

Figure A. 35: All distance distributions obtained for the five double mutants of p38α apo and in combination with the three type I inhibitors.

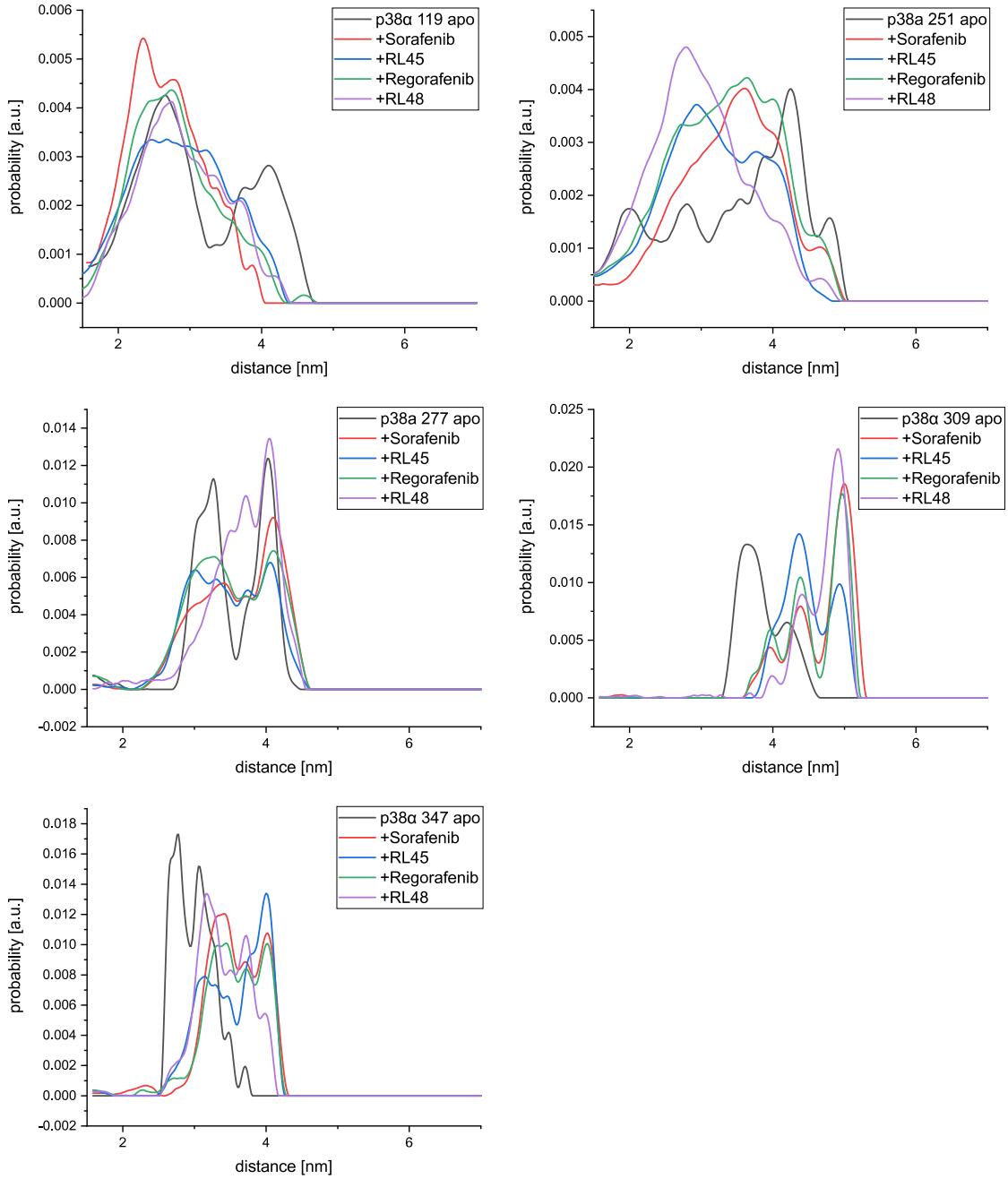

Figure A. 36: All distance distributions obtained for the five double mutants of p38α apo and in combination with the four type II inhibitors.

Multilateration of all type II inhibitors

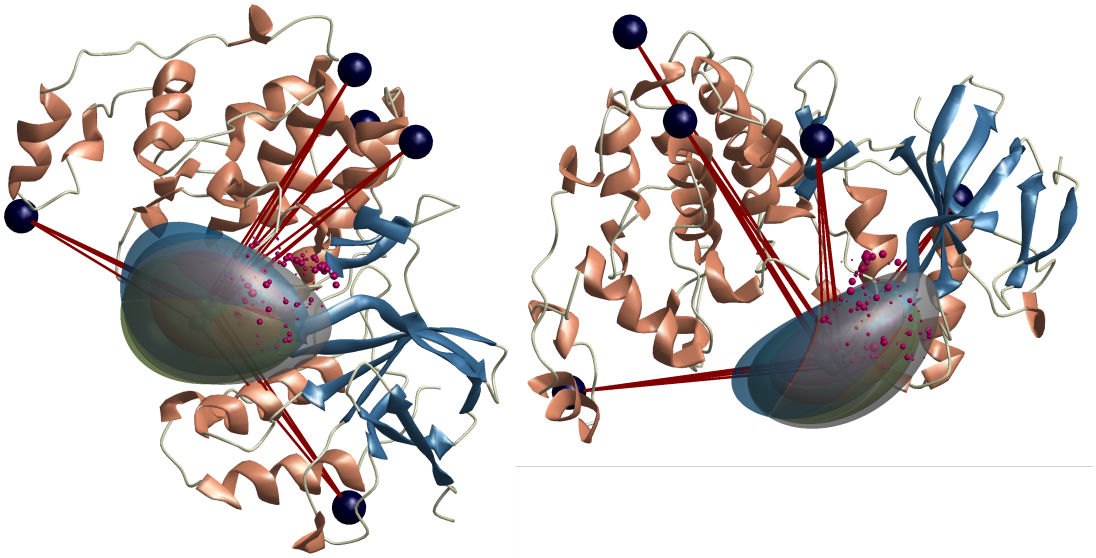

Figure A. 37: Multilateration for all type II inhibitors, structure 3GCU. The probability volumes for RL45 (blue), RL48 (green), Regorafenib (red) and Sorafenib (grey) are shown

10. References

1. McLachlan, A. D., Protein Structure and Function. *Annual Review of Physical Chemistry* **1972,** *23* (1), 165-192.

2. Ouzounis, C. A.; Coulson, R. M. R.; Enright, A. J.; Kunin, V.; Pereira-Leal, J. B., Classification schemes for protein structure and function. *Nature Reviews Genetics* **2003,** *4*, 508.

3. Dyson, H. J.; Wright, P. E., Coupling of folding and binding for unstructured proteins. *Curr Opin Struct Biol* **2002,** *12* (1), 54-60.

4. Nölting, B.; Andert, K., Mechanism of protein folding. *Proteins: Structure, Function, and Bioinformatics* **2000,** *41* (3), 288-298.

5. Gilliland, G.; Berman, H. M.; Weissig, H.; Shindyalov, I. N.; Westbrook, J.; Bourne, P. E.; Bhat, T. N.; Feng, Z., The Protein Data Bank. *Nucleic Acids Res* **2000,** *28* (1), 235-242.

6. Tompa, P., Intrinsically disordered proteins: a 10-year recap. *Trends in Biochemical Sciences* **2012,** *37* (12), 509-516.

7. Uversky, V. N.; Oldfield, C. J.; Dunker, A. K., Intrinsically disordered proteins in human diseases: introducing the D2 concept. *Annu Rev Biophys* **2008,** *37*, 215-46.

8. Uversky, V. N., Intrinsically disordered proteins and their (disordered) proteomes in neurodegenerative disorders. *Front Aging Neurosci* **2015,** *7*.

9. Na, J.-H.; Lee, W.-K.; Yu, Y. G., How Do We Study the Dynamic Structure of Unstructured Proteins: A Case Study on Nopp140 as an Example of a Large, Intrinsically Disordered Protein. *International journal of molecular sciences* **2018,** *19* (2), 381.

10. Eliezer, D., Biophysical characterization of intrinsically disordered proteins. *Curr Opin Struc Biol* **2009,** *19* (1), 23-30.

11. Theillet, F.-X.; Binolfi, A.; Frembgen-Kesner, T.; Hingorani, K.; Sarkar, M.; Kyne, C.; Li, C.; Crowley, P. B.; Gierasch, L.; Pielak, G. J.; Elcock, A. H.; Gershenson, A.; Selenko, P., Physicochemical Properties of Cells and Their Effects on Intrinsically Disordered Proteins (IDPs). *Chemical Reviews* **2014,** *114* (13), 6661-6714.

12. Treiber, D. K.; Shah, N. P., Ins and Outs of Kinase DFG Motifs. *Chemistry & Biology* **2013,** *20* (6), 745-746.

13. Wegmann, S.; Medalsy, I. D.; Mandelkow, E.; Müller, D. J., The fuzzy coat of pathological human Tau fibrils is a two-layered polyelectrolyte brush. *Proceedings of the National Academy of Sciences* **2013,** *110* (4), E313-E321.

14. Kosol, S.; Contreras-Martos, S.; Cedeno, C.; Tompa, P., Structural characterization of intrinsically disordered proteins by NMR spectroscopy. *Molecules* **2013,** *18* (9), 10802-28.

15. Brutscher, B.; Felli, I. C.; Gil-Caballero, S.; Hosek, T.; Kummerle, R.; Piai, A.; Pierattelli, R.; Solyom, Z., NMR Methods for the Study of Instrinsically Disordered Proteins Structure, Dynamics, and Interactions: General Overview and Practical Guidelines. *Adv Exp Med Biol* **2015,** *870*, 49-122.

16. Brucale, M.; Schuler, B.; Samorì, B., Single-Molecule Studies of Intrinsically Disordered Proteins. *Chemical Reviews* **2014,** *114* (6), 3281-3317.

17. Chen, H.; Rhoades, E., Fluorescence characterization of denatured proteins. *Curr Opin Struc Biol* **2008,** *18* (4), 516-524.

18. LeBlanc, S. J.; Kulkarni, P.; Weninger, K. R., Single Molecule FRET: A Powerful Tool to Study Intrinsically Disordered Proteins. *Biomolecules* **2018,** *8* (4).

19. Drescher, M., EPR in Protein Science. In *Top Curr Chem*, Drescher, M.; Jeschke, G., Eds. Springer Berlin Heidelberg: Berlin, Heidelberg, 2012; pp 91-119.

20. Marinelli, F.; Fiorin, G., Structural Characterization of Biomolecules through Atomistic Simulations Guided by DEER Measurements. *Structure* **2019,** *27* (2), 359-370.e12.

21. Islam, S. M.; Stein, R. A.; McHaourab, H. S.; Roux, B., Structural Refinement from Restrained-Ensemble Simulations Based on EPR/DEER Data: Application to T4 Lysozyme. *The Journal of Physical Chemistry B* **2013,** *117* (17), 4740-4754.

22. Reginsson, G. W.; Schiemann, O., Spin labeling of DNA and RNA. In *Encyclopedia of Biophysics*, Springer: 2013; pp 2429-2431.

23. Yin, J.-J.; Pasenkiewicz-Gierula, M.; Hyde, J. S., Lateral diffusion of lipids in membranes by pulse saturation recovery electron spin resonance. *Proceedings of the National Academy of Sciences* **1987,** *84* (4), 964-968.

24. Jeschke, G.; Sajid, M.; Schulte, M.; Ramezanian, N.; Volkov, A.; Zimmermann, H.; Godt, A., Flexibility of shape-persistent molecular building blocks composed of p-phenylene and ethynylene units. *J Am Chem Soc* **2010,** *132* (29), 10107-17.

25. Hintze, C.; Schütze, F.; Drescher, M.; Mecking, S., Probing of chain conformations in conjugated polymer nanoparticles by electron spin resonance spectroscopy. *Phys Chem Chem Phys* **2015,** *17* (48), 32289-32296.

26. Kay, C. W.; Feicht, R.; Schulz, K.; Sadewater, P.; Sancar, A.; Bacher, A.; Möbius, K.; Richter, G.; Weber, S., EPR, ENDOR, and TRIPLE resonance spectroscopy on the neutral flavin radical in Escherichia coli DNA photolyase. *Biochemistry-Us* **1999,** *38* (51), 16740-16748.

27. Bittl, R.; Zech, S. G., Pulsed EPR Study of Spin-Coupled Radical Pairs in Photosynthetic Reaction Centers: Measurement of the Distance Between and in Photosystem I and between and in Bacterial Reaction Centers. *The Journal of Physical Chemistry B* **1997,** *101* (8), 1429-1436.

28. Wertz, J., *Electron spin resonance: elementary theory and practical applications*. Springer Science & Business Media: 2012.

29. Freed, J. H., Theory of slow tumbling ESR spectra for nitroxides. *Spin Labeling: theory and applications* **1976,** *1*, 53-132.

30. Hubbell, W. L.; McHaourab, H. S.; Altenbach, C.; Lietzow, M. A., Watching proteins move using site-directed spin labeling. *Structure* **1996,** *4* (7), 779-83.

31. Isas, J. M.; Langen, R.; Haigler, H. T.; Hubbell, W. L., Structure and dynamics of a helical hairpin and loop region in annexin 12: a site-directed spin labeling study. *Biochemistry-Us* **2002,** *41* (5), 1464-1473.

32. Molin, Y. N.; Salikhov, K. M.; Zamaraev, K. I. i., *Spin exchange*. Springer-Verlag: 1980.

33. Altenbach, C.; Froncisz, W.; Hemker, R.; Mchaourab, H.; Hubbell, W. L., Accessibility of nitroxide side chains: absolute Heisenberg exchange rates from power saturation EPR. *Biophysical journal* **2005,** *89* (3), 2103-2112.

34. Smirnova, T. I.; Smirnov, A. I., High-field ESR spectroscopy in membrane and protein biophysics. In *ESR spectroscopy in Membrane Biophysics*, Springer: 2007; pp 165-251.

35. Earle, K. A.; Moscicki, J. K.; Ge, M.; Budil, D. E.; Freed, J. H., 250-GHz electron spin resonance studies of polarity gradients along the aliphatic chains in phospholipid membranes. *Biophysical journal* **1994,** *66* (4), 1213.

36. Griffith, O.; Dehlinger, P.; Van, S., Shape of the hydrophobic barrier of phospholipid bilayers (evidence for water penetration in biological membranes). *The Journal of membrane biology* **1974,** *15* (1), 159-192.

37. Steinhoff, H.-J.; Savitsky, A.; Wegener, C.; Pfeiffer, M.; Plato, M.; Möbius, K., High-field EPR studies of the structure and conformational changes of site-directed spin labeled bacteriorhodopsin. *Biochimica et Biophysica Acta (BBA)-Bioenergetics* **2000,** *1457* (3), 253-262.

38. Altenbach, C.; Flitsch, S. L.; Khorana, H. G.; Hubbell, W. L., Structural studies on transmembrane proteins. 2. Spin labeling of bacteriorhodopsin mutants at unique cysteines. *Biochemistry* **1989,** *28* (19), 7806-12.

39. Altenbach, C.; Marti, T.; Khorana, H. G.; Hubbell, W. L., Transmembrane protein structure: spin labeling of bacteriorhodopsin mutants. *Science* **1990,** *248* (4959), 1088-92.

40. Berliner, L. J., *Spin labeling : theory and applications*. Academic Press: New York, 1976.

41. Potapov, A.; Yagi, H.; Huber, T.; Jergic, S.; Dixon, N. E.; Otting, G.; Goldfarb, D., Nanometer-scale distance measurements in proteins using Gd3+ spin labeling. *J Am Chem Soc* **2010,** *132* (26), 9040-8.

42. Qi, M.; Gross, A.; Jeschke, G.; Godt, A.; Drescher, M., Gd(III)-PyMTA label is suitable for in-cell EPR. *J Am Chem Soc* **2014,** *136* (43), 15366-78.

43. Martorana, A.; Bellapadrona, G.; Feintuch, A.; Di Gregorio, E.; Aime, S.; Goldfarb, D., Probing protein conformation in cells by EPR distance measurements using Gd3+ spin labeling. *J Am Chem Soc* **2014,** *136* (38), 13458-65.

44. Griffith, O. H.; Waggoner, A., Nitroxide free radicals: spin labels for probing biomolecular structure. *Accounts of Chemical Research* **1969,** *2* (1), 17-24.

45. Klare, J. P.; Steinhoff, H. J., Spin labeling EPR. *Photosynth. Res.* **2009,** *102* (2-3), 377.

46. Klare, J. P., Site-directed spin labeling EPR spectroscopy in protein research. *Biol Chem* **2013,** *394* (10), 1281-300.

47. Hubbell, W. L.; Lopez, C. J.; Altenbach, C.; Yang, Z., Technological advances in site-directed spin labeling of proteins. *Curr Opin Struct Biol* **2013,** *23* (5), 725-33.

48. Paletta, J. T.; Pink, M.; Foley, B.; Rajca, S.; Rajca, A., Synthesis and Reduction Kinetics of Sterically Shielded Pyrrolidine Nitroxides. *Organic Letters* **2012,** *14* (20), 5322-5325.

49. Hyodo, F.; Matsumoto, K.; Matsumoto, A.; Mitchell, J. B.; Krishna, M. C., Probing the intracellular redox status of tumors with magnetic resonance imaging and redox-sensitive contrast agents. *Cancer Res* **2006,** *66* (20), 9921-8.

50. Marx, L.; Chiarelli, R.; Guiberteau, T.; Rassat, A., A comparative study of the reduction by ascorbate of 1,1,3,3-tetraethylisoindolin-2-yloxyl and of 1,1,3,3-tetramethylisoindolin-2-yloxyl. *Journal of the Chemical Society-Perkin Transactions 1* **2000,** (8), 1181-1182.

51. Azarkh, M.; Okle, O.; Eyring, P.; Dietrich, D. R.; Drescher, M., Evaluation of spin labels for in-cell EPR by analysis of nitroxide reduction in cell extract of Xenopus laevis oocytes. *J Magn Reson* **2011,** *212* (2), 450-4.

52. Bobko, A. A.; Kirilyuk, I. A.; Grigor'ev, I. A.; Zweier, J. L.; Khramtsov, V. V., Reversible reduction of nitroxides to hydroxylamines: Roles for ascorbate and glutathione. *Free Radical Biology and Medicine* **2007,** *42* (3), 404-412.

53. Emoto, M.; Mito, F.; Yamasaki, T.; Yamada, K. I.; Sato-Akaba, H.; Hirata, H.; Fujii, H., A novel ascorbic acid-resistant nitroxide in fat emulsion is an efficient brain imaging probe for in vivo EPR imaging of mouse. *Free Radical Research* **2011,** *45* (11-12), 1325-1332.

54. Jagtap, A. P.; Krstic, I.; Kunjir, N. C.; Hänsel, R.; Prisner, T. F.; Sigurdsson, S. T., Sterically shielded spin labels for in-cell EPR spectroscopy: Analysis of stability in reducing environment. *Free Radical Research* **2015,** *49* (1), 78-85.

55. Baldauf, C.; Schulze, K.; Lueders, P.; Bordignon, E.; Tampe, R., In-situ spin labeling of his-tagged proteins: distance measurements under in-cell conditions. *Chemistry* **2013,** *19* (41), 13714-9.

56. Cunningham, T. F.; Putterman, M. R.; Desai, A.; Horne, W. S.; Saxena, S., The double-histidine Cu(2)(+)-binding motif: a highly rigid, site-specific spin probe for electron spin resonance distance measurements. *Angew Chem Int Ed Engl* **2015,** *54* (21), 6330-4.

57. Fleissner, M. R.; Bridges, M. D.; Brooks, E. K.; Cascio, D.; Kalai, T.; Hideg, K.; Hubbell, W. L., Structure and dynamics of a conformationally constrained nitroxide side chain and applications in EPR spectroscopy. *Proc Natl Acad Sci U S A* **2011,** *108* (39), 16241-6.

58. Altenbach, C.; Flitsch, S. L.; Khorana, H. G.; Hubbell, W. L., Structural studies on transmembrane proteins. 2. Spin labeling of bacteriorhodopsin mutants at unique cysteines. *Biochemistry-Us* **1989,** *28* (19), 7806-7812.

59. Altenbach, C.; Marti, T.; Khorana, H. G.; Hubbell, W. L., Transmembrane Protein-Structure - Spin Labeling of Bacteriorhodopsin Mutants. *Science* **1990,** *248* (4959), 1088-1092.

60. Griffith, O. H.; McConnell, H. M., A NITROXIDE-MALEIMIDE SPIN LABEL. *Proceedings of the National Academy of Sciences* **1966,** *55* (1), 8-11.

61. Fleissner, M. R.; Cascio, D.; Hubbell, W. L., Structural origin of weakly ordered nitroxide motion in spin-labeled proteins. *Protein Sci* **2009,** *18* (5), 893-908.

62. Columbus, L.; Kalai, T.; Jeko, J.; Hideg, K.; Hubbell, W. L., Molecular motion of spin labeled side chains in alpha-helices: analysis by variation of side chain structure. *Biochemistry* **2001,** *40* (13), 3828-46.

63. Rassat, A.; Rey, P., [Nitroxides. 23. Preparation of amino acid free radicals and their complex salts]. *Bull Soc Chim Fr* **1967,** *3*, 815-8.

64. Nakaie, C. R.; Goissis, G.; Schreier, S.; Paiva, A. C., pH dependence of EPR spectra of nitroxides containing ionizable groups. *Braz J Med Biol Res* **1981,** *14* (2-3), 173-80.

65. Stoller, S.; Sicoli, G.; Baranova, T. Y.; Bennati, M.; Diederichsen, U., TOPP: a novel nitroxide-labeled amino acid for EPR distance measurements. *Angew Chem Int Ed Engl* **2011,** *50* (41), 9743-6.

66. Jeschke, G., MMM: A toolbox for integrative structure modeling. *Protein Sci* **2018,** *27* (1), 76-85.

67. The PyMOL Molecular Graphics System, Version 2.1 Schrödinger, LLC.

68. Berliner, L., *Spin labeling II: Theory and applications*. Academic, New York: 1979.

69. Brustolon, M., What Can Be Studied with Electron Paramagnetic Resonance? *Electron Paramagnetic Resonance: A Practitioner's Toolkit* **2009**, 83-108.

70. McHaourab, Hassane S.; Steed, P. R.; Kazmier, K., Toward the Fourth Dimension of Membrane Protein Structure: Insight into Dynamics from Spin-Labeling EPR Spectroscopy. *Structure* **2011,** *19* (11), 1549-1561.

71. Tilegenova, C.; Elberson, B. W.; Marien Cortes, D.; Cuello, L. G., CW-EPR Spectroscopy and Site-Directed Spin Labeling to Study the Structural Dynamics of Ion Channels. *Methods Mol Biol* **2018,** *1684*, 279-288.

72. Stoll, S.; Schweiger, A., EasySpin, a comprehensive software package for spectral simulation and analysis in EPR. *J Magn Reson* **2006,** *178* (1), 42-55.

73. Budil, D. E.; Lee, S.; Saxena, S.; Freed, J. H., Nonlinear-Least-Squares Analysis of Slow-Motion EPR Spectra in One and Two Dimensions Using a Modified Levenberg–Marquardt Algorithm. *Journal of Magnetic Resonance, Series A* **1996,** *120* (2), 155-189.

74. Kensch, O.; Restle, T.; Wohrl, B. M.; Goody, R. S.; Steinhoff, H. J., Temperature-dependent equilibrium between the open and closed conformation of the p66 subunit of HIV-1 reverse transcriptase revealed by site-directed spin labelling. *Journal of Molecular Biology* **2000,** *301* (4), 1029-1039.

75. Eaton, S. S.; Eaton, G. R., Distance Measurements by CW and Pulsed EPR. In *Distance Measurements in Biological Systems by EPR*, Berliner, L. J.; Eaton, G. R.; Eaton, S. S., Eds. Springer US: Boston, MA, 2000; pp 1-27.

76. Jeschke, G.; Spiess, H. W., Distance measurements in solid-state NMR and EPR spectroscopy. In *Novel NMR and EPR techniques*, Springer: 2006; pp 21-63.

77. McHaourab, H. S.; Lietzow, M. A.; Hideg, K.; Hubbell, W. L., Motion of spin-labeled side chains in T4 lysozyme. Correlation with protein structure and dynamics. *Biochemistry* **1996,** *35* (24), 7692-704.

78. Schmidt, T.; Wälti, M. A.; Baber, J. L.; Hustedt, E. J.; Clore, G. M., Long Distance Measurements up to 160 Å in the GroEL Tetradecamer Using Q-Band DEER EPR Spectroscopy. **2016,** *55* (51), 15905-15909.

79. Ward, R.; Bowman, A.; Sozudogru, E.; El-Mkami, H.; Owen-Hughes, T.; Norman, D. G., EPR distance measurements in deuterated proteins. *J Magn Reson* **2010,** *207* (1), 164-167.

80. Bowman, A.; Hammond, C. M.; Stirling, A.; Ward, R.; Shang, W.; El-Mkami, H.; Robinson, D. A.; Svergun, D. I.; Norman, D. G.; Owen-Hughes, T., The histone chaperones

Vps75 and Nap1 form ring-like, tetrameric structures in solution. *Nucleic Acids Res* **2014,** *42* (9), 6038-6051.

81. Hintze, C., Masterarbeit, Universität Konstanz. **2011**, 64.

82. Georgieva, E. R.; Roy, A. S.; Grigoryants, V. M.; Borbat, P. P.; Earle, K. A.; Scholes, C. P.; Freed, J. H., Effect of freezing conditions on distances and their distributions derived from Double Electron Electron Resonance (DEER): a study of doubly-spin-labeled T4 lysozyme. *J Magn Reson* **2012,** *216*, 69-77.

83. Yang, Z.; Jiménez-Osés, G.; López, C. J.; Bridges, M. D.; Houk, K. N.; Hubbell, W. L., Long-Range Distance Measurements in Proteins at Physiological Temperatures Using Saturation Recovery EPR Spectroscopy. *J Am Chem Soc* **2014,** *136* (43), 15356-15365.

84. Rajca, A.; Kathirvelu, V.; Roy, S. K.; Pink, M.; Rajca, S.; Sarkar, S.; Eaton, S. S.; Eaton, G. R., A spirocyclohexyl nitroxide amino acid spin label for pulsed EPR spectroscopy distance measurements. *Chem-Eur J* **2010,** *16* (19), 5778-5782.

85. Meyer, V.; Swanson, M. A.; Clouston, L. J.; Boratynski, P. J.; Stein, R. A.; McHaourab, H. S.; Rajca, A.; Eaton, S. S.; Eaton, G. R., Room-temperature distance measurements of immobilized spin-labeled protein by DEER/PELDOR. *Biophys J* **2015,** *108* (5), 1213-9.

86. Yang, Z.; Liu, Y.; Borbat, P.; Zweier, J. L.; Freed, J. H.; Hubbell, W. L., Pulsed ESR dipolar spectroscopy for distance measurements in immobilized spin labeled proteins in liquid solution. *J Am Chem Soc* **2012,** *134* (24), 9950-2.

87. Banham, J. E.; Baker, C. M.; Ceola, S.; Day, I. J.; Grant, G. H.; Groenen, E. J.; Rodgers, C. T.; Jeschke, G.; Timmel, C. R., Distance measurements in the borderline region of applicability of CW EPR and DEER: a model study on a homologous series of spin-labelled peptides. *J Magn Reson* **2008,** *191* (2), 202-218.

88. Meyer, A.; Jassoy, J. J.; Spicher, S.; Berndhauser, A.; Schiemann, O., Performance of PELDOR, RIDME, SIFTER, and DQC in measuring distances in trityl based bi- and triradicals: exchange coupling, pseudosecular coupling and multi-spin effects. *Phys Chem Chem Phys* **2018**.

89. Borbat, P. P.; Freed, J. H., Multiple-quantum ESR and distance measurements. *Chem Phys Lett* **1999,** *313* (1), 145-154.

90. Borbat, P. P.; Freed, J. H., Double-quantum ESR and distance measurements. In *Distance measurements in biological systems by EPR*, Springer: 2002; pp 383-459.

91. Schöps, P.; Spindler, P. E.; Marko, A.; Prisner, T. F., Broadband spin echoes and broadband SIFTER in EPR. *J Magn Reson* **2015,** *250*, 55-62.

92. Milikisyants, S.; Scarpelli, F.; Finiguerra, M. G.; Ubbink, M.; Huber, M., A pulsed EPR method to determine distances between paramagnetic centers with strong spectral anisotropy and radicals: the dead-time free RIDME sequence. *J Magn Reson* **2009,** *201* (1), 48-56.

93. Milov, A.; Salikhov, K.; Shirov, M., Application of ELDOR in electron-spin echo for paramagnetic center space distribution in solids. *Fizika Tverdogo Tela* **1981,** *23* (4), 975-982.

94. Milov, A.; Ponomarev, A.; Tsvetkov, Y. D., Electron-electron double resonance in electron spin echo: Model biradical systems and the sensitized photolysis of decalin. *Chem Phys Lett* **1984,** *110* (1), 67-72.

95. Pannier, M.; Veit, S.; Godt, A.; Jeschke, G.; Spiess, H. W., Dead-time free measurement of dipole-dipole interactions between electron spins. *J Magn Reson* **2000,** *142* (2), 331-340.

96. Jeschke, G.; Bender, A.; Paulsen, H.; Zimmermann, H.; Godt, A., Sensitivity enhancement in pulse EPR distance measurements. *J Magn Reson* **2004,** *169* (1), 1-12.

97. Bowen, A. M.; Tait, C. E.; Timmel, C. R.; Harmer, J. R., Orientation-selective DEER using rigid spin labels, cofactors, metals, and clusters. In *Structural Information from Spin-Labels and Intrinsic Paramagnetic Centres in the Biosciences*, Springer: 2013; pp 283-327.

98. Jeschke, G., DEER Distance Measurements on Proteins. *Ann. Rev. Phys. Chem.* **2012,** *63*, 419.

99. Schweiger, A.; Jeschke, G., *Principles of pulse electron paramagnetic resonance*. Oxford University Press: 2001.

100. Eaton, S. S.; Eaton, G. R., Distance measurements by CW and pulsed EPR. In *Distance Measurements in Biological Systems by EPR*, Springer: 2002; pp 1-27.

101. Persson, M.; Harbridge, J. R.; Hammarström, P.; Mitri, R.; Mårtensson, L.-G.; Carlsson, U.; Eaton, G. R.; Eaton, S. S., Comparison of Electron Paramagnetic Resonance Methods to Determine Distances between Spin Labels on Human Carbonic Anhydrase II. *Biophysical Journal* **2001,** *80* (6), 2886-2897.

102. Polyhach, Y.; Bordignon, E.; Jeschke, G., Rotamer libraries of spin labelled cysteines for protein studies. *Phys Chem Chem Phys* **2011,** *13* (6), 2356-66.

103. Jeschke, G., Ensemble models of proteins and protein domains based on distance distribution restraints. *Proteins* **2016,** *84* (4), 544-60.

104. Rao, J. N.; Jao, C. C.; Hegde, B. G.; Langen, R.; Ulmer, T. S., A Combinatorial NMR and EPR Approach for Evaluating the Structural Ensemble of Partially Folded Proteins. *J Am Chem Soc* **2010,** *132* (25), 8657-8668.

105. Jao, C. C.; Hegde, B. G.; Chen, J.; Haworth, I. S.; Langen, R., Structure of membrane-bound alpha-synuclein from site-directed spin labeling and computational refinement. *Proc Natl Acad Sci U S A* **2008,** *105* (50), 19666-71.

106. Reichel, K.; Stelzl, L. S.; Köfinger, J.; Hummer, G., Precision DEER Distances from Spin-Label Ensemble Refinement. *The Journal of Physical Chemistry Letters* **2018,** *9* (19), 5748-5752.

107. Gigli, L.; Andrałojć, W.; Dalaloyan, A.; Parigi, G.; Ravera, E.; Goldfarb, D.; Luchinat, C., Assessing protein conformational landscapes: integration of DEER data in Maximum Occurrence analysis. *Phys Chem Chem Phys* **2018**.

108. Abdullin, D.; Florin, N.; Hagelueken, G.; Schiemann, O., EPR-based approach for the localization of paramagnetic metal ions in biomolecules. *Angew Chem Int Ed Engl* **2015,** *54* (6), 1827-31.

109. Lopez, C. J.; Yang, Z.; Altenbach, C.; Hubbell, W. L., Conformational selection and adaptation to ligand binding in T4 lysozyme cavity mutants. *Proc Natl Acad Sci U S A* **2013,** *110* (46), E4306-15.

110. Gaffney, B. J.; Bradshaw, M. D.; Frausto, S. D.; Wu, F.; Freed, J. H.; Borbat, P., Locating a lipid at the portal to the lipoxygenase active site. *Biophys J* **2012,** *103* (10), 2134-44.

111. Borbat, P. P.; McHaourab, H. S.; Freed, J. H., Protein Structure Determination Using Long-Distance Constraints from Double-Quantum Coherence ESR: Study of T4 Lysozyme. *J Am Chem Soc* **2002,** *124* (19), 5304-5314.

112. Evans, Eric G. B.; Pushie, M. J.; Markham, Kate A.; Lee, H.-W.; Millhauser, Glenn L., Interaction between Prion Protein's Copper-Bound Octarepeat Domain and a Charged C-Terminal Pocket Suggests a Mechanism for N-Terminal Regulation. *Structure* **2016,** *24* (7), 1057-1067.

113. Yang, Z.; Kurpiewski, M. R.; Ji, M.; Townsend, J. E.; Mehta, P.; Jen-Jacobson, L.; Saxena, S., ESR spectroscopy identifies inhibitory Cu²⁺ sites in a DNA-modifying enzyme to reveal determinants of catalytic specificity. *Proceedings of the National Academy of Sciences* **2012,** *109* (17), E993-E1000.

114. Shah, C.; Hegde, Balachandra G.; Morén, B.; Behrmann, E.; Mielke, T.; Moenke, G.; Spahn, Christian M. T.; Lundmark, R.; Daumke, O.; Langen, R., Structural Insights into Membrane Interaction and Caveolar Targeting of Dynamin-like EHD2. *Structure* **2014,** *22* (3), 409-420.

115. Wingler, L. M.; Elgeti, M.; Hilger, D.; Latorraca, N. R.; Lerch, M. T.; Staus, D. P.; Dror, R. O.; Kobilka, B. K.; Hubbell, W. L.; Lefkowitz, R. J., Angiotensin Analogs with Divergent Bias Stabilize Distinct Receptor Conformations. *Cell* **2019,** *176* (3), 468-478.e11.

116. Snatzke, G., Circular Dichroism and Optical Rotatory Dispersion — Principles and Application to the Investigation of the Stereochemistry of Natural Products. **1968,** *7* (1), 14-25.

117. Beychok, S., Circular dichroism of biological macromolecules. *Science* **1966,** *154* (3754), 1288-99.

118. Greenfield, N. J., Using circular dichroism spectra to estimate protein secondary structure. *Nat Protoc* **2007,** *1*, 2876.

119. Brahms, S.; Brahms, J., Determination of protein secondary structure in solution by vacuum ultraviolet circular dichroism. *Journal of Molecular Biology* **1980,** *138* (2), 149-178.

120. Kelly, S. M.; Jess, T. J.; Price, N. C., How to study proteins by circular dichroism. *Bba-Proteins Proteom* **2005,** *1751* (2), 119-139.

121. Drake, A. F., Polarization Modulation - the Measurement of Linear and Circular-Dichroism. *J Phys E Sci Instrum* **1986,** *19* (3), 170-181.

122. de Jongh, H. H. J.; Goormaghtigh, E.; Killian, J. A., Analysis of Circular Dichroism Spectra of Oriented Protein-Lipid Complexes: Toward a General Application. *Biochemistry-Us* **1994,** *33* (48), 14521-14528.

123. Emamzadeh, F. N., Alpha-synuclein structure, functions, and interactions. *Journal of research in medical sciences : the official journal of Isfahan University of Medical Sciences* **2016,** *21*, 29-29.

124. Goedert, M., Alpha-synuclein and neurodegenerative diseases. *Nature Reviews Neuroscience* **2001,** *2* (7), 492-501.

125. Pujols, J.; Peña-Díaz, S.; Lázaro, D. F.; Peccati, F.; Pinheiro, F.; González, D.; Carija, A.; Navarro, S.; Conde-Giménez, M.; García, J.; Guardiola, S.; Giralt, E.; Salvatella, X.; Sancho, J.; Sodupe, M.; Outeiro, T. F.; Dalfó, E.; Ventura, S., Small molecule inhibits α-synuclein aggregation, disrupts amyloid fibrils, and prevents degeneration of dopaminergic neurons. *Proceedings of the National Academy of Sciences* **2018**.

126. Hsieh, C.-J.; Ferrie, J. J.; Xu, K.; Lee, I.; Graham, T. J. A.; Tu, Z.; Yu, J.; Dhavale, D.; Kotzbauer, P.; Petersson, E. J.; Mach, R. H., Alpha Synuclein Fibrils Contain Multiple Binding Sites for Small Molecules. *Acs Chem Neurosci* **2018**.

127. Roeters, S. J.; Iyer, A.; Pletikapic, G.; Kogan, V.; Subramaniam, V.; Woutersen, S., Evidence for Intramolecular Antiparallel Beta-Sheet Structure in Alpha-Synuclein Fibrils from a Combination of Two-Dimensional Infrared Spectroscopy and Atomic Force Microscopy. *Sci Rep* **2017,** *7*, 41051.

128. Marotta, N. P.; Lin, Y. H.; Lewis, Y. E.; Ambroso, M. R.; Zaro, B. W.; Roth, M. T.; Arnold, D. B.; Langen, R.; Pratt, M. R., O-GlcNAc modification blocks the aggregation and toxicity of the protein alpha-synuclein associated with Parkinson's disease. *Nat Chem* **2015,** *7* (11), 913-20.

129. Kang, L.; Moriarty, G. M.; Woods, L. A.; Ashcroft, A. E.; Radford, S. E.; Baum, J., N-terminal acetylation of α-synuclein induces increased transient helical propensity and decreased aggregation rates in the intrinsically disordered monomer. *Protein Sci* **2012,** *21* (7), 911-917.

130. Shvadchak, V. V.; Subramaniam, V., A Four-Amino Acid Linker between Repeats in the alpha-Synuclein Sequence Is Important for Fibril Formation. *Biochemistry-Us* **2014,** *53* (2), 279-281.

131. Schaser, A. J.; Osterberg, V. R.; Dent, S. E.; Stackhouse, T. L.; Wakeham, C. M.; Boutros, S. W.; Weston, L. J.; Owen, N.; Weissman, T. A.; Luna, E.; Raber, J.; Luk, K. C.; McCullough, A. K.; Woltjer, R. L.; Unni, V. K., Alpha-synuclein is a DNA binding protein that modulates DNA repair with implications for Lewy body disorders. *Sci Rep-Uk* **2019,** *9* (1), 10919.

132. Ruggeri, F. S.; Benedetti, F.; Knowles, T. P. J.; Lashuel, H. A.; Sekatskii, S.; Dietler, G., Identification and nanomechanical characterization of the fundamental single-strand protofilaments of amyloid α-synuclein fibrils. *Proceedings of the National Academy of Sciences* **2018**.

133. Conway, K. A.; Lee, S. J.; Rochet, J. C.; Ding, T. T.; Williamson, R. E.; Lansbury, P. T., Acceleration of oligomerization, not fibrillization, is a shared property of both alpha-synuclein mutations linked to early-onset Parkinson's disease: Implications for pathogenesis and therapy. *P Natl Acad Sci USA* **2000,** *97* (2), 571-576.

134. Whiten, D. R.; Cox, D.; Horrocks, M. H.; Taylor, C. G.; De, S.; Flagmeier, P.; Tosatto, L.; Kumita, J. R.; Ecroyd, H.; Dobson, C. M.; Klenerman, D.; Wilson, M. R., Single-Molecule Characterization of the Interactions between Extracellular Chaperones and Toxic α-Synuclein Oligomers. *Cell Rep* **2018,** *23* (12), 3492-3500.

135. Dettmer, U.; Newman, A. J.; von Saucken, V. E.; Bartels, T.; Selkoe, D., KTKEGV repeat motifs are key mediators of normal alpha-synuclein tetramerization: Their mutation causes excess monomers and neurotoxicity. *Proc Natl Acad Sci U S A* **2015**.

136. Coelho-Cerqueira, E.; Carmo-Goncalves, P.; Pinheiro, A. S.; Cortines, J.; Follmer, C., alpha-Synuclein as an intrinsically disordered monomer - fact or artefact? *Febs J* **2013,** *280* (19), 4915-4927.

137. Dedmon, M. M.; Lindorff-Larsen, K.; Christodoulou, J.; Vendruscolo, M.; Dobson, C. M., Mapping long-range interactions in alpha-synuclein using spin-label NMR and ensemble molecular dynamics simulations. *J Am Chem Soc* **2005,** *127* (2), 476-7.

138. Theillet, F. X.; Binolfi, A.; Bekei, B.; Martorana, A.; Rose, H. M.; Stuiver, M.; Verzini, S.; Lorenz, D.; van Rossum, M.; Goldfarb, D.; Selenko, P., Structural disorder of monomeric alpha-synuclein persists in mammalian cells. *Nature* **2016,** *530* (7588), 45-50.

139. Cattani, J.; Subramaniam, V.; Drescher, M., Room-temperature in-cell EPR spectroscopy: alpha-Synuclein disease variants remain intrinsically disordered in the cell. *Phys Chem Chem Phys* **2017,** *19* (28), 18147-18151.

140. Fakhree, M. A. A.; Zijlstra, N.; Raiss, C. C.; Siero, C. J.; Grabmayr, H.; Bausch, A. R.; Blum, C.; Claessens, M. M. A. E., The number of alpha-synuclein proteins per vesicle gives insights into its physiological function. *Sci Rep-Uk* **2016,** *6*.

141. Pauwels, K.; Lebrun, P.; Tompa, P., To be disordered or not to be disordered: is that still a question for proteins in the cell? *Cell Mol Life Sci* **2017,** *74* (17), 3185-3204.

142. Fakhree, M. A. A.; Nolten, I. S.; Blum, C.; Claessens, M. M. A. E., Different Conformational Subensembles of the Intrinsically Disordered Protein α-Synuclein in Cells. *The Journal of Physical Chemistry Letters* **2018,** *9* (6), 1249-1253.

143. Snead, D.; Eliezer, D., Alpha-synuclein function and dysfunction on cellular membranes. *Exp Neurobiol* **2014,** *23* (4), 292-313.

144. Binolfi, A.; Rasia, R. M.; Bertoncini, C. W.; Ceolin, M.; Zweckstetter, M.; Griesinger, C.; Jovin, T. M.; Fernandez, C. O., Interaction of alpha-synuclein with divalent metal ions reveals key differences: a link between structure, binding specificity and fibrillation enhancement. *J Am Chem Soc* **2006,** *128* (30), 9893-901.

145. Rodriguez, J. A.; Ivanova, M. I.; Sawaya, M. R.; Cascio, D.; Reyes, F. E.; Shi, D.; Sangwan, S.; Guenther, E. L.; Johnson, L. M.; Zhang, M.; Jiang, L.; Arbing, M. A.; Nannenga, B. L.; Hattne, J.; Whitelegge, J.; Brewster, A. S.; Messerschmidt, M.; Boutet, S.; Sauter, N. K.; Gonen, T.; Eisenberg, D. S., Structure of the toxic core of alpha-synuclein from invisible crystals. *Nature* **2015**.

146. Vamvaca, K.; Volles, M. J.; Lansbury, P. T., The First N-terminal Amino Acids of alpha-Synuclein Are Essential for alpha-Helical Structure Formation In Vitro and Membrane Binding in Yeast. *Journal of Molecular Biology* **2009,** *389* (2), 413-424.

147. Conway, K. A.; Harper, J. D.; Lansbury, P. T., Fibrils Formed in Vitro from α-Synuclein and Two Mutant Forms Linked to Parkinson's Disease are Typical Amyloid. *Biochemistry-Us* **2000,** *39* (10), 2552-2563.

148. Robotta, M.; Cattani, J.; Martins, J. C.; Subramaniam, V.; Drescher, M., Alpha-Synuclein Disease Mutations Are Structurally Defective and Locally Affect Membrane Binding. *J Am Chem Soc* **2017,** *139* (12), 4254-4257.

149. Perrin, R. J.; Woods, W. S.; Clayton, D. F.; George, J. M., Interaction of Human α-Synuclein and Parkinson's Disease Variants with Phospholipids: STRUCTURAL ANALYSIS USING SITE-DIRECTED MUTAGENESIS. *Journal of Biological Chemistry* **2000,** *275* (44), 34393-34398.

150. Ulmer, T. S.; Bax, A.; Cole, N. B.; Nussbaum, R. L., Structure and Dynamics of Micelle-bound Human α-Synuclein. *Journal of Biological Chemistry* **2005,** *280* (10), 9595-9603.

151. Bussell, R.; Eliezer, D., Effects of Parkinson's Disease-Linked Mutations on the Structure of Lipid-Associated α-Synuclein. *Biochemistry-Us* **2004,** *43* (16), 4810-4818.

152. Burai, R.; Ait-Bouziad, N.; Chiki, A.; Lashuel, H. A., Elucidating the Role of Site-Specific Nitration of alpha-Synuclein in the Pathogenesis of Parkinson's Disease via Protein Semisynthesis and Mutagenesis. *J Am Chem Soc* **2015,** *137* (15), 5041-5052.

153. Neumann, H.; Hazen, J. L.; Weinstein, J.; Mehl, R. A.; Chin, J. W., Genetically encoding protein oxidative damage. *J Am Chem Soc* **2008,** *130* (12), 4028-4033.

154. Uversky, V. N.; Yamin, G.; Munishkina, L. A.; Karymov, M. A.; Millett, I. S.; Doniach, S.; Lyubchenko, Y. L.; Fink, A. L., Effects of nitration on the structure and aggregation of α-synuclein. *Molecular Brain Research* **2005,** *134* (1), 84-102.

155. Nonaka, T.; Iwatsubo, T.; Hasegawa, M., Ubiquitination of alpha-synuclein. *Biochemistry-Us* **2005,** *44* (1), 361-8.

156. Stephens, A. D.; Nespovitaya, N.; Zacharopoulou, M.; Kaminski, C. F.; Phillips, J. J.; Kaminski Schierle, G. S., Different Structural Conformers of Monomeric α-Synuclein Identified after Lyophilizing and Freezing. *Anal Chem* **2018**.

157. Yu, H.; Han, W.; Ma, W.; Schulten, K., Transient beta-hairpin formation in alpha-synuclein monomer revealed by coarse-grained molecular dynamics simulation. *J Chem Phys* **2015,** *143* (24), 243142.

158. Graen, T.; Klement, R.; Grupi, A.; Haas, E.; Grubmuller, H., Transient Secondary and Tertiary Structure Formation Kinetics in the Intrinsically Disordered State of alpha-Synuclein from Atomistic Simulations. *Chemphyschem* **2018**.

159. Neupane, K.; Solanki, A.; Sosova, I.; Belov, M.; Woodside, M. T., Diverse Metastable Structures Formed by Small Oligomers of alpha-Synuclein Probed by Force Spectroscopy. *Plos One* **2014,** *9* (1).

160. Binolfi, A.; Theillet, F. X.; Selenko, P., Bacterial in-cell NMR of human alpha-synuclein: a disordered monomer by nature? *Biochem Soc T* **2012,** *40*, 950-U292.

161. Allison, J. R.; Rivers, R. C.; Christodoulou, J. C.; Vendruscolo, M.; Dobson, C. M., A Relationship between the Transient Structure in the Monomeric State and the Aggregation Propensities of alpha-Synuclein and beta-Synuclein. *Biochemistry-Us* **2014,** *53* (46), 7170-7183.

162. Waudby, C. A.; Camilloni, C.; Fitzpatrick, A. W. P.; Cabrita, L. D.; Dobson, C. M.; Vendruscolo, M.; Christodoulou, J., In-Cell NMR Characterization of the Secondary Structure Populations of a Disordered Conformation of alpha-Synuclein within E. coli Cells. *Plos One* **2013,** *8* (8).

163. Islam, S. M.; Stein, R. A.; McHaourab, H. S.; Roux, B., Structural refinement from restrained-ensemble simulations based on EPR/DEER data: application to T4 lysozyme. *J Phys Chem B* **2013,** *117* (17), 4740-54.

164. Nami, F.; Gast, P.; Groenen, E. J. J., Rapid Freeze-Quench EPR Spectroscopy: Improved Collection of Frozen Particles. *Appl Magn Reson* **2016,** *47*, 643-653.

165. Gao, C.; Zhou, G.-Y.; Xu, Y.; Hua, T.-C., Glass transition and enthalpy relaxation of ethylene glycol and its aqueous solution. *Thermochimica Acta* **2005,** *435* (1), 38-43.

166. Bedard, L.; Lefevre, T.; Morin-Michaud, E.; Auger, M., Besides Fibrillization: Putative Role of the Peptide Fragment 71-82 on the Structural and Assembly Behavior of alpha-Synuclein. *Biochemistry-Us* **2014,** *53* (41), 6463-6472.

167. Park, S.; Yoon, J.; Jang, S.; Lee, K.; Shin, S., Computational Study on Oligomer Formation of Fibril-forming Peptide of alpha-Synuclein. *B Korean Chem Soc* **2012,** *33* (3), 848-854.

168. Yoon, J.; Jang, S.; Lee, K.; Shin, S., Dimerization of Fibril-forming Segments of alpha-Synuclein. *B Korean Chem Soc* **2009,** *30* (8), 1845-1850.

169. Kruger, R.; Kuhn, W.; Muller, T.; Woitalla, D.; Graeber, M.; Kosel, S.; Przuntek, H.; Epplen, J. T.; Schols, L.; Riess, O., Ala30Pro mutation in the gene encoding alpha-synuclein in Parkinson's disease. *Nat Genet* **1998,** *18* (2), 106-8.

170. Polymeropoulos, M. H.; Lavedan, C.; Leroy, E.; Ide, S. E.; Dehejia, A.; Dutra, A.; Pike, B.; Root, H.; Rubenstein, J.; Boyer, R.; Stenroos, E. S.; Chandrasekharappa, S.; Athanassiadou, A.; Papapetropoulos, T.; Johnson, W. G.; Lazzarini, A. M.; Duvoisin, R. C.; Di Iorio, G.; Golbe, L. I.; Nussbaum, R. L., Mutation in the alpha-synuclein gene identified in families with Parkinson's disease. *Science* **1997,** *276* (5321), 2045-7.

171. Robotta, M.; Hintze, C.; Schildknecht, S.; Zijlstra, N.; Jungst, C.; Karreman, C.; Huber, M.; Leist, M.; Subramaniam, V.; Drescher, M., Locally Resolved Membrane Binding Affinity of the N-Terminus of alpha-Synuclein. *Biochemistry-Us* **2012,** *51* (19), 3960-3962.

172. Nelson, J. W.; Kallenbach, N. R., Stabilization of the ribonuclease S-peptide α-helix by trifluoroethanol. *Proteins: Structure, Function, and Bioinformatics* **1986,** *1* (3), 211-217.

173. Robotta, M.; Hintze, C.; Schildknecht, S.; Zijlstra, N.; Jungst, C.; Karreman, C.; Huber, M.; Leist, M.; Subramaniam, V.; Drescher, M., Locally resolved membrane binding affinity of the N-terminus of alpha-synuclein. *Biochemistry-Us* **2012,** *51* (19), 3960-2.

174. Jeschke, G., DEER Distance Measurements on Proteins. *Annu Rev Phys Chem* **2012,** *63*, 419-446.

175. Chou, P. Y.; Fasman, G. D., Empirical predictions of protein conformation. *Annual review of biochemistry* **1978,** *47*, 251-76.

176. Huang, J.; Rauscher, S.; Nawrocki, G.; Ran, T.; Feig, M.; de Groot, B. L.; Grubmüller, H.; MacKerell Jr, A. D., CHARMM36m: an improved force field for folded and intrinsically disordered proteins. *Nat Methods* **2016,** *14*, 71.

177. Robustelli, P.; Piana, S.; Shaw, D. E., Developing a molecular dynamics force field for both folded and disordered protein states. *Proceedings of the National Academy of Sciences* **2018,** *115* (21), E4758-E4766.

178. Liu, H.; Song, D.; Lu, H.; Luo, R.; Chen, H. F., Intrinsically disordered protein-specific force field CHARMM36IDPSFF. *Chemical biology & drug design* **2018,** *92* (4), 1722-1735.

179. Song, D.; Luo, R.; Chen, H.-F., The IDP-Specific Force Field ff14IDPSFF Improves the Conformer Sampling of Intrinsically Disordered Proteins. *J Chem Inf Model* **2017,** *57* (5), 1166-1178.

180. Lemkau, L. R.; Comellas, G.; Kloepper, K. D.; Woods, W. S.; George, J. M.; Rienstra, C. M., Mutant protein A30P alpha-synuclein adopts wild-type fibril structure, despite slower fibrillation kinetics. *J Biol Chem* **2012,** *287* (14), 11526-32.

181. Chang, L. F.; Karin, M., Mammalian MAP kinase signalling cascades. *Nature* **2001,** *410* (6824), 37-40.

182. Rask-Andersen, M.; Zhang, J.; Fabbro, D.; Schioth, H. B., Advances in kinase targeting: current clinical use and clinical trials. *Trends Pharmacol Sci* **2014,** *35* (11), 60-76.

183. Dominguez, C.; Powers, D. A.; Tamayo, N., p38 MAP kinase inhibitors: Many are made, but few are chosen. *Curr Opin Drug Disc* **2005,** *8* (4), 421-430.

184. Saklatvala, J., The p38 MAP kinase pathway as a therapeutic target in inflammatory disease. *Curr Opin Pharmacol* **2004,** *4* (4), 372-377.

185. Kumar, S.; Boehm, J.; Lee, J. C., p38 map kinases: Key signalling molecules as therapeutic targets for inflammatory diseases. *Nat Rev Drug Discov* **2003,** *2* (9), 717-726.

186. Cuend, A.; Rousseaua, S., p38 MAP-Kinases pathway regulation, function and role in human diseases. *Biochimica et Biophysica Acta (BBA) - Molecular Cell Research (1773)* **2007**, 1358-1375.

187. Wagner, E. F.; Nebreda, A. R., Signal integration by JNK and p38 MAPK pathways in cancer development. *Nat Rev Cancer* **2009,** *9* (8), 537-549.

188. Vogtherr, M.; Saxena, K.; Hoelder, S.; Grimme, S.; Betz, M.; Schieborr, U.; Pescatore, B.; Robin, M.; Delarbre, L.; Langer, T.; Wendt, K. U.; Schwalbe, H., NMR characterization of kinase p38 dynamics in free and ligand-bound forms. *Angewandte Chemie-International Edition* **2006,** *45* (6), 993-997.

189. Huang, Y. M. M.; Chen, W.; Potter, M. J.; Chang, C. E. A., Insights from Free-Energy Calculations: Protein Conformational Equilibrium, Driving Forces, and Ligand-Binding Modes. *Biophysical Journal* **2012,** *103* (2), 342-351.

190. Weisner, J.; Gontla, R.; van der Westhuizen, L.; Oeck, S.; Ketzer, J.; Janning, P.; Richters, A.; Mühlenberg, T.; Fang, Z.; Taher, A.; Jendrossek, V.; Pelly, S. C.; Bauer, S.; van Otterlo, W. A.; Rauh, D., Covalent-Allosteric Kinase Inhibitors. *Angew Chem Int Ed Engl* **2015,** *54* (35), 10313-6.

191. Bührmann, M.; Hardick, J.; Weisner, J.; Quambusch, L.; Rauh, D., Covalent Lipid Pocket Ligands Targeting p38α MAPK Mutants. *Angewandte Chemie International Edition* **2017**, 13232-13236.

192. Fang, Z.; Grütter, C.; Rauh, D., Strategies for the selective regulation of kinases with allosteric modulators: exploiting exclusive structural features. *ACS chemical biology* **2012,** *8* (1), 58-70.

193. Müller, S.; Chaikuad, A.; Gray, N. S.; Knapp, S., The ins and outs of selective kinase inhibitor development. *Nat Chem Biol* **2015,** *11* (11), 818-821.

194. Roskoski, R., Classification of small molecule protein kinase inhibitors based upon the structures of their drug-enzyme complexes. *Pharmacol Res* **2016,** *103*, 26-48.

195. Diskin, R.; Askari, N.; Capone, R.; Engelberg, D.; Livnah, O., Active mutants of the human p38alpha mitogen-activated protein kinase. *J Biol Chem* **2004,** *279* (45), 47040-9.

196. Simard, J. R.; Rauh, D., FLiK: a direct-binding assay for the identification and kinetic characterization of stabilizers of inactive kinase conformations. *Methods Enzymol* **2014,** *548*, 147-71.

197. Muller, S.; Chaikuad, A.; Gray, N. S.; Knapp, S., The ins and outs of selective kinase inhibitor development. *Nat Chem Biol* **2015,** *11* (11), 818-821.

198. Hagelueken, G.; Ward, R.; Naismith, J. H.; Schiemann, O., MtsslWizard: in silico spin-labeling and generation of distance distributions in PyMOL. *Appl Magn Reson* **2012,** *42* (3), 377-391.

199. Earle, K. A., Budil, David E., Calculating Slow-Motion ESR Spectra of Spin-Labeled Polymers. In *Advanced ESR Methods in Polymer Research*, 2006.

200. Cuenda, A.; Rouse, J.; Doza, Y. N.; Meier, R.; Cohen, P.; Gallagher, T. F.; Young, P. R.; Lee, J. C., Sb-203580 Is a Specific Inhibitor of a Map Kinase Homolog Which Is Stimulated by Cellular Stresses and Interleukin-1. *Febs Lett* **1995,** *364* (2), 229-233.

201. Pargellis, C.; Tong, L.; Churchill, L.; Cirillo, P. F.; Gilmore, T.; Graham, A. G.; Grob, P. M.; Hickey, E. R.; Moss, N.; Pav, S.; Regan, J., Inhibition of p38 MAP kinase by utilizing a novel allosteric binding site. *Nat Struct Biol* **2002,** *9* (4), 268-272.

202. Tong, L.; Pav, S.; White, D. M.; Rogers, S.; Crane, K. M.; Cywin, C. L.; Brown, M. L.; Pargellis, C. A., A highly specific inhibitor of human p38 MAP kinase binds in the ATP pocket. *Nat Struct Biol* **1997,** *4* (4), 311-316.

203. Koeberle, S. C.; Romir, J.; Fischer, S.; Koeberle, A.; Schattel, V.; Albrecht, W.; Grütter, C.; Werz, O.; Rauh, D.; Stehle, T., Skepinone-L is a selective p38 mitogen-activated protein kinase inhibitor. *Nat Chem Biol* **2012,** *8* (2), 141-143.

204. Simard, J. R.; Getlik, M.; Grütter, C.; Pawar, V.; Wulfert, S.; Rabiller, M.; Rauh, D., Development of a fluorescent-tagged kinase assay system for the detection and characterization of allosteric kinase inhibitors. *J Am Chem Soc* **2009,** *131* (37), 13286-13296.

205. Strumberg, D.; Schultheis, B., Regorafenib for cancer. *Expert Opin Inv Drug* **2012,** *21* (6), 879-889.

206. Kroe, R. R.; Regan, J.; Proto, A.; Peet, G. W.; Roy, T.; Landro, L. D.; Fuschetto, N. G.; Pargellis, C. A.; Ingraham, R. H., Thermal denaturation: A method to rank slow binding, high-affinity p38 alpha MAP kinase inhibitors. *Journal of Medicinal Chemistry* **2003,** *46* (22), 4669-4675.

207. Baur, B.; Storch, K.; Martz, K. E.; Goettert, M. I.; Richters, A.; Rauh, D.; Laufer, S. A., Metabolically stable dibenzo[b,e]oxepin-11(6H)-ones as highly selective p38 MAP kinase inhibitors: optimizing anti-cytokine activity in human whole blood. *J Med Chem* **2013,** *56* (21), 8561-78.

208. Zimmermann, G.; Zhou, D.; Taussig, R., Mutations Uncover a Role for Two Magnesium Ions in the Catalytic Mechanism of Adenylyl Cyclase. *Journal of Biological Chemistry* **1998,** *273* (31), 19650-19655.

209. Adams, J. A., Activation Loop Phosphorylation and Catalysis in Protein Kinases: Is There Functional Evidence for the Autoinhibitor Model? *Biochemistry-Us* **2003,** *42* (3), 601-607.

210. Cherry, M.; Williams, D. H., Recent kinase and kinase inhibitor X-ray structures: mechanisms of inhibition and selectivity insights. *Curr Med Chem* **2004,** *11* (6), 663-73.

211. Gilburt, J.; Girvan, P.; Blagg, J.; Ying, L.; Dodson, C. A., Ligand discrimination between active and inactive activation loop conformations of Aurora-A kinase is unmodified by phosphorylation. *Chem Sci* **2019**.

212. Markwick, P. R.; Malliavin, T.; Nilges, M., Structural biology by NMR: structure, dynamics, and interactions. *Plos Comput Biol* **2008,** *4* (9), e1000168.

213. Jeschke, G., DEER distance measurements on proteins. *Annu Rev Phys Chem* **2012,** *63*, 419-46.

214. Jeschke, G.; Polyhach, Y., Distance measurements on spin-labelled biomacromolecules by pulsed electron paramagnetic resonance. *Phys Chem Chem Phys* **2007,** *9* (16), 1895-910.

215. Bagshaw, C. R., ATP analogues at a glance. *Journal of Cell Science* **2001,** *114* (3), 459-460.

216. Yin, D. M.; Hammler, D.; Peter, M. F.; Marx, A.; Schmitz, A.; Hagelueken, G., Inhibitor-Directed Spin Labelling—A High Precision and Minimally Invasive Technique to Study the Conformation of Proteins in Solution. *Chemistry – A European Journal* **2018,** *24* (26), 6665-6671.

217. Breitwieser, W.; Lyons, S.; Flenniken, A. M.; Ashton, G.; Bruder, G.; Willington, M.; Lacaud, G.; Kouskoff, V.; Jones, N., Feedback regulation of p38 activity via ATF2 is essential for survival of embryonic liver cells. *Genes & Development* **2007,** *21* (16), 2069-2082.

218. Pulverer, B. J.; Kyriakis, J. M.; Avruch, J.; Nikolakaki, E.; Woodgett, J. R., Phosphorylation of c-jun mediated by MAP kinases. *Nature* **1991,** *353* (6345), 670-674.

219. Kang, Y. J.; Seit-Nebi, A.; Davis, R. J.; Han, J., Multiple activation mechanisms of p38alpha mitogen-activated protein kinase. *J Biol Chem* **2006,** *281* (36), 26225-34.

220. Sicard, P.; Clark, J. E.; Jacquet, S.; Mohammadi, S.; Arthur, J. S. C.; O'Keefe, S. J.; Marber, M. S., The activation of p38 alpha, and not p38 beta, mitogen-activated protein kinase is required for ischemic preconditioning. *J Mol Cell Cardiol* **2010,** *48* (6), 1324-1328.

221. Salvador, J. M.; Fornace, J. A. J.; Ashwell, J. D., Activating p38 MAPK: New Tricks for an Old Kinase AU - Mittelstadt, Paul R. *Cell Cycle* **2005,** *4* (9), 1189-1192.

222. Jeschke, G.; Chechik, V.; Ionita, P.; Godt, A.; Zimmermann, H.; Banham, J.; Timmel, C.; Hilger, D.; Jung, H., DeerAnalysis2006—a comprehensive software package for analyzing pulsed ELDOR data. *Appl Magn Reson* **2006,** *30* (3-4), 473-498.

223. Koshland, D. E., Application of a Theory of Enzyme Specificity to Protein Synthesis. *Proceedings of the National Academy of Sciences* **1958,** *44* (2), 98-104.

224. Vogt, A. D.; Di Cera, E., Conformational Selection Is a Dominant Mechanism of Ligand Binding. *Biochemistry-Us* **2013,** *52* (34), 5723-5729.

225. Bleicken, S.; Jeschke, G.; Stegmueller, C.; Salvador-Gallego, R.; Garcia-Saez, A. J.; Bordignon, E., Structural model of active Bax at the membrane. *Molecular cell* **2014,** *56* (4), 496-505.

226. Pribitzer, S.; Sajid, M.; Hülsmann, M.; Godt, A.; Jeschke, G., Pulsed triple electron resonance (TRIER) for dipolar correlation spectroscopy. *J Magn Reson* **2017,** *282*, 119-128.

227. McPherson, A.; Koszelak, S.; Axelrod, H.; Day, J.; Williams, R.; Robinson, L.; McGrath, M.; Cascio, D., An experiment regarding crystallization of soluble proteins in the presence of beta-octyl glucoside. *J Biol Chem* **1986,** *261* (4), 1969-75.

228. Chen, P. S.; Toribara, T. Y.; Warner, H., Microdetermination of Phosphorus. *Anal Chem* **1956,** *28* (11), 1756-1758.

229. Pronk, S.; Páll, S.; Schulz, R.; Larsson, P.; Bjelkmar, P.; Apostolov, R.; Shirts, M. R.; Smith, J. C.; Kasson, P. M.; van der Spoel, D., GROMACS 4.5: a high-throughput and highly parallel open source molecular simulation toolkit. *Bioinformatics* **2013**, btt055.

230. Abraham, M. J.; Murtola, T.; Schulz, R.; Páll, S.; Smith, J. C.; Hess, B.; Lindahl, E., GROMACS: High performance molecular simulations through multi-level parallelism from laptops to supercomputers. *SoftwareX* **2015,** *1-2*, 19-25.

231. Schmid, N.; Eichenberger, A. P.; Choutko, A.; Riniker, S.; Winger, M.; Mark, A. E.; van Gunsteren, W. F., Definition and testing of the GROMOS force-field versions 54A7 and 54B7. *European biophysics journal* **2011,** *40* (7), 843-856.

232. Huang, J.; Rauscher, S.; Nawrocki, G.; Ran, T.; Feig, M.; de Groot, B. L.; Grubmuller, H.; MacKerell, A. D., Jr., CHARMM36m: an improved force field for folded and intrinsically disordered proteins. *Nat Methods* **2017,** *14* (1), 71-73.

233. Bjelkmar, P.; Larsson, P.; Cuendet, M. A.; Hess, B.; Lindahl, E., Implementation of the CHARMM Force Field in GROMACS: Analysis of Protein Stability Effects from Correction Maps, Virtual Interaction Sites, and Water Models. *J Chem Theory Comput* **2010,** *6* (2), 459-66.

234. Hess, B.; Bekker, H.; Berendsen, H. J.; Fraaije, J. G., LINCS: a linear constraint solver for molecular simulations. *J Comput Chem* **1997,** *18* (12), 1463-1472.

235. Essmann, U.; Perera, L.; Berkowitz, M. L.; Darden, T.; Lee, H.; Pedersen, L. G., A smooth particle mesh Ewald method. *The Journal of chemical physics* **1995,** *103* (19), 8577-8593.

236. Bussi, G.; Donadio, D.; Parrinello, M., Canonical sampling through velocity rescaling. *The Journal of chemical physics* **2007,** *126* (1), 014101.

237. Parrinello, M.; Rahman, A., Polymorphic transitions in single crystals: A new molecular dynamics method. *Journal of Applied Physics* **1981,** *52* (12), 7182-7190.

238. Berendsen, H.; Grigera, J.; Straatsma, T., The missing term in effective pair potentials. *Journal of Physical Chemistry* **1987,** *91* (24), 6269-6271.

239. Daura, X.; Gademann, K.; Jaun, B.; Seebach, D.; van Gunsteren, W. F.; Mark, A. E., Peptide folding: when simulation meets experiment. *Angewandte Chemie International Edition* **1999,** *38* (1-2), 236-240.

240. Steigmiller, S.; Borsch, M.; Graber, P.; Huber, M., Distances between the b-subunits in the tether domain of F0F1-ATP synthase from E. coli. *Bba-Bioenergetics* **2005,** *1708* (2), 143-153.

241. Cheng, N. S., Formula for the viscosity of a glycerol-water mixture. *Ind Eng Chem Res* **2008,** *47* (9), 3285-3288.

242. Pannier, M.; Veit, S.; Godt, A.; Jeschke, G.; Spiess, H. W., Dead-time free measurement of dipole–dipole interactions between electron spins. *J Magn Reson* **2011,** *213* (2), 316-325.

11. List of abbreviations

ASYN	alpha-synuclein
IDP	Intrinsically disordered protein
ATP	adenosine triphosphate
ADP	and adenosine diphosphate
AMP	adenosine monophosphate
EPR	electron paramagnetic resonance
NMR	nuclear magnetic resonance
CD	circular dichroism
MD	molecular dynamics
(sm)FRET	(single molecule) Förster resonance energy transfer
IR	infrared
SDSL	site-directed spin labeling
MTSSL	methanethiosulfonate spin label
Proxyl	3-maleimido proxyl
TOAC	2,2,6,6-tetramethyl-N-oxyl-4-amino-4-carboxylic acid
TOPP	4-(3,3,5,5-tetramethyl-2,6-dioxo-4-oxylpiperazin-1-yl)-L-phenylglycine
cwEPR	continuous-wave EPR
DQC	double-quantum coherence
SIFTER	single frequency technique for refocusing dipolar couplings
DEER	double-electron electron resonance
PELDOR	pulsed electron-electron double resonance
NAC	non-amyloid component
PTM	post-translational modifications
SPPS	solid-phase peptide synthesis
MRW	mean residue ellipticity
LUVs	large unilamellar vesicles
TRIS	tris(hydroxymethyl)aminomethane
MAPK	mitogen-activated protein kinase
DMSO	dimethyl sulfoxide